UNIVERSITÀ DEGLI STUDI DI TRIESTE

Sede Amministrativa del Dottorato di Ricerca

CHINESE ACADEMY OF SCIENCE, INSTITUTE OF GEOLOGY AND GEOPHYSICS

CHINESE EARTHQUAKE ADMINISTRATION, INSTITUTE OF GEOPHYSICS

Posto di dottorato attivato grazie al contributo del
Ministero dell'Istruzione, dell'Università e della Ricerca (MIUR) nell'ambito del progetto:
Advanced methodologies in the field of geophysics and geodynamics
Internationalization Program (D.M. 5 august 2004, n. 262, Art.23)
International University Cooperations, Program 2004-2006, Prot. II04A1CHC8

XXI CICLO DEL
DOTTORATO DI RICERCA IN
GEOFISICA DELLA LITOSFERA E GEODINAMICA

Rayleigh wave tomography in North-China from ambient seismic noise

Settore scientifico-disciplinare GEO/10

DOTTORANDO
LIHUA FANG

RESPONSABILE DOTTORATO DI RICERCA (Coordinatore)
PROF. *PETER SUHADOLC*
FIRMA: _____

RELATORE
PROF. *ZHIFENG DING (CEA)*
FIRMA: _____

SUPERVISORE
PROF. *GIULIANO PANZA*
FIRMA: _____

CORRELATORE
PROF. *JIANPING WU*
FIRMA: _____

CORRELATORE
DR. *FABIO ROMANELLI*
FIRMA: _____

CORRELATORE
DR. *FRANCO VACCARI*
FIRMA: _____

ANNO ACCADEMICO 2008/2009

Acknowledgements

Having spent almost one year in University of Trieste, I am indebted to many great people who gave me much support and help in my academic study, research, and life.

It is my greatest fortune and pleasure that Prof. Giuliano Francesco Panza was my thesis supervisor. Without his insightful supervision and continuous support, I would not have been able to complete this thesis. Giuliano gave me inspiration and encouragement during the entire period of my doctoral study and research. His broad knowledge and research interests really open my minds in the research.

I would also like to thank my Chinese co-supervisor, Prof. Zhifeng Ding and Prof. Jianping Wu of IGPCEA for initiating the international cooperation project. Their guidance broadened my knowledge and research interests. They also gave much help in data collection and analysis. Besides, they also gave many constructive criticisms with the thesis write-up.

I also owe much to Dr Romanelli Fabio, Dr Vaccari Franco, Dr Mariangela Guidarelli and Ms. G. De Meo. They really gave me much help during my stay in Trieste. Special thanks go to Dr Romanelli Fabio, because he helped us to handle many many kinds of documents, such as residence permit, insurance and so on.

My appreciation also goes to Prof. T. B. Yanovskaya for sharing her tomographic software and many instructions on surface wave tomography. I appreciate Prof. Qingju Wu and Prof. Zhengqin He for their great help and valuable suggestions during my research. Dr. Xuemei Zhang and Dr. Sufang Zhang were always helpful and I benefited from the discussion with them. I also owe much to Dr. Huajian Yao of MIT, for many helpful discussions related to ambient noise studies. I would like to thank the colleagues of IGPCEA for their help during deploying the NCSA seismic stations, collecting and processing the data. Many faculty members and researchers in IGPCEA also gave me a lot of help in the past years; I would especially thank Dr. Weilai Wang, Dr. Laiyu Lu and Dr. Zhixiang Yao.

My endless love goes to my family. They are the biggest supports for me anytime and anywhere. I share every happiness and difficulty with them. Without their love and continuing supports, it would have been impossible for me to finish this thesis work.

This work is supported by the Key Program of the National Natural Science Foundation of China (Grant No. 90914005), National Natural Science Foundation of China (Grants No. 40774038), Basic Research Project of Ministry of Science & Technology China (Grants No. 2006FY110100) and National Nonprofit Institute Research Grant of Institute of Geophysics, China Earthquake Administration (Grant No. DQJB09B08). This work is also supported by Italian MUR and University of Trieste in the framework of the Internationalization PhD Program (2004-2006): Advanced methodologies in the field of geophysics and geodynamics (Prot. II04A1CHC8) Coordinated by Giuliano F. Panza.

Abstract

The theory and methodology of ambient noise tomography has been studied and applied to North-China successfully. Continuous vertical-component seismograms, spanning the period from January 1, 2007 to February 28, 2008 recorded by 190 broadband stations and 10 very broadband stations, have been used. The cross correlation technique has been applied to ambient noise data recorded by North-China Seismic Array for each station pairs of the array. Rayleigh wave group velocity dispersion curves are measured at periods between 4 s and 40 s by multiple filter technique. We obtain 5630 high quality dispersion curves. Surface wave tomography is conducted to generate group velocity maps with a grid spacing of 0.25º×0.25º. These maps display higher resolution and extend to shorter periods than previous surface wave tomography maps. Then genetic algorithm is used to invert pure path dispersion curves. The 3-D shear wave velocity structure from 0 to 50 km depth is readily constructed. To the authors' knowledge, the resolution presented here is, so far, the highest one in China mainland.

The original results of this thesis are:

1, The SNR of Green Function is proportional to the square root of observation time and can be enhanced by using the symmetric component. The inhomogeneous distribution of seismic noise gives rise to the asymmetry of Green Function. Using more than one year's data, one can get more symmetric and higher SNR Green Function.

2, The characteristics of ambient seismic noise are different for different period bands. In 4-10 s, a coherent phase with large amplitude near zero lag time is observed. In 10-20 s, the sources of ambient seismic noise have a very clear seasonal variability. The azimuthal distributions of noise share a great similarity with the map of average ocean wave height map obtained by TOPEX-Poseidon. In 20-50s range, Rayleigh wave Green Functions are almost symmetrical and show less seasonal variation in both signal strength and directivity, which indicates that the distribution of noise is

almost homogeneous. In 4-20s range, the amplitudes of positive and negative components of Green Functions are obviously asymmetrical, but the arrival times are almost identical, indicating that the distribution of noise has much influence on the amplitude of Green Function, but less influence on arrival time.

3, Tomographic maps at short periods reveal an evident lateral heterogeneity in the curst of North-China, quite well in agreement with known geological and tectonic features. The North China Basin is imaged as a broad low velocity area, while the Taihangshan and Yanshan uplifts and Ordos block are imaged as high velocity zones, and the Quaternary intermountain basins show up as small low-velocity anomalies.

4, The 3-D S-wave crustal velocity model in North China shows a distinct low velocity belt with NW trend at 10 km of depth near Zhangjiakou-Bohai seismic zone. This low velocity belt and the southern margin of Yanshan high velocity anomaly draw the outline of Zhangjiakou-Bohai seismic zone and its northern border line. There is a well-defined low velocity zone in middle-to-lower crust (15-25 km) in the Beijing-Tianjin-Tangshan region, which may be caused by intrusion of hot mantle materials.

5, We analyzed the seismogenic structure near Tangshan，Luanxian and Ninghe earthquake region. We infer that these three earthquakes are mainly caused by vertical deformation of upper mantle and material exchange between crust and upper mantle. The magma intrudes the crust along faults near the boundary of crust and upper mantle, which leads to the low velocity anomaly in the uppermost mantle. The magma intrusion heats up the lower crustal material and drops its viscosity. Some minerals are dehydrated. The water moves up and is trapped in the middle crust. The existence of liquid affects the structure and composition of the fault zone, further changes the stress state, weakens the seismotectonic region and triggers the earthquakes.

Key Words: Ambient Noise Tomography, Cross Correlation, Rayleigh Wave, Group Velocity, Genetic Algorithm, North China

Contents

Chapter 1 Introduction

1.1 Tectonic background

Cratons, in which the crust was mainly generated in the Precambrian, are typically underlain by mantle lithosphere that is thick, cold, and refractory (e.g., Jordan, 1975). Because it is cold and nearly anhydrous, such lithospheric mantle has a high viscosity and thus contributes significantly to craton stability (e.g., Pollack, 1986; Hirth et al., 2000). Thus the ancient cratons have not undergone major tectonism or magmatism, and no significant crustal growth followed cratonization. However, several lines of evidence suggest that the lithosphere of North China Craton (NCC) is not stable forever, but can be lost or severely modified (decratonized), resulting in significant crustal growth during major tectonomagmatic events (Yang et al., 2008).

The NCC is an important natural laboratory for studying the temporal change of the lithosphere because there is the juxtaposition of Ordovician diamondiferous kimberlites, Mesozoic lamprophyre-basalt and Cenozoic tholeiite-alkali basalts in this craton.

While diamond inclusions, xenoliths and mineral concentrates in kimberlites indicate a thick (>180 km), cold and refractory lithospheric keel beneath the NCC prior to the Palaeozoic, basalt-borne xenoliths reveal the presence of thin, hot and fertile lithosphere in the Cenozoic (Xu, 2001). Petrological and geochemical probing using xenolith from the upper mantle carried up by volcanic extrusions indicates that the lithosphere is no more than 80 km over much of eastern NCC, and is in places less than 60 km thick (e.g., Fan et al., 1993; Menzies et al., 1993; Griffin et al., 1998; Xu, 2001). Geophysical analyses also point to a much thinner lithosphere in eastern NCC (e.g., Liu, 1987; Tian et al., 2009; Chen et al., 2008). This indicates the dramatic change in lithospheric architecture during the Phanerozoic and raises important questions about what processes were involved. Was older crust simply reactivated or does this magmatism represent a growth of new continental crust? What were the mechanisms that allowed the generation of such large volumes of magma within a previously stable craton?

1.2 History of geological evolution

The NCC is one of the oldest ancient continental cores in the world with a basement crystalline complex formed 3.7 Ga. Metamorphism of the platform basement-complex mainly took place in Precambrian (Chen, 1994). The research on Precambrian granitoids indicated (Deng et al., 1999) that the continental crust-forming stages in North China can be approximately marked off into the following stages: (1) TT-type continental crust in Paleo-Archean (called the juvenile stage of continental crust), (2) TTGG-type continental crust in middle-Archean or Neo-Archean (called pre-mature continental crust stage) and (3) GG-type continental crust in Neo-Archean or Paleo-proterozoic (called mature continental crust stage). This result is consistent with the statistic peak of Sm-Nd model ages concentrated in the range of 2.7 Ga and 2.9 Ga as determined by 198 Precambrian metamorphic rocks (Zhang, 1998), and is well correlated with the itabirite deposit mostly developed in Neo-Archean (Sheng, 1998), which is a typical mineral resource of banded iron formation prevailed at that period. Isotopic ages determined in the Sangan area indicate that granulite facies metamorphism of khondalite series, gneiss terrane and high-pressure basic granulite all happened by the end of Paleoproterozoic (Guo et al., 2001). SHRIMP ages of detrital zircon from the Changzhougou formation at the bottom of Mesoproterozoic Changchengian System indicated that the clastic sediments all were come from the crustal source area of North China craton about 2.5 Ga (Wan et al., 2003). Evidence mentioned above indicated that the North China continental crust was formed in early Archean-Paleoproterozoic and has the similar history with the global craton forming process.

The sedimentary cover was mainly formed after Mesoproterozoic and comprise five stages (Qiu et al., 2005): (1) from Mesoproterozoic (Pt_2) to the early stage of middle Ordovician (O_2^1) was a continuous sediment of marine facies; (2) from the late stage of middle Ordovician (O_2^2) to the early stage of Carboniferous Period (C_2^1) was the period of uplift, denudation, weathering and planation of the North China platform entirely lacking of sedimentary records; (3) the sediments of the North China platform change from paralic sedimentary facies gradually to basin sediments of continental facies from the late stage of Carboniferous Period (C_2^2) to Triassic Period (T); (4) Yanshanian Orogenic Period was from Jurassic to Cretaceous; (5) rift basin in eastern

North China was formed from Paleogene to Quaternary Period (E-Q).

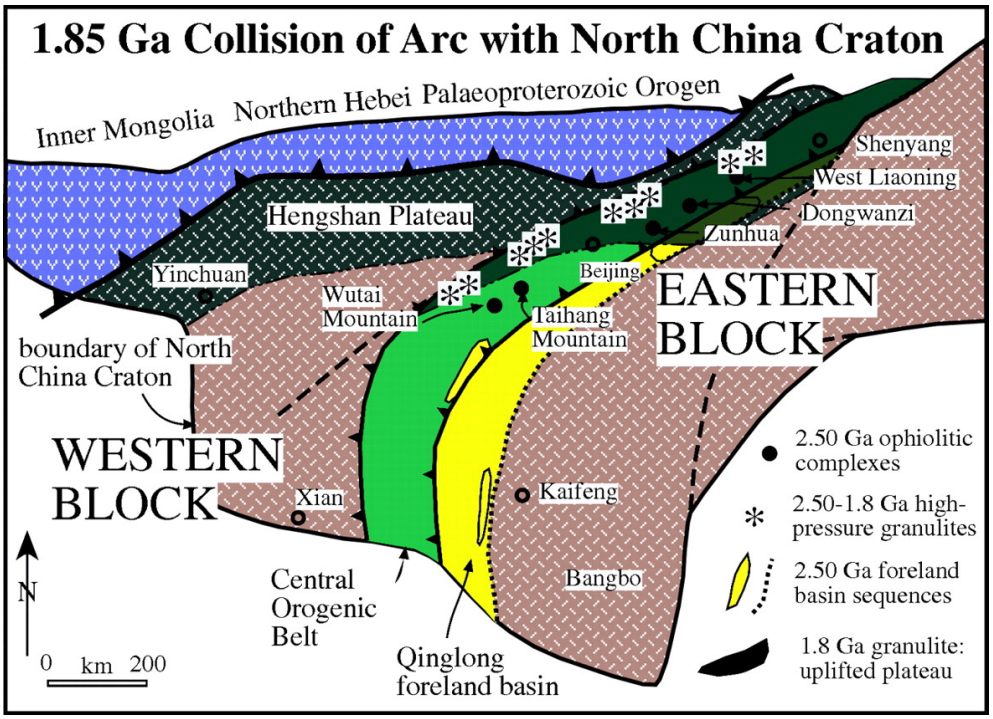

Figure 1-1. Tectonic map of the North China Craton (modified after Kusky et al. 2007).

The NCC is divided into three major blocks, the Eastern and Western blocks, Central Orogenic Belt (Kusky et al., 2007, Figure 1-1). The Eastern and Western Blocks are separated by the Late Archaean Central Orogenic Belt, in which virtually all U–Pb zircon ages (upper intercepts) fall between 2.55 and 2.50 Ga (Zhang 1989; Zhai et al. 1995; Kröner et al. 2002; Zhao et al. 1998, 2005; Kusky et al. 2001, 2004; Kusky & Li, 2003; Polat et al., 2006). The stable Western Block, also known as the Ordos Block (Bai & Dai 1998; Li et al. 1998), is a stable craton with a thick mantle root, no earthquakes, low heat flow, and a lack of internal deformation since the Precambrian. It has a thick platform sedimentary cover intruded by a narrow belt of 2.55–2.50 Ga arc plutons along its eastern margin (Zhang et al. 1998). Much of the Archaean geology of the Western Block is poorly exposed because of thick Proterozoic and Palaeozoic to Cretaceous platformal cover. A platformal cover on an Archaean basement is typical of many Archaean cratons worldwide. In contrast, the Eastern Block is atypical for a craton in that it has been tectonically active and has numerous earthquakes, high heat flow, and a thin lithosphere reflecting the lack of a thick mantle root. The Eastern Block contains a variety of c. 3.80–2.50 Ga gneissic rocks and greenstone belts locally overlain by 2.60–2.50 Ga sandstone and carbonate units (e.g. Bai & Dai 1996, 1998).

Deformation is complex, polyphase, and indicates the complex collisional, rifting, and underplating history of this block from the Early Archaean to the Meso-Proterozoic (Zhai et al. 1992, 2002; Li et al. 2000a; Kusky et al., 2001; Kusky & Li 2003; Zhai, 2005; Polat et al., 2006), and again in the Mesozoic–Cenozoic.

The Central Orogenic Belt (COB) includes belts of TTG, granite, and supracrustal sequences that were variably metamorphosed from greenschist to granulite facies. It can be traced for about 1600 km from west Liaoning in the north to west Henan Province in the south. Greenschist- to amphibolite grade metamorphism predominates in the southeastern part of the COB (such as in the Qinglong belt), but the northwestern part is dominated by amphibolite- to granulite-facies rocks, including some high-pressure assemblages (10–13 kbar at 850±50℃; Li et al., 2000b; Zhao et al., 2001a, b). The high-pressure assemblages occur in the linear Hengshan belt, which extends for more than 700 km with a ENE–WSW trend. Internal (western) parts of the orogen are characterized by thrust-related subhorizontal foliations, shallow-dipping shear zones, recumbent folds, and tectonically interleaved highpressure granulite migmatite and metasedimentary rocks. The COB is in many places overlain by sedimentary rocks deposited in graben and continental shelf environments, and is intruded by c. 2.5–2.4 and 1.9–1.8 Ga dyke swarms. Several large 2.2–2.0 Ga anorogenic granites have also been identified within the belt (Li & Kusky, 2007).

The NCC also suffered two episodes of orogenic modifications during the Mesozoic. Main surface features, including major east–west and north–south fold belts, widespread plutonism, and extensional faults, are related to these events. The first orogenic episode occurred during the Triassic to mid-Jurassic (Indosinian), corresponding to the collision of the NCC with the South China Block. The consumption of over 200,000 km^2 of continental crust had led to ultra-high-pressure (UHP) metamorphism. The collisional event also, for the first time since the formation of the NCC, caused major tectonism and relative elevations in the interior of the NCC. The second orogenic event was the so-called Yanshanian Orogeny developed along northern NCC. It was probably related to the closure of the Mongol-Okhotsk Ocean to the north. Although thin-skinned thrusting was widespread along northern NCC (e.g., Davis et al. 1998), the shallow nature of such structures may not have significant bearings on modern tectonics and seismicity.

1.3 Magmatic activities

Though there were some magmatic events in North China before Jurassic, in Caledonian only diamond-bearing kimberlites intruded in Mengying of Shandong Province and Fuxian of Liaoning Province indicating a small-scale mantle-heat disturbance under cratonic environment (Deng et al., 1996); Hercynian was the collision period between the North China platform and Mongolia micro-continent forming North China continent, and Indosinian was the collision period between the North China continent and South China continent to form China continent. The distribution of magmatic activities for these two periods were mainly limited to the North, Northeast and South margins of the North China platform (Cheng, 1994), and there are not any intra-platform magmatic activities, indicating that the magmatic activities of Hercynian and Indosinian had only very small influence over the interior of North China platform. Therefore, the lacking of large-scale mantle-derived magmatic activities since the formation of North China platform in early Archean-Paleoproterozoic till Jurassic suggests that the lithospheric crust-mantle structure of North China platform kept the long-term stability before Jurassic.

Since Jurassic, the North China platform has been activated with intensive and wide magmatic activities (age of 200–110 Ma) during Yanshanian orogenic movement (Wang et al., 1994; Wilde et al., 2003; Wu et al., 2000; Zhou et al., 2003). The source area of Yanshanian granitoids bear the characteristics of crust-mantle mixing, and has very similar Sr-Nd isotopic composition with coetaneous gabbros, diorite, basic-ultrabasic rock and volcanic rocks (Zhou et al., 2003; Hong et al., 2003; Liu et al., 2004). The recently determined Tectono-magmatic events1) indicate that North China has surpassed a whole orogenic cycle of preliminary stage in J_1 and early stage in J_2 of orogeny→peak orogenic stage in J_3→late orogenic stage in K_1^1→post-orogenic stage in K_1^2; among them, thickening continental crust was formed in J_1-J_2, and then the lithosphere was de-rooted at large-acreage after J_3. The most violent period of magmatic activities was in J_3-K_1^1, which was homologous with large-scale metallogeny of 130—110 Ma (Zhou et al., 2003; Mao et al., 2003) and 120±10 Ma peak period (mostly range in 80—160 Ma) of crust-mantle interaction (Wan et al., 2003; Zhou and Sun, 2003).The wide-spread Mesozoic igneous rocks can be delimitated into several igneous rock belts, such as Jiliao-Ludong, Yanliao, Taihangshan and Luhuai trending

NEE, and Yushan (Henan-Shanxi), the west segment of north margin of North China trending NWW (Cheng, 1994).

The characteristics of Himalayan magmatic activity is the eruption of basaltic magma and lack of intrusive rocks; the basaltic eruptions are mainly distributed on the eastern plain of North China. According to the isotopic ages, volcanic activities can be classified into two cycles: the Paleogene cycle and Neogene-Quaternary cycle, the former are mainly of tholeiites, while the latter are alkali basalts. Since the tholeiites are dominant in the Paleogene cycle and the alkali basalt dominant in the Neogene-Quaternary cycle, it is suggested that the depth of the source of basaltic magma tended to be deepened gradually with time, which accords with the characteristics of typical continental volcanic rifting (Deng, 1989).

The spatial distribution of igneous rocks mentioned above indicates that in the North China platform activation or reconstruction have been inhomogeneous since Jurassic. Voluminous intrusion of granitic magma of crust-mantle mixing source in Yanshanian and basaltic eruption in Himalayan indicate the influx of material and heat of convective mantle into the continental crust in North China in these two magmatic cycles, but their dynamic mechanisms are different from each other, the former is compressive orogenic-mechanism, while the latter is extensional rifting-mechanism.

To sum up all evidence of geology and geophysics mentioned above, we make out that there are three types of lithosphere in the North China platform: The Eerduosi terrane in the West, with fault-depression basin surrounding its boundary with the characteristics of cold, stable, and continental-root existing, belongs to cratonic lithospheric type; Yanshan and Taihangshan Mountains in the middle belong to orogenic lithospheric type, which was formed in the compressive orogenic-mechanism in Mesozoic, without basaltic activity in Cenozoic, indicates that the orogenic character was still kept in there; the East plain of North China belongs to rift lithospheric type, and the massive basaltic eruption is the marker of extensional rifting-mechanism.

1.4 Previous seismic studies in NC

The study region is located at the eastern margin of NCC (Figure. 1-2). The central part of the study area is NCB (North China Basin). NCB is a large epicontinental basin where many uplifts and depression basins developed since the Cenozoic. NCB can be

divided in to two major internal uplifts (Chengning, Cangxian) and four major depressions (Jizhong, Huanghua, Jiyang, and Linqing) (Chang, 1991). The northeastern part of the study area is occupied by the relatively stable Yanshan uplift with its major structure and tectonic trend oriented in the E-W direction. The western and northwestern portions is dominated by the Taihangshan uplift region with some small intermountain basins. To the southeast there is the Luxi Uplift, and to the east the Bohai Bay. In the NCB and the Taihangshan uplift region there are many active faults, oriented in the NE–SW direction. In the two regions, most of the structures and mountain ranges have trends oriented in the NE–SW direction.

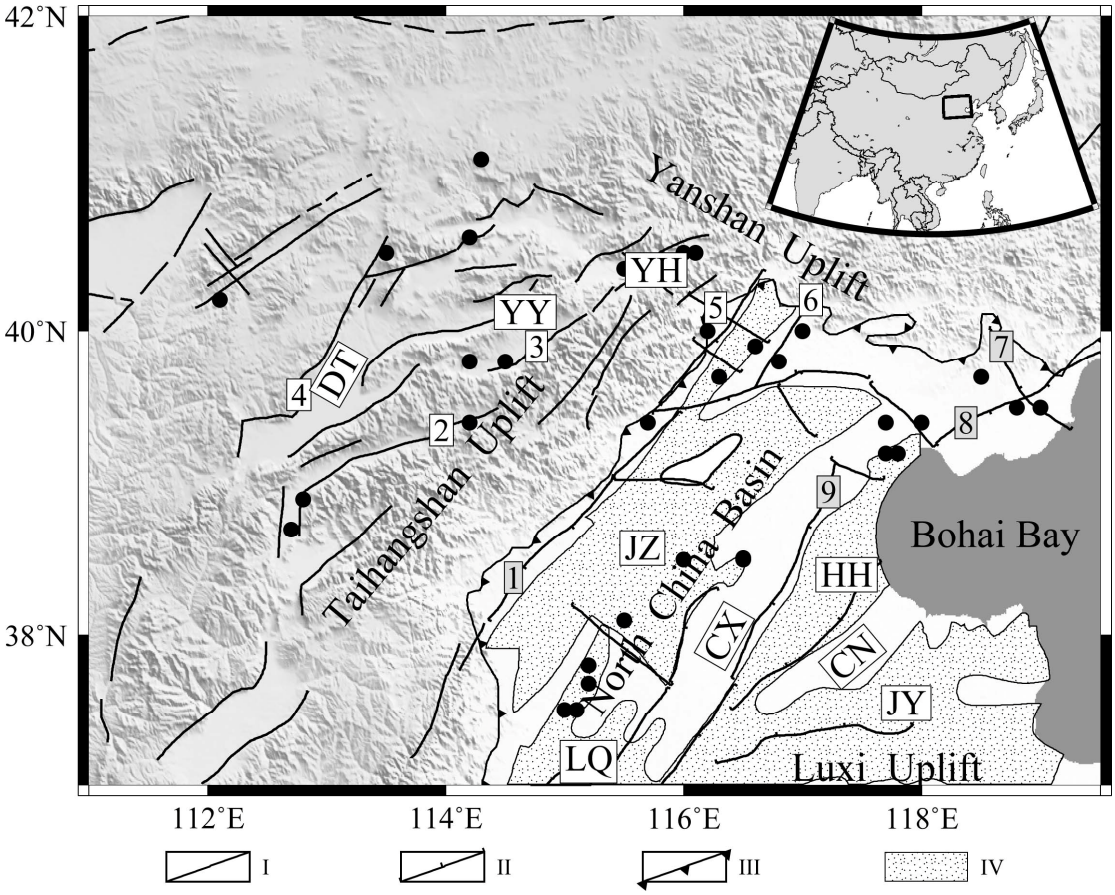

Figure 1-2. Topography and tectonic sketch map of the study region. Modified from Wang et al.(1989) and Deng et al.(2004). The legend is shown at the bottom. I, Major faults; II, Deduced faults; III, Boundary of Cenozoic basins; IV, Depression areas in North China basin. The names of major faults and geological units are as following: 1, Taihangshan fault; 2, Wutaishan fault; 3, Yuxian-Yanqing fault; 4, Kouquan fault; 5, Nankou-Sunhe fault; 6, Xiadian-Fengheying fault; 7, Luanxian-Leting fault; 8, Changli-Ninghe fault; 9, Cangxian fault. The names of the basin and major geological units are: YH, Yanqing-Huailai Basin; YY, Yangyuan-Yuxian Basin; DT, Datong Basin; JZ, Jizhong depression; HH, Huanghua depression; JY, Jiyang depression; LQ, Linqing depression; CX, Cangxian uplift; CN, Chengning uplift. The black dots represent historical earthquakes with magnitude larger than 6.0. The rectangle of the inset map shows the location of

the study region.

This North China is one of the most seismic active areas in China. Historical strong earthquakes occurred frequently in this area. More than 200 earthquakes with magnitude greater than 5.0 have occurred in this region since 780 BC, among them 37 events are larger than M= 6.0 and 10 events are larger than M= 7.0 (The Earthquake Disaster Prevention Department of China Earthquake Administration, 1995, 1999; China Earthquake Networks Center, 2008). In 1679, an earthquake of M= 8.0 occurred in Sanhe; it is the largest one among the known historical earthquakes in this region. The 1976 Tangshan earthquake (M=7.8) killed at least 240,000 people, and was one of the most destructive earthquakes in the world in human history. In the study region, there are several large cities (e.g., Beijing, Tianjin, Tangshan, and Shijiazhuang) in addition to numerous towns and villages. A detailed investigation of the crustal structure and seismotectonics of this region is very important for the understanding of physics of continental earthquakes and for the assessment of seismic hazard and for the mitigation of the seismic risk.

The North China has been intensively investigated by a variety of seismic methods and techniques, such as deep seismic sounding profiling, wide-angle reflection/refraction profiling, body wave and surface wave tomography, receiver function, anisotropy and so on. In the following, we will make a brief summary of the related studies in NC.

Deep seismic sounding: A major effort in the NC region is deep seismic sounding (DSS) using active sources to image the crustal structure (e.g. Zhang et al., 1997; Jia et al., 2005a, b). The coverage of the DSS profiles is particularly dense in North China. These studies revealed strong lateral heterogeneities in the velocity structure of the crust and uppermost mantle as well as significant lateral variations in the crustal thickness beneath this area, also low-velocity zones in the mid-crust were observed in many regions.

Body wave tomography: In recent years seismic tomography has become a powerful tool for studying the crust and mantle structure. Many researchers have investigated the 3D seismic velocity structure of the crust and uppermost mantle beneath North China and adjacent areas using earthquake arrival times (e.g., Sun and Liu, 1995; Liu et al., 1986; Huang and Zhao, 2004; Ding et al., 2009; Tian et al., 2009).

These tomography studies have revealed a complex and dramatically thinned lithosphere beneath eastern China.

Surface wave tomography: Many surface wave tomography studies have also been conducted (e.g., Feng & Teng, 1983; Ritzwoller & Levshin，1998，Huang et al., 2003), but most of them are at China mainland scale and the lateral resolution is of the order of 100-200km. Few studies of surface waves in North-China have been undertaken, which is due to the relatively low level of seismicity and the consequent logistic limitation suffered by earthquake-based surface wave tomography. Recently, He et al. (2009) obtained phase velocity tomography results using the surface wave data recorded by NCSA. The resolution is greatly enhanced due to the dense array and is estimated to be 30-50 km. Previous surface wave tomography studies almost exclusively used teleseismic earthquakes. It is difficult to obtain reliable short-period (<10 s) dispersion measurements from distant earthquakes due to intrinsic attenuation and scattering along the ray paths, but it is the most useful information for constraining the structure of the crust and uppermost mantle. Moreover, the long paths also result in broad lateral sensitivity kernels which limit the resolution to hundreds of kilometers. For these reasons, high-resolution surface wave tomography results are scarce.

Receiver function: The receiver function method has been applied to study the shear wave velocity structures. Recent teleseismic P receiver function studies (Zheng et al., 2005, 2006, 2007; Wang et al., 2009) showed marked structural differences of the crust among the NCB, the Taihangshan uplift and the Yanshan uplift. Receiver function *h-k* stack results give the lateral variations of sedimentary cover, crust thickness and Poisson's ratio (Xu & Zheng, 2005; Luo et al., 2008; Wang et al., 2009). P-wave receiver function migration results reveal a 60- to 80-km-thick present-day lithosphere beneath the study region, significantly thinned from the Paleozoic lithosphere of >180 km (Chen et al., 2006). S-wave receiver function migration results indicate that the LAB is as shallow as 60–70 km in the southeast basin and coastal areas and deepens to no more than 140 km in the northwest mountain ranges and continental interior. These observations indicate widespread lithospheric thinning in North China in comparison with the lithospheric thicknesses typical of most cratonic regions (＞180 km).

Other geophysical methods such as anisotropy, magnetotelluric, gravity and aeromagnetic soundings are also used (Liu et al., 1989; Zhao et al., 2008).

To sum up, extensive seismic studies have been conducted in North China and many meaningful results are obtained. However, in the above-mentioned studies, main shortcomings and drawbacks still exist due to the limitations of methodology, low precision of earthquakes location, short number of seismic stations and their non-uniform spatial distribution.

1.5 The NCSA project

North China hosts the most vital industrial, commercial, residential, and political centers of China. It is one of the most geologically active continental regions in the world, with frequent and devastating earthquakes. It is also geologically the best studied regions in China where abundant geological and geophysical data provide a firm foundation for the proposed Earth system studies.

In order to study the formation and evolution of NCC, to obtain crust and upper mantle structure and to verify various proposed mechanisms for the interpretation of the lithospheric processes which occurred in NCC, a seismic experiment (NCSA) has been carried out between November 2006 and November 2008. 250 portable stations were deployed in North China. The range of the interstation paths spans from 8 km to over 600 km, while the average station separation is about 35 km. The experiment ran continuously with the sampling rate of 50 Hz. There are three types of sensors, of which 190 are broadband sensors (Guralp CMG-3ESPC sensor, corner frequency: 0.033 Hz), 10 are very broadband sensors (Guralp CMG-3T sensor, corner frequency: 0.0083 Hz) and 50 are short period sensors (Guralp CMG-40T sensor, corner frequency: 1 Hz). The recorder unit is Reftek-130B digitizer with an installed GPS clock correction system. Each of the unit was equipped with two 2 Gb memory card. In order to decrease the anthropic noise, sensors were buried in a pit with 1 m depth. The main power to the units was supplied via a 12 V battery charged with alternating current or solar panel. The station locations were chosen not only according to the geological formations but also to logistical reasons. Each of the stations was built inside an agricultural property which helped to ensure the security of the equipment.

This experiment is designed to identify some of the fundamental questions regarding the geodynamics in the NC. One of the focus areas of this research plan is the active crustal deformation and earthquakes, since NC has the most active intracontinental seismicity in the world. Another focus area covers the

asthenosphere-lithosphere interactions and, in particular, the understanding of the mantle processes responsible for the decraton of the NC lithosphere.

1.6 Thesis structure

Experimental and theoretical studies have shown that the elastodynamic Green function between two points can be estimated from the cross correlation of recordings made at the two locations (Weaver & Lobkis, 2001; Derode et al., 2003a, b; Larose et al., 2005a, b; Snieder, 2004; Wapenaar, 2004). Surface wave empirical Green functions (EGFs) estimated from ambient noise and its dispersion characteristics can be used to produce dispersion tomography maps. The ambient noise tomography (ANT) method alleviates some of the problems affecting traditional surface wave measurements made on teleseismic earthquake recordings. This method has been successfully applied in several geographical settings, such as Southern California (Shapiro et al., 2005; Sabra et al., 2005a), Tibet (Yao et al., 2006), Europe (Yang et al., 2007), New Zealand (Lin et al., 2007), China mainland (Zheng et al., 2008), and elsewhere in the world.

In view of the above background, the general objective of my doctoral thesis is to investigate the crustal velocity structure beneath North-China. Specific objectives include:

(1) Construct a high resolution 3-D shear velocity model in crust beneath North-China;

(2) Probe possible relationship between the velocity structure and major faults (e.g., Taihangshan fault);

(3) Characterize the ambient noise features of NCSA.

This thesis consists of six chapters.

In chapter 1, we review the tectonic background of North-China and previous studies related to this thesis work. We introduce the North-China Seismic Array project and present the objectives of this thesis research.

In chapter 2, we describe the theory of ambient noise tomography and data processing procedure.

In chapter 3, we discuss the tomographic inversion results.

In chapter 4, we describe the theory of inverting dispersion data with Genetic Algorithm and present the 3-D S-wave velocity model in North-China.

In chapter 5, we analyse the noise characteristics in North-China.

In chapter 6, we present the discussions, conclusions and recommendations of this study.

Chapter 2 Data and method

2.1 Data

Continuous vertical-component seismograms, spanning the period from January 1, 2007, to February 28, 2008, recorded by 190 broadband stations and 10 very broadband stations, are used in this study (Figure 2-1). The broadband stations are equipped with Guralp CMG-3ESPC seismometers (60s to 50Hz flat velocity response), while the very broadband stations are equipped with Guralp CMG-3T seismometers (120s to 50Hz flat velocity response).

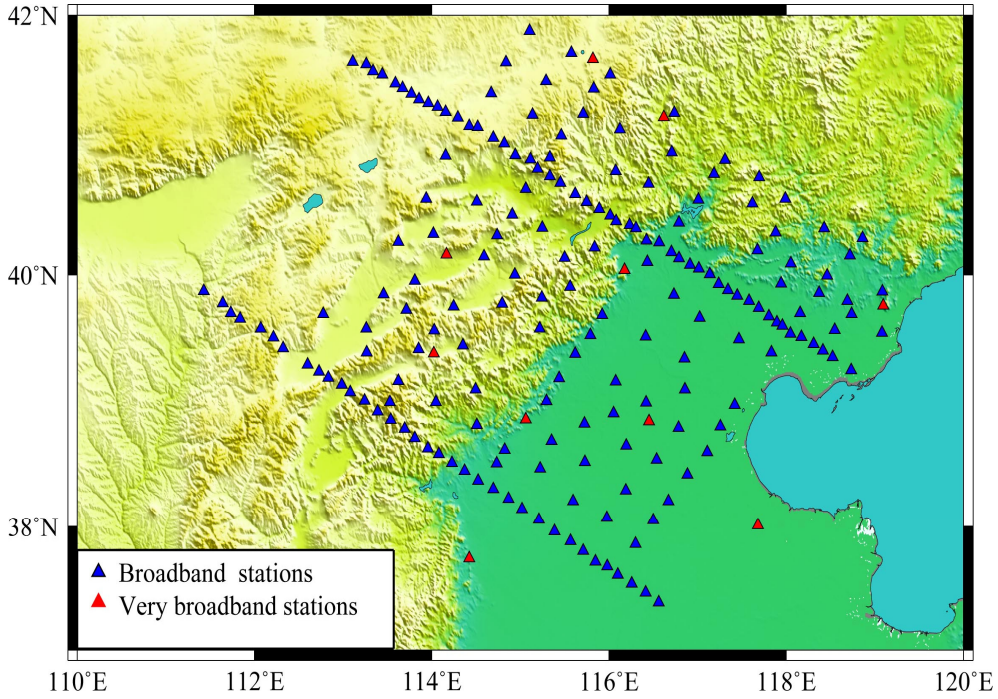

Figure 2-1. Locations of the seismic stations used in this study: blue and red triangles show the locations of broadband and very broadband stations, respectively.

2.2 Ambient noise tomography

2.2.1 Introduction

Surface waves are evanescent and propagate along Earth's surface with group (or phase) velocities that depend on frequency; their dispersion can be used to study the medium properties at different depths. At long periods (e.g., T > 100s) surface waves are mainly sensitive to the shear velocity structure at large depth (e.g., upper mantle),

while at short periods (e.g., T < 30s) they sample the shallower structure. As a corollary, the depth resolution of short period surface waves is much better than that of longer period waves.

Surface waves propagating from earthquakes to one or more receivers have been widely used to study the crust and upper mantle structure, on both regional and global scale. Various approaches have been used for regional surface wave tomography, including the construction – and point-wise inversion – of group (or phase) velocity maps (Ritzwoller & Levshin, 1998; Curtis et al., 1998; Panza et al., 2007; and many others), the measurement of inter-station phase velocities through traditional two-station analysis (e.g., Yao et al., 2005), or (partitioned) waveform inversion (e.g., Nolet, 1990; Simons et al., 1999). Forsyth and Li (2005) developed a two plane-wave method to analyze the 2-D variation of surface wave phase velocities across arrays with small foot-prints (compared to the source-receiver distance). Surface waves can be used to investigate both the isotropic and anisotropic structure in the crust and upper mantle, which can help understand subsurface deformation. In fact, surface wave dispersion provides more direct constraints on depth variation in azimuthal and radial anisotropy (e.g., Montagner & Nataf, 1986; Montagner & Tanimoto, 1991; Simons et al., 2002; Sebai et al., 2006) than shear wave splitting of, for instance, SKS waves.

In North-China and surrounding areas, numerous tomographic studies have been conducted with earthquake data. However, due to the small number of stations, the lateral resolution of these tomographic studies, especially surface wave tomography, is usually quite poor (>100 km). Furthermore, it has been difficult to obtain reliable constraints on the crustal structure from surface wave dispersion, since at short periods (e.g., T < 10 s) the waveforms are usually affected by scattering due to strong crustal heterogeneity. Furthermore, the sparse and uneven distribution of earthquake sources and the uncertainties of the spatial characteristics of surface-wave sensitivity kernel also limit the resolution and the accuracy of traditional approaches for surface wave tomography.

The lateral resolution of tomographic images can be improved by increasing the number of stations in the study area, for example through the deployment of temporary seismograph arrays. The deployment of NCSA offers us an opportunity to obtain high resolution tomography maps.

To improve the radial resolution one must extend the frequency bandwidth, in particular towards shorter periods. Research in ultrasonic and seismology (e.g., Lobkis & Weaver, 2001; Campillo & Paul, 2003; Shapiro & Campillo, 2004) demonstrates that the short period surface wave Green's function (essentially, ground displacement due to a point source) between pairs of receivers can be extracted from the time-domain correlation of ambient noise and coda waves (i.e., scattered waves). Since the measurements can be made between each station pair, this approach leads to high resolution surface wave array tomography at short periods (e.g., Shapiro et al., 2005).

The first attempts to use ambient noise for surface wave tomography, called ambient noise surface wave tomography, were applied to stations in Southern California (Shapiro et al. 2005; Sabra et al. 2005a). Ambient noise tomography is now expanding rapidly. Recent applications have arisen across all of California and the Pacific Northwest (Moschetti et al. 2007), in South Korea (Cho et al. 2006), in Tibet (Yao et al. 2006), in Europe (Yang et al. 2007), across New Zealand (Lin et al. 2007), as well as elsewhere in the world.

2.2.2 Theoretical background

The Green's function of a medium between two points A and B represents the record we would obtain at A if an impulsive source is applied at B.

In the case of a completely random wavefield, the cross correlation of signals recorded between two points converges to the complete Green's function of the medium, including all reflection, scattering and propagation modes (Weaver 2005). To demonstrate this result and to define more precisely under which assumption it is valid, various experimental, numerical and theoretical approaches have been developed.

Historically speaking, helioseismology was the first field where ambient-noise cross correlation performed from recordings of the Sun's surface random motion was used to retrieve time-distance information on the solar surface (Duvall et al. 1993; Gilles et al. 1997). The idea of day-light imaging was proposed by Claerbout (1968) in the context of prospecting. More recently, a seminal paper was published by Weaver and Lobkis (2001), who showed how diffuse thermal noise recorded and cross-correlated at two transducers fastened to one face of an aluminium sample provided the complete Green's function between these two points. They theoretically interpreted this result by invoking equipartitioning of the modes excited in the

aluminium sample. This result was generalized to the case where randomization is not produced by the distribution of sources, but is provided by multiple scattering that takes place in heterogeneous media (Lobkis and Weaver, 2001).

The use of a spectral representation (Lobkis and Weaver, 2001), the fluctuation-dissipation approach (Weaver and Lobkis, 2001, 2003; van Tiggelen, 2003; Godin, 2007) or a correlation-type representation theorem (e.g. Wapenaar, 2004) are rigorous theoretical approaches to interpret experimental results.

Experimental evidences demonstrated the feasibility of passive imaging in 1) acoustics (Lobkis and Weaver, 2001; Weaver and Lobkis, 2001; Larose et al., 2004), 2) seismology where Campillo and Paul (2003) retrieve the Green's function between two seismic stations from a collection of earthquakes, and 3) oceanography in shallow underwater acoustics where both direct and reflected wavefronts were retrieved from ambient-noise cross correlation (Roux and Kuperman, 2004; Sabra et al., 2005b). By summing the contributions of all sources to the correlation, it has been shown numerically that the correlation contains the causal and acausal Green's function of the medium (Wapenaar, 2004). Cases of non-reciprocal (e.g. in the presence of a flow) or inelastic media have also been theoretically investigated (Wapenaar 2006; Godin 2007).

Derode et al. (2003a, b) proposed to interpret the Green's function reconstruction in terms of a time-reversal analogy and showed that correlation of multiply scattered waves could be used for passive imaging in acoustics. The convergence of the noise correlation function towards the Green's function in an unbounded medium can also be interpreted through the stationary phase theorem (Snieder 2004; Roux et al. 2005b).

In seismology, Aki (1957) proposed a long time ago to use seismic noise to retrieve the dispersion properties of surface waves in the subsoil. Shapiro and Campillo (2004) reconstructed the surface wave part of the Green's function by correlating seismic noise at stations separated by distances of hundreds to thousands of kilometers, and measured their dispersion curves at periods ranging from 5 to about 150 seconds. This method led to the first application of passive seismic imaging in California (Shapiro et al. 2005; Sabra et al. 2005a) with a much greater spatial accuracy than for usual active techniques. Larose et al. (2005) also used noise cross correlation at small distances on the moon.

For the problem of elastic waves, it has been theoretically shown that the convergence of noise correlation to the Green's function was bonded by the equipartition condition of the different components of the elastic field (Sanchez-Sesma et al. 2006a, 2007). In other words, the emergence of the Green's function is effective after a sufficient self-averaging process that is provided by random spatial distribution of the noise sources when considering long time series as well as scattering (Campillo 2006; Larose et al. 2006a).

2.2.3 Extraction of Green's function by cross correlation

Gouédard et al. (2008) show that the cross correlation of noise recorded at two distant stations A and B yields the Green's function, assuming that the wavefield is a white noise distributed everywhere in the medium, with no assumption about the medium. Following is the detailed formula derivation.

We consider any medium X, that does not need to be homogeneous, where the wave propagation equation is controlled by a damped equation that can be written as:

$$\frac{\partial^2 u}{\partial t^2} + 2a\frac{\partial u}{\partial t} - Lu = f \qquad (1)$$

Here $a > 0$ is a constant that corresponds to the attenuation of the medium, $f(t,\vec{r})$ is the source field (i.e. the noise field in our case) and $u(t,\vec{r})$ denotes the displacement field. If $L = c^2(\vec{r})\Delta$,we recognize the usual wave equation. In a more general calculation, L can be any negative self-adjoint elliptic differential operator. In more physical terms, L is an operator which preserves energy.

First of all we will introduce a definition of the Green's function in the frequency domain using the integral kernel of the operator L, and show that this definition is equivalent to the usual one. Then, by expressing the displacement field using the Green's function, we will calculate the cross correlation and find how the derivative of the cross correlation function is linked to the Green's function.

We introduce the integral kernel of an operator P, denoted by $[\![P]\!](x,y)$ by:

$$\forall u:\ X \mapsto \mathbb{R}^3,\ (Pu)(x) = \int_X [\![P]\!](x,y)u(y)dy$$

This is the 'continuous matrix' of the operator P. It has to be linked to the case of a

finite space where one can define the matrix (P_{ij}) of P and write the following formula:

$$\forall u:\ X \mapsto \mathbb{R}^3,\ (Pu)_i = \sum_j P_{ij} u_j$$

We first consider a medium without attenuation, i.e. $a = 0$ in equation 1. Let us define the Green's function of L in the frequency domain, denoted by $\hat{G}(\omega + i\varepsilon, \vec{r}, \vec{r}_s)$, with ε a small positive value, as the opposite of the integral kernel of $((\omega + i\varepsilon)^2 + L)^{-1}$. In other words, $\hat{G}$ is the resolvent of L evaluated at point $(\omega + i\varepsilon)^2$. The $\hat{\bullet}$ denotes a function defined in the Fourier space. ε ensures that $((\omega + i\varepsilon)^2 + L)$ is invertible as L has real eigenvalues. We will show that this mathematical definition of $\hat{G}$ is the same as the usual one, which is the causal solution of the wave equation (equation 1) when the source function f is a Dirac impulse in time and space $\delta(t, \vec{r} - \vec{r}_s)$.The Green's function $\hat{G}(\omega + i\varepsilon, \vec{r}, \vec{r}_s)$ admits a limit as $\varepsilon \to 0^+$,denoted by $\hat{G}(\omega + i0, \vec{r}, \vec{r}_s)$, as a Schwartz distribution on the real axis. If L has a continuous spectrum, this limit is a smooth function (the 'limiting absorption principle'). $\hat{G}$ can thus be written as:

$$\begin{aligned}
\hat{G}(\omega + i0, \vec{r}, \vec{r}_s) &= -\left[\!\left[((\omega + i0)^2 + L)^{-1} \right]\!\right](\vec{r}, \vec{r}_s) \\
&= -\int_X \left[\!\left[((\omega + i0)^2 + L)^{-1} \right]\!\right] \\
&\qquad \times (\vec{r}, \vec{r}')\delta(\vec{r}' - \vec{r}_s) d\vec{r}' \\
&= -((\omega + i0)^2 + L)^{-1} \delta(\vec{r} - \vec{r}_s)
\end{aligned}$$

which yields:

$$-((\omega + i0)^2 + L)\hat{G}(\omega + i0, \vec{r}, \vec{r}_s) = \delta(\vec{r} - \vec{r}_s)$$

The inverse Fourier transform of this equation gives a relation that is the usual definition of G in the case of a medium without attenuation:

$$\frac{\partial^2 G}{\partial t^2}(t, \vec{r}, \vec{r}_s) - LG(t, \vec{r}, \vec{r}_s) = \delta(t)\delta(\vec{r} - \vec{r}_s)$$

G is thus the solution of equation 1 in the case of an impulsive source in time and space. One can compute the inverse Fourier transform of $\hat{G}(\omega + i\varepsilon, x, y)$ using residue calculus, and take the limit as ε goes to 0 to obtain

$$G(t,\vec{r},\vec{r}_s) = Y(t)\left[\!\left[\frac{\sin t\sqrt{-L}}{\sqrt{-L}} \right]\!\right](\vec{r},\vec{r}_s)$$

where Y is the Heaviside-step function, and where we denote $\sqrt{-L}$ the operator which eigenvalues are the images of the eigenvalues of L by the function $x \mapsto \sqrt{-x}$ (idem for the sinus function).

If we consider an attenuating medium, the Green's function $\hat{G}(\omega,\vec{r},\vec{r}_s)$ is defined by the resolvent of L evaluated at point $\omega^2 + 2ia\omega$ instead of $(\omega + i0)^2$. It thus becomes

$$G_a(t,\vec{r},\vec{r}_s) = Y(t)e^{-at}\left[\!\left[\frac{\sin t\sqrt{-L-a^2}}{\sqrt{-L-a^2}} \right]\!\right](\vec{r},\vec{r}_s) \qquad (2)$$

We now define the time domain cross correlation between the displacement at two points A and B as:

$$C(\tau,\vec{r}_A,\vec{r}_B) = \lim_{T\to+\infty} \frac{1}{T}\int_0^T u(t,\vec{r}_A)\overline{u(t+\tau,\vec{r}_B)}dt \qquad (3)$$

where the bar denotes the conjugate. $u(t,\vec{r})$ can be expressed using the Green's function G_a (here attenuation is necessary to ensure convergence of the integral, see Roux et al. (2005b)) and the source function f as follows:

$$u(t,\vec{r}) = \int_0^\infty dt' \int_X G_a(t',\vec{r},\vec{r}_s) f(t-t',\vec{r}_s)d\vec{r}_s$$

We assume that f is a white noise distributed everywhere in the medium X, acting at any time t. In the frequency domain, a white noise contains all the frequencies with a random phase. In the time domain, this is a random wavefield such that the position and the activation time of each source are uncorrelated. In this case, and considering a damping medium, we replace the large T limit in the correlation by an ensemble average. We then obtain the following explicit expression for the correlation between the wavefields recorded at A and B (see Gouédard et al. (2008) for mathematical details):

$$C(\tau,\vec{r}_A,\vec{r}_B) = \frac{\sigma^2 e^{-a|\tau|}}{4a}\left[\!\left[(-L)^{-1}(\cos\tau\sqrt{-L-a^2}) + a\frac{\sin|\tau|\sqrt{-L-a^2}}{\sqrt{-L-a^2}} \right]\!\right](\vec{r}_A,\vec{r}_B) \qquad (4)$$

where σ is the variance of the noise wavefield.

The time derivative of this equation is expressed in terms of the Green's function using (2), giving the more familiar expression:

$$\frac{d}{d\tau}C(\tau,\vec{r}_A,\vec{r}_B)=\frac{-\sigma^2}{4a}(G_a(\tau,\vec{r}_A,\vec{r}_B)-G_a(-\tau,\vec{r}_A,\vec{r}_B)) \qquad (5)$$

This means that for any medium, the time-derivative of the cross correlation computed between the wavefields recorded at two stations A and B is the Green's function of the medium, provided that the damping coefficient is small enough and that noise sources behave as white noise acting everywhere in the medium. This is the same hypothesis as stated in Roux et al. (2005b), Lobkis and Weaver (2001) and others, but *L* is now an arbitrary negative definite elliptic operator, and so the present result is more general.

2.3 Data processing

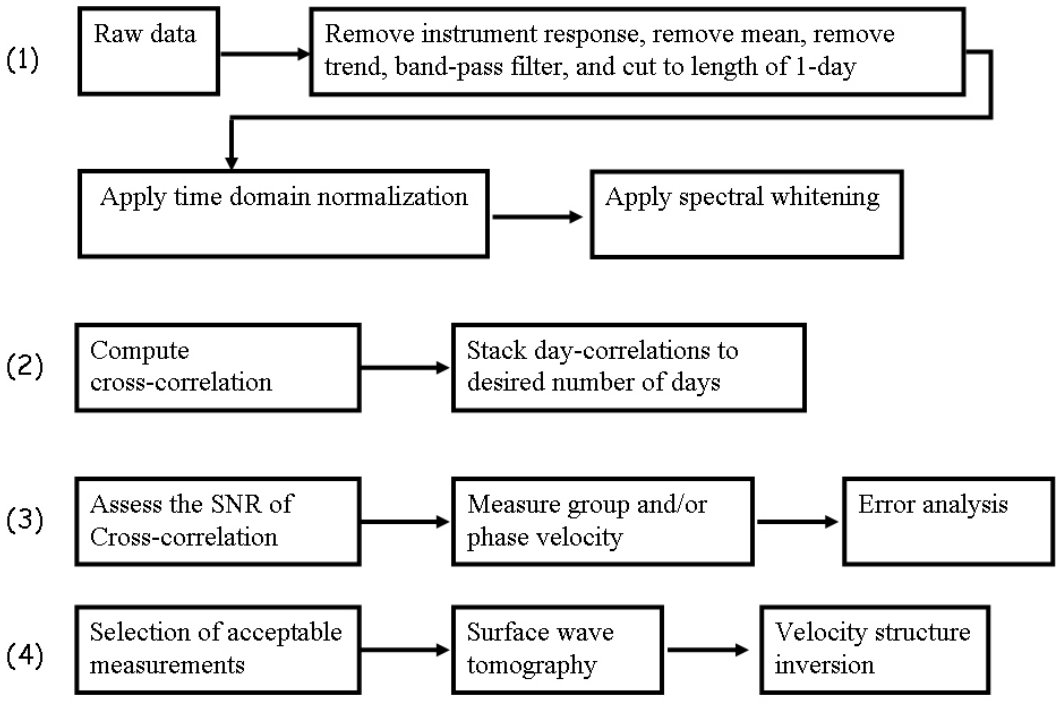

Figure 2-2. Schematic representation of the data processing scheme.

In its current state, the ambient noise data processing procedure divides into four principal phases that are applied roughly in order: (1) single station data preparation, (2) cross correlation and temporal stacking, (3) measurement of dispersion curves and (4)

quality control, including error analysis and selection of the acceptable measurements. These steps are presented schematically in Figure 2-2. After data processing is complete, tomography for group or phase speed maps and inversion for a Vs model may follow. The discussion about tomography and depth inversion will be presented in Chapter 3 and Chapter 4.

2.3.1 Single station data preparation

The first phase of data processing consists of preparing waveform data from each station individually. The purpose of this phase is to accentuate broad-band ambient noise by attempting to remove earthquake signals and instrumental irregularities that tend to obscure ambient noise. In addition, because the spectral amplitude of ambient noise peaks in the microseism band, methods have to be devised to extract the longer period ambient noise from seismic records. Figure 2-2 shows the steps that compose Phase 1 of data processing: resample (decimate to 1 Hz), removal of the instrument response, de-meaning, de-trending and bandpass filtering (4-100 s) the seismogram, time-domain normalization and spectral whitening. This procedure is typically applied to a single day of data. Day data with less than 90 per cent 'on-time' are currently rejected.

The most important step in single-station data preparation is what we call 'time-domain' or 'temporal normalization'. Time-domain normalization is a procedure for reducing the effect on the cross correlations of earthquakes, instrumental irregularities and nonstationary noise sources near to stations.

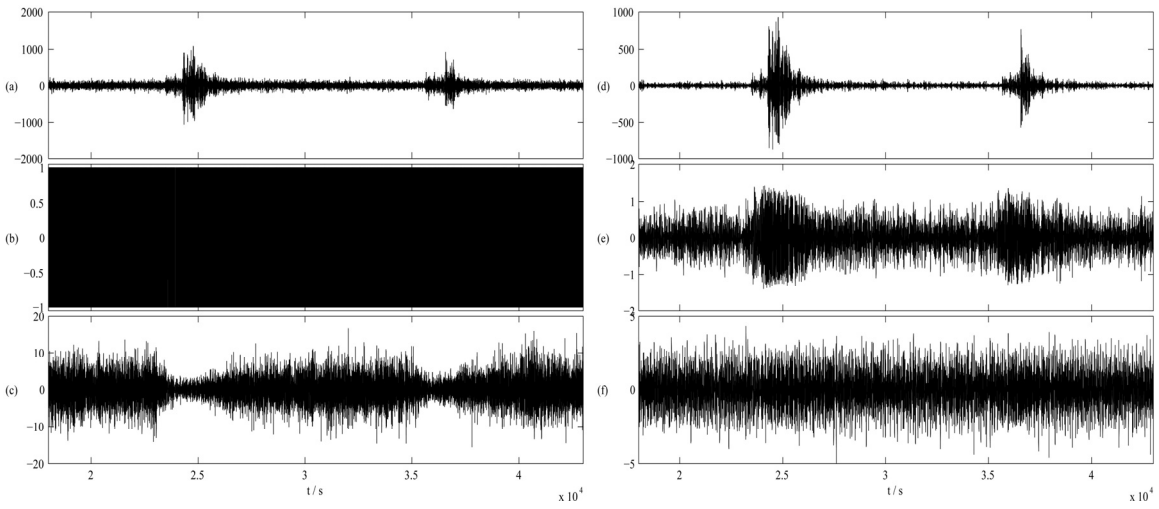

Figure 2-3. A comparison of two time-domain normalization methods applied to earthquake signals for data from LIQ station. (a) Raw broad-band data from Jan. 27, 2007 showing two

earthquakes, recorded by LIQ station. (b) Data after temporal normalization using one-bit method. (c) Data after temporal normalization using running-absolute-mean method. (d), (e) and (f) are bandpass filtered (15 -50 s) waveforms to (a), (b) and (c).

At present, two normalization methods are often used. The first and most aggressive method is called 'one-bit' normalization, which retains only the sign of the raw signal by replacing all positive amplitudes with a 1 and all negative amplitudes with a −1. This method has been shown to increase signal-to-noise ratio (SNR) when employed in acoustic experiments in the laboratory (Larose et al. 2004) and has been used in a number of early seismic studies of coda waves and ambient noise (Campillo & Paul 2003; Shapiro & Campillo 2004; Shapiro et al. 2005; Yao et al. 2006). The second method is running-absolute-mean normalization, employed for example by Bensen et al. (2007). This method computes the running average of the absolute value of the waveform in a normalization time window of fixed length and weights the waveform at the centre of the window by the inverse of this average. The temporal weights of the running-absolute-mean normalization are computed on the waveform filtered in the earthquake band. In this case, if d_j is the raw seismogram and $\hat{d}_j$ is the seismogram bandpass filtered in the earthquake band. We compute the normalization weight for time point n as:

$$\omega_n = \frac{1}{2N+1} \sum_{j=n-N}^{n+N} \left| \hat{dj} \right|,$$

so that the normalized datum becomes $\tilde{d}_n = d_n / \omega_n$. The width of the normalization window (2N+1) determines how much amplitude information is retained. A one-sample window (N =0) is equivalent to one-bit normalization, while a very long window will approach a re-scaled original signal as N→∞. After several tests, we find the signal to noise ratio (SNR) of the cross correlation function is a bit higher when the running average is computed between 15s and 50s using a 50 s normalization window. An example result of the application of this method is shown in Figure 2-3. Figure 2-3f shows that the earthquake signals have been removed by running-absolute-mean, whereas one-bit method can not remove the earthquake signals effectively (Figure 2-3e).

This method is not faultless, however. For example, it does not surgically remove narrow data glitches, as it will inevitably down-weight a broad time interval around the

glitch. One-bit normalization does not suffer from this shortcoming.

The principal reason we prefer running-absolute-mean normalization over the water-level or one-bit normalization methods is its greater flexibility and adaptability to the data. For example, in areas with high regional seismicity it is desirable to tune the time domain normalization to the frequency content of the seismicity.

2.3.2 Spectral normalization or whitening

Ambient noise is not flat in the frequency domain (i.e. it is not spectrally white), but is peaked near the primary (around 15 s period) and secondary (around 7.5 s period) microseisms and rises at very long periods above 50 s to form a signal now referred to as Earth 'hum' (e.g. Rhie & Romanowicz 2004). Inversely weighting the complex spectrum by a smoothed version of the amplitude spectrum produces the normalized or whitened spectrum. Spectral normalization acts to broaden the band of the ambient noise signal in cross correlations and also combats degradation caused by persistent monochromatic sources such as the Gulf of Guinea source. Spectral whitening can eliminate the persistent monochromatic sources sufficiently and can reduce broad imbalances in single-station spectra to aid in the production of a broad-band dispersion measurement.

2.3.3 Cross correlation, stacking and signal emergence

After the preparation of the daily time-series, the next step in the data processing scheme is cross correlation and stacking. We perform cross correlations between all possible station pairs and perform data selection later. This yields a total of $n(n-1)/2$ possible station pairs, where n is the number of stations. Cross correlation is performed daily in the time domain. Once the daily cross correlations are computed, they are stacked to produce the final cross correlation.

The resulting cross correlations are two-sided time functions with both positive and negative time coordinates, i.e. both positive and negative correlation lags. We typically store the correlations from −1500 to 1500 s. The positive lag part of the cross correlation is sometimes called the 'causal' signal and the negative lag part the 'acausal' signal. These waveforms represent waves traveling in opposite directions between the stations.

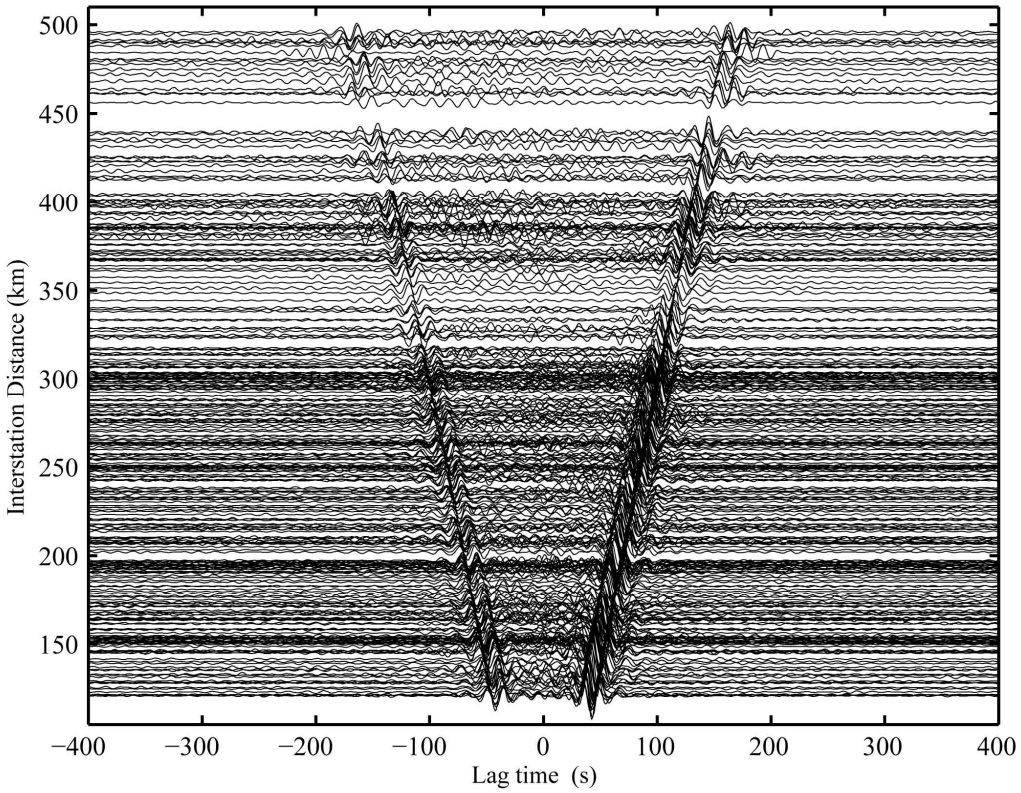

Figure 2-4. Bandpass filtered (10-50s) cross correlations as a function of distance and lag time. The cross correlation is time reversed if the amplitude of the negative component is smaller than the amplitude of the positive one. Only cross correlation with SNR greater than 25 are plotted.

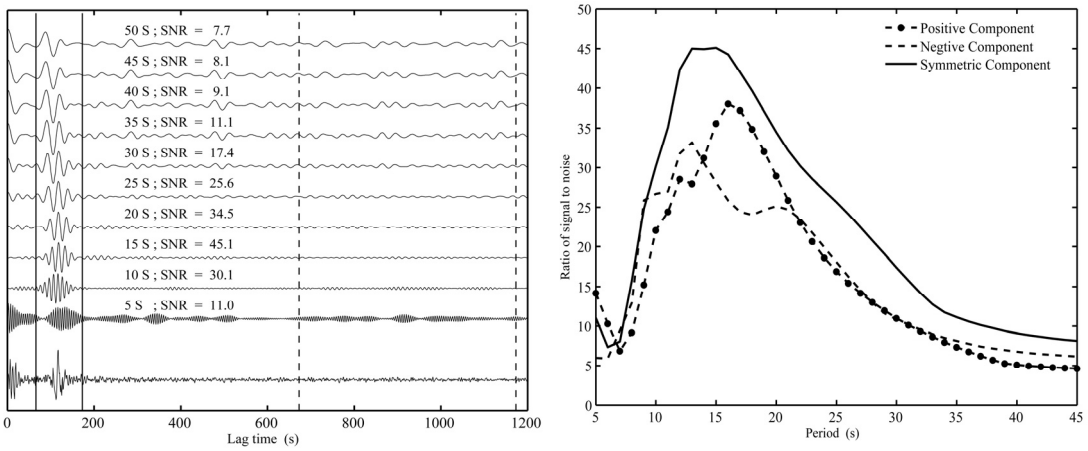

(a) (b)

Figure 2-5. Calculation of SNR. (a) The SNR of cross correlation obtained between GUY and CHL station. The bottom channel is the original cross correlation. Other channels are Gaussian filtered waveform. The characters in the panel show the center period of Gaussian filter and SNR value. (b) The SNR of the positive and negative lags of the cross correlation and the symmetric-component.

If sources of ambient noise are distributed homogeneously in azimuth, the causal

and acausal signals would be identical. However, considerable asymmetry in amplitude and spectral content is typically observed, which indicates differences in both the source process and distance to the source in the directions radially away from the stations. We often compress the two-sided signal into a one-sided signal by averaging the causal and acausal parts. We call this the 'symmetric' signal or component. Previous studies indicate that the symmetric signals can enhance the SNR (Bensen et al., 207; Lin et al., 2007).

Figure 2-4 shows an example of 14-month stacks of cross correlations plotted as a record-section. Clear signals are seen for both positive and negative correlation lags with physically reasonable moveouts (~3 km·s^{-1}).

In this study the SNR is defined as the peak signal in a signal window divided by the root mean square (RMS) of the trailing noise, filtered with a 10-30 s bandpass filter. The Rayleigh wave signal window is calculated by the inter-station distance divided by the group velocity windows (2-5 km/s). The noise window is 500 s in length that trails the end of signal window by 500s. It can be seen from Figure 2-5, the SNR of the symmetric component is higher than the positive and negative component in all period band.

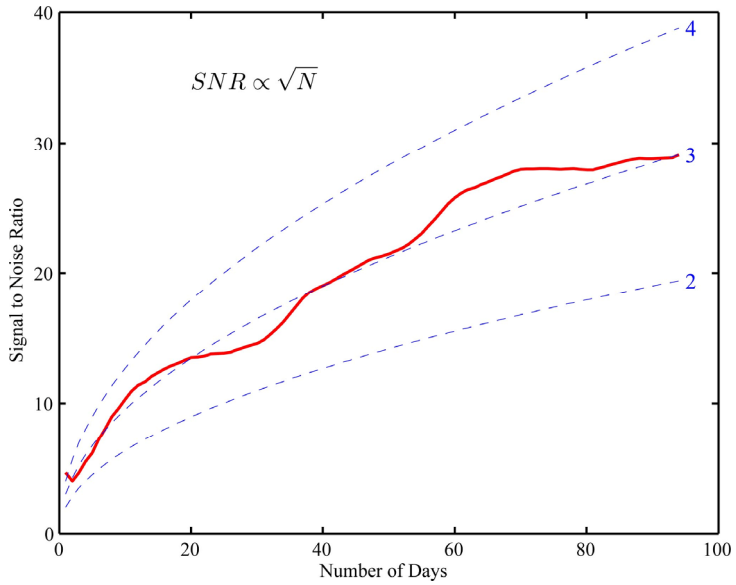

Figure 2-6. The relationship between SNR and cross correlation time for GUY and CHL station. A square root dependence is shown as the blue dotted lines.

We analyzed the relationship between SNR and cross correlation time. The SNR for each day shows moderate variation as the noise and seismicity varies (Figure 2-6). Based on the cross correlation time series for each day, we sum these to obtain the time

series for N number of days and compute the SNR. The accumulated SNR based on the summed traces shows clearly that the SNR increases proportional to the square root of recording time in agreement with Sabra et al. (2004).

2.3.4 Group velocity measurements

Rayleigh wave group velocity dispersion curves are determined using a multiple filter method (Dziewonski et al., 1969; Levshin et al., 1992; Liang et al., 2008). The implementation of this process is illustrated in Figure 2-7. Figure 2-7a is a typical cross correlation waveform obtained between two stations in North-China. The original seismogram is filtered using a series of Gaussian filters with central periods ranging from 4 s to 50 s. The envelope functions of the filtered seismograms, i.e., the FTAN (Frequency Time Analysis) spectrum, are plotted in Figure 2-7b with colors representing envelope amplitudes. This method constructs a 2D diagram of signal power as a function of time or group velocity and the central frequency or period of successive narrow-band Gaussian filters. The local power maximum along the period axis is picked. The group arrival times of the maximum amplitude as a function of filter period are used to calculate a group velocity curve.

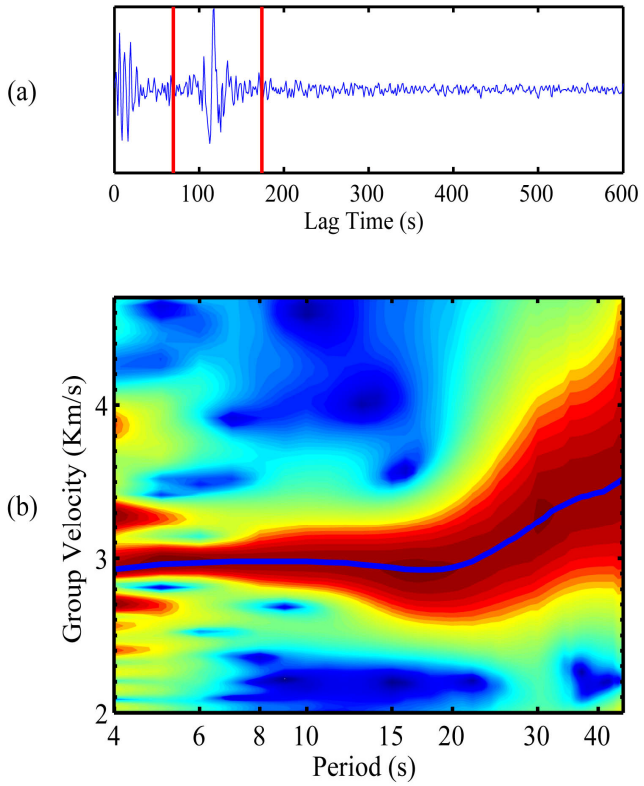

Figure 2-7. Example of dispersion measurement. (a) A typical cross correlation function obtained between two stations. (b) FTAN diagram obtained after multiple filter analysis.

2.3.5 Data selection

The number of inter-station path grows as the square of the number of stations, but not all paths can be used to obtain a high quality dispersion curve. In order to get a reliable tomography result and minimize workload, some data quality control criteria must be devised to identify and reject bad measurements. In this study, we use four criteria to select data, which are minimum inter-station distance, signal to noise ratio, cluster analysis and traveltime residual.

First, we apply a minimum three wavelengths inter-station distance constraint and we exclude paths shorter than 120 km. For closely spaced station-pairs, the signals at positive and negative lags can interfere with spurious precursory arrivals and each other at long periods, rendering the measurements unreliable. Since the average inter-station path length is about 300 km in NCSA, the minimum wavelength criterion significantly reduces the number of measurements at periods above 30 s because stations must be separated by more than 360 km.

Second, we apply a selection criterion based on the period-dependent SNR, which is defined as the peak signal in a signal window divided by the root mean square (RMS) of the trailing noise, filtered with a 10-30 s bandpass filter. The Rayleigh wave signal window is calculated by the inter-station distance divided by the group velocity windows (2-5 km/s). We store the cross correlations from -1500 s to 1500 s. The noise window is defined from 1000 s to 1500 s. We only select cross correlations with SNR≥7 and measure their dispersion curves.

Third, we apply clustering analysis to dispersion curves retrieved from ambient noise data. Clustering measurements obtained at a particular station from a set of earthquakes located near to one another is commonly used to assess uncertainties in earthquake dispersion measurements (e.g. Ritzwoller & Levshin, 1998; Pontevivo & Panza, 2002, 2006). We select dispersion curves with similar azimuths and similar distances obtained at a station. These dispersion curves are considered to be similar to each other, because they almost sample the same region. In some cases, one can get a very smooth, continuous but dubious dispersion curve. By using clustering analysis, we can verify the reliability of this kind of measurement and discard the questionable ones.

Chapter 3 Surface wave tomography of NC

3.1 Introduction

The Earth, to a first approximation, has a spherically symmetrical seismic velocity structure. Models such as PREM, IASPI91 and AK135 allow traveltimes of different seismic waves to be predicted. Departures from such predicted traveltimes are known as 'traveltime anomalies'. Seismic tomography addresses this problem: *Is it possible to construct Earth's 3-D structure by using the traveltimes?*

Seismic tomography is a technique which is used to generate three dimensional images of the inside of the Earth and thus represents one of the most powerful tools to explore its interior. Seismic tomography has its roots in the computed tomography (CT) scanning, a technique used in medicine to look inside the human body. Although the underlying theory is quite similar, in the medical imaging case, the source and receiver distribution is controlled by the operator, unlike the seismology where we can only control the locations of the receivers.

It is possible to use much more extensive observational material by incorporating data over 'mixed' paths, i.e., the ones traversing regions of different structures. If the ratio between the segments of a path corresponding to different regions varies with the path, then the velocities in each region can be estimated from the traveltimes for such paths. This possibility is based on the assumption that the medium is laterally homogenous within each region, the boundaries between them are known, while the effects of refraction and phase distortion at boundaries can be neglected.

Phase or group surface wave velocities observed along different paths are widely used to study the lateral variations and anisotropy of the lithospheric structures. The final aim of most of these studies is to map local values of the velocities and, if possible, to display azimuthal anisotropy for a set of periods. For determination of a 3-D model, the maps of local surface wave velocities are used. The 3-D model may be constructed by solving a set of 1-D inverse problems to determine vertical velocity and density distributions at each point of the area under investigation from corresponding dispersion curves. Montagner (1986) has shown that this approach is equivalent to 3-D inversion, if the vertical and horizontal velocity variations are decoupled. Such a two-step approach is more preferable than a direct 3-D inversion, because in this case

the calculations are much simpler. Thus the 3-D inverse problem using surface wave data may be separated into two independent problems: 2-D inversion for phase or group velocities for a fixed period, resulting in lateral variations of these velocities for a set of periods, and 1-D inversion for the vertical distribution of the elastic parameters, such as P and S velocities as well as density.

In surface wave inversions, the inverse problem is typically divided into two parts: A nearly linear part to estimate 2-D dispersion maps and a nonlinear part in which the dispersion maps are used to infer earth structure. It is the nearly linear part that we call surface wave tomography.

There are a number of surface wave tomographic techniques currently in use by several research groups around the world. These techniques differ in geometry (i.e., Cartesian versus spherical), model parameterization (e.g., glocal versus local basis functions), certain theoretical assumptions (particularly about wave paths and scattering), the regularization scheme, and whether azimuthal anisotropy can be estimated simultaneously with the isotropic velocities.

3.2 Surface wave tomography method

In this study, a generalized 2-D linear inversion procedure developed by Ditmar & Yanovskaya (1987) and Yanovskaya & Ditmar (1990) has been applied to construct the group velocity tomographic maps. This method is a generalization to two dimensions of the classical 1-D method of Backus & Gilbert (1968). The tomographic method estimates a group velocity map *U(x)* at each period by minimizing the following misfit function:

$$\alpha \iint |\nabla m(x)|^2 dx + (d - Gm)^T (d - Gm) = \min , \qquad (1)$$

where,

$$m(x) = (U^{-1}(x) - U_0^{-1})U_0 , \qquad (2)$$

$$d_i = t_i - t_{i0} , \qquad (3)$$

$$(Gm)_i = \iint G_i(x) m(x) dx = \int_{l_{0i}} m(x) \frac{ds}{U_0} , \qquad (4)$$

$$\iint G_i(x)dx = \int_{l_{0i}} \frac{ds}{U_0} = t_{i0}, \qquad (5)$$

In the relations (1–5), $x = x(\theta, \phi)$ is the position vector, U_0 is the velocity corresponding to a starting model, t_i is the observed travel time along the i_{th} path, t_{i0} is the travel time calculated for the starting model, α is a regularization parameter, l_{0i} is the length of the i_{th} path and s is the segment along which the inversion is performed. The parameter α controls the trade-off between the fit to the data and the smoothness of the resulting group velocity maps. We select a regularization parameter so that (a) the regionalised velocities are within the velocity range defined by the individual observed dispersion relations, and (b) the final unaccounted traveltime residuals are distributed randomly (Yanovskaya et al., 1998). Calculations of group velocity maps are made for several regularization parameters, α =0.05, α =0.1, α =0.2, α =0.3. Decrease in α gives a sharper solution region with an increase in solution error, whereas increase in α leads to smoothing of the solution region with decrease in solution error. Finally, we use the value of α =0.2, which gives relatively smooth maps with small solution errors.

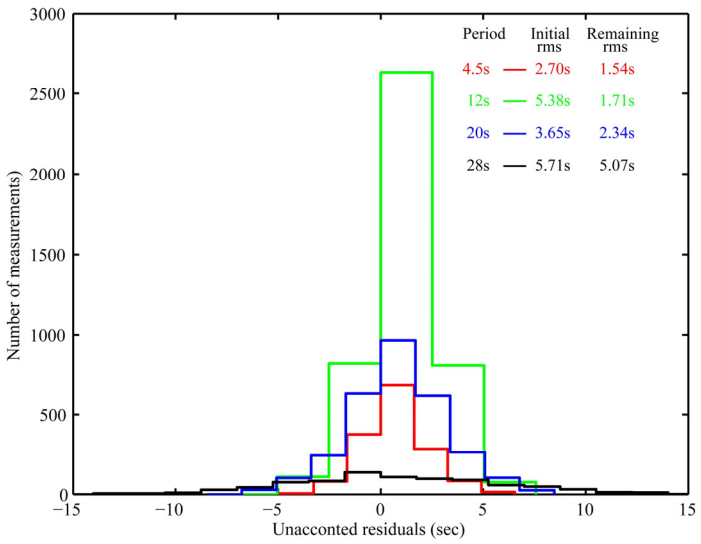

Figure 3-1. Histograms of final traveltime residuals for the four periods. The RMS of the initial (before tomography) and final (after tomography) group traveltime residuals at each period are indicated on the panel.

In order to ensure the quality of the solution, we compared the the initial mean square travel time residual and the remaining (unaccounted) residual, σ. Since it has been assumed that the unaccounted residuals are random, σ can be accepted as an

estimate of the standard error of the data. As soon as a solution for the lateral velocity variations is obtained, the remaining travel time residuals are calculated along all paths. Some of them may be large due to measurement errors and other factors. To reduce the effect of large errors, the data with the residuals larger than 3σ are rejected, and the procedure of tomographic reconstruction is repeated. Such selection of the data is performed several times, until no large residuals are remained in the data set. The histograms of the remaining residuals for the four periods are shown in Figure 3-1. The RMS of the initial travel-time residuals is about 5 s and the RMS of the final unaccounted residuals is about 2 s. These values are fairly small compared to those obtained when earthquakes are used in tomography.

3.3 Raypath distribution and density

The resolution of the group velocity maps depends mostly on the density of paths and on their azimuthal distribution (crossing paths). In our case, these two parameters depend on the geometry of the seismic array and on the distribution of the noise sources that can limit the number of available paths for some directions.

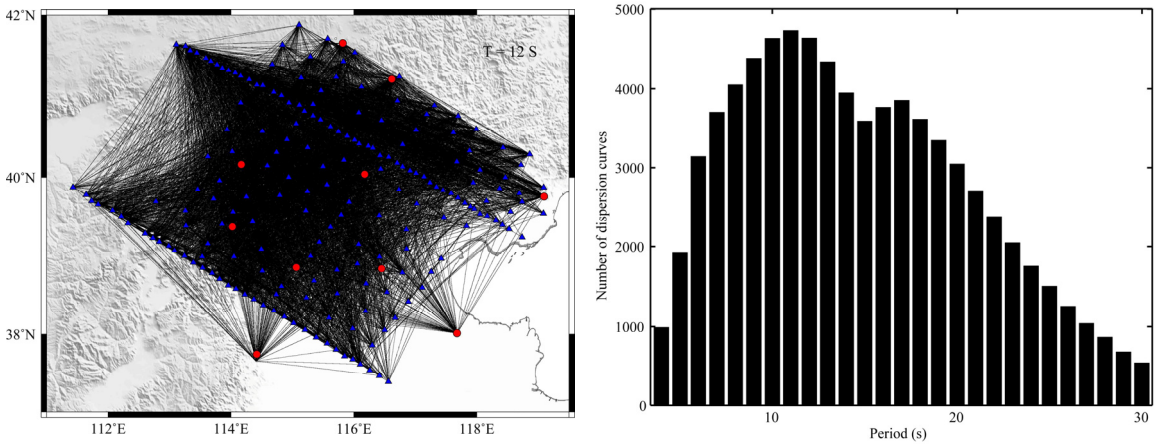

(a) (b)

Figure 3-2. (a) Map of the connecting raypaths between two stations for 12 s period. The blue triangles and red dots show the location of broadband and very broadband stations, respectively. (b) Number of raypaths used in the tomographic inversion respect to period.

Figure 3-2a shows the raypath distribution for 12 s period and Figure 3-2b shows the total number of raypaths for the selected periods which were used in this study to create the tomographic image. We use maximum cutoff period T as a data selection criteria. The dispersion curves are more affected by seasonal variation of ambient seismic noise for periods large than T. The average interstation distance is ~300 km

for NCSA, so the obtained dispersion curves mainly concentrate between 4 and 30 s period band. For 6-20 s period, the total number of raypaths exceeds 3000.

The raypath density diagrams for the four selected periods with cell size of 0.25°×0.25° are shown in Figure 3-3. The general coverage is sufficient except the margins of the study region. For most cells, the raypath density is larger than 300, with its maximum equal to 1314. The dense raypath distribution guarantees the reliability and the high resolution of tomography results.

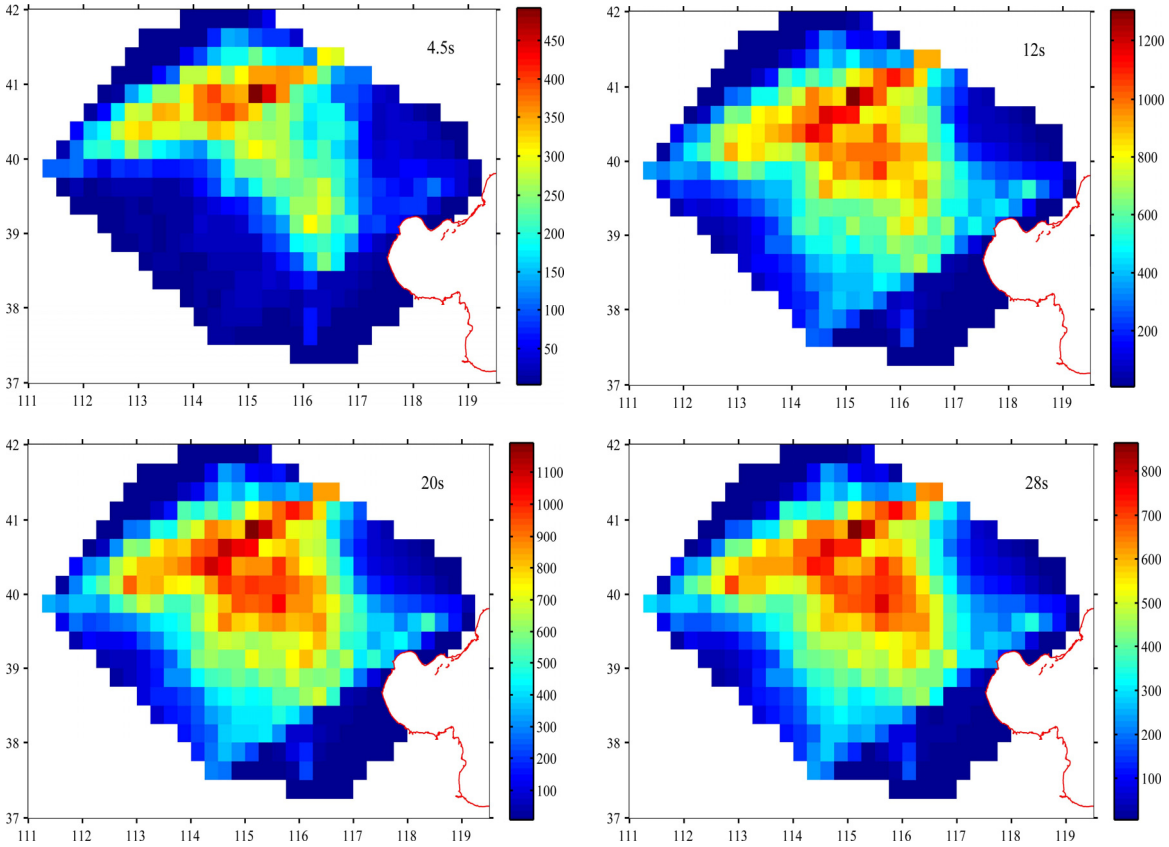

Figure 3-3. Path density diagrams from the data coverage for selected periods with cell size of 0.25°×0.25°. The period is indicated in the right-upper corner of each panel.

3.4 Resolution

As with any tomographic inversion, the resulting maps are not uniquely defined because the initial data do not constrain the seismic velocities at all points of the medium. Therefore, the knowledge of the resolving power is important in order to estimate the minimum really resolvable feature by a given data set and to sort out those features that may be numerical artifacts. Yanovskaya (1997) and Yanovskaya et al. (1998) proposed to use two parameters to estimate the lateral resolution: the mean

size and the stretching of the averaging area.

For 2D tomography problems, a function $S(x,y)$ for different orientations of the coordinate system is used in order to determine the sizes of the averaging area along different directions (Yanovskaya et al. 1998). The "averaging area'' which gives us an idea of the obtained resolution can be approximated by an ellipse centered at a point, with axes equal to the largest $S_{max}(x,y)$ and to the smallest $S_{min}(x,y)$ values of $S(x,y)$. The smallest $S_{min}(x,y)$ and largest $S_{max}(x,y)$ axes of the ellipse are calculated, and the resolution in each point is given by a single number, which is the mean size of the averaging area $L=(S_{min}(x,y) + S_{max}(x,y))/2$. As the resolution is closely correlated to the density of the crossing ray paths in each cell, it is clear that small values of the mean size of the averaging area (corresponding to high resolution) should appear in the areas that are crossed by a large number of ray paths and vice versa.

The second parameter is the stretching of the averaging area, which provides information on the azimuthual distribution of the ray paths and is given by the ratio

$$2[S_{min}(x,y) - S_{max}(x,y)]/ [S_{min}(x,y) + S_{max}(x,y)],$$

Small values of the stretching parameter imply that the paths are more or less, uniformly distributed along all directions; hence the resolution at each point can be represented by the mean size of the averaging area. On the contrary, large values of this parameter (usually > 1) mean that the paths have a preferred orientation and that the resolution along this preferential direction is likely to be quite small (Yanovskaya, 1997).

The mean size of the averaging area of our tomographic results is of the order of 25 km in most of the study region, but worsens near to the borders of the region where the path coverage is poor (Figure 3-4). This means that the areas of different tectonic structure with size > 25 km can be resolved in the solution from real data. The values of the stretching of the averaging area are between 0.1 and 0.75 in most of the study area at the four periods. This indicates that the azimuthal distribution of the paths is sufficiently uniform and that the resolution is almost the same along any direction.

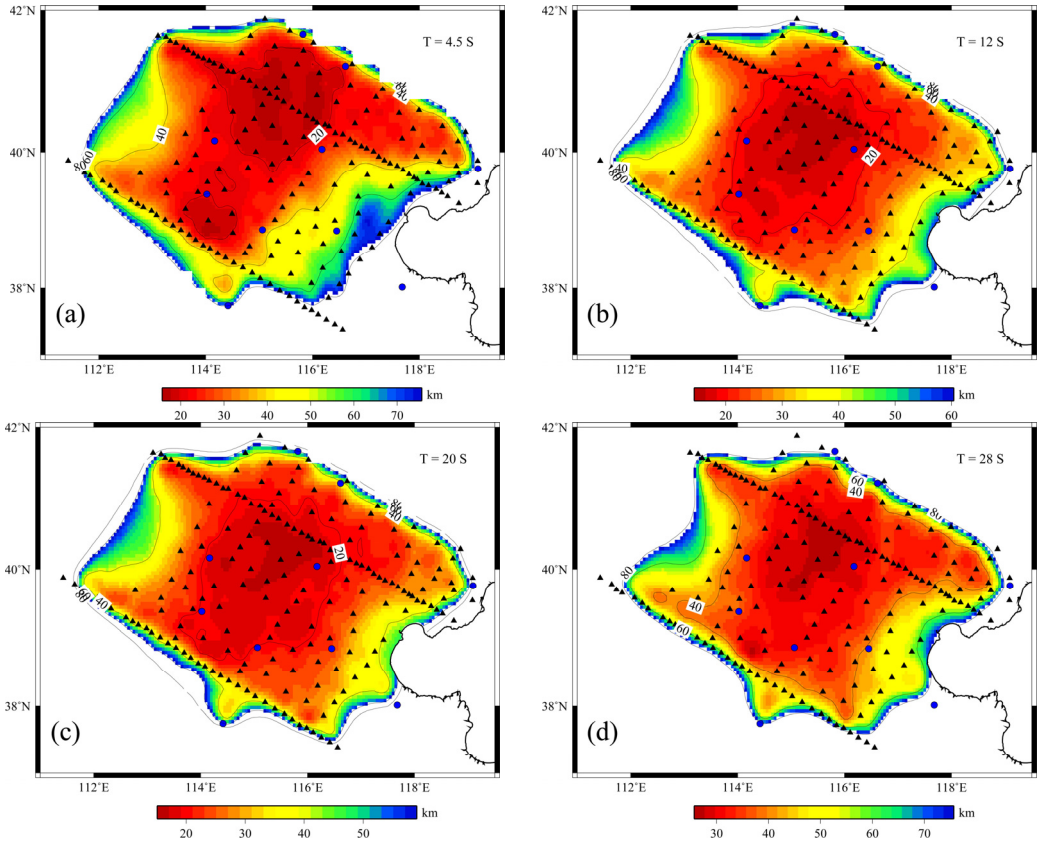

Figure 3-4. Resolution of the data as mean size of the averaging area in km at different periods. The black triangles and blue dots show the location of broadband and very broadband stations, respectively.

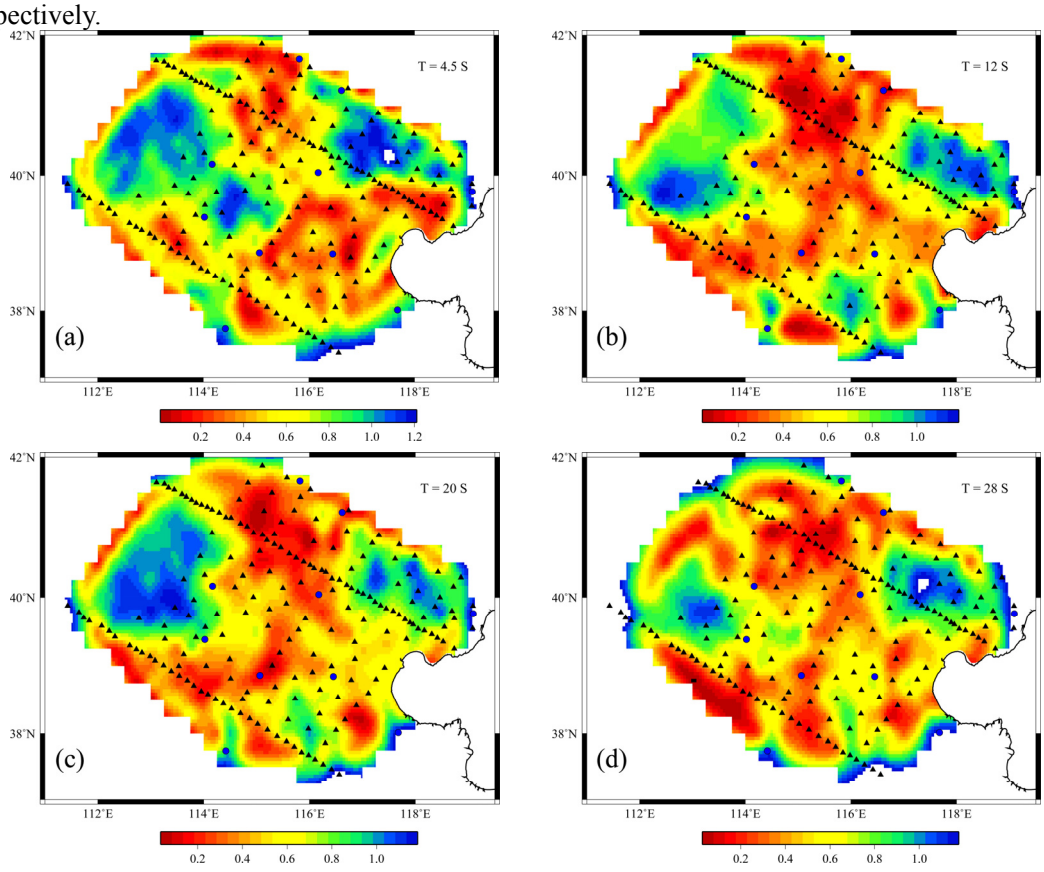

Figure 3-5. Resolution of the data as stretching of the averaging area at different periods. The symbols in this figure are same as those in Figure 3-4.

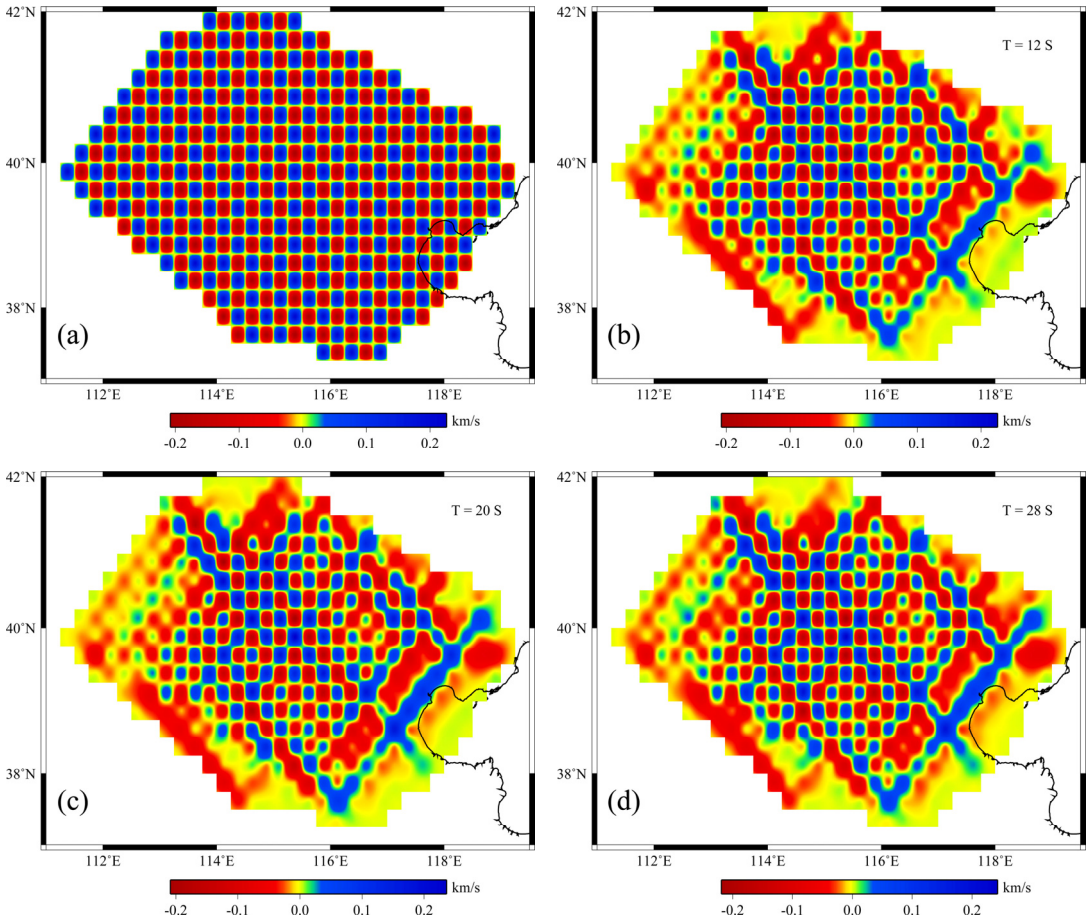

Figure 3-6. Checkerboard test results. (a) Theoretical model of 0.25º×0.25º. A velocity perturbation of ±7 percent with respect to the average group velocity for each examined period is assumed for the cells. (b), (c) and (d) are the inversion results for 12 s, 20 s and 28 s, respectively.

In order to further validate the tomographic results, we perform additional checkerboard tests (Figure 3-6). The study area is divided into 0.25º×0.25º cells and a velocity perturbation of ±7 percent with respect to the average group velocity for each examined period is assumed for the cells. Using this model, traveltimes along paths linking two stations are calculated. Then a solution for the velocity perturbation is obtained with the same parameters as for the real data. The estimations of the resolution obtained from the mean size of the area and the checkerboard tests indicate that it is reasonable to divide the study region into 0.25º×0.25º cells and that the anomalies with a surface extension of about 25×25 km^2 or larger are reliable.

3.5 Results and discussion

Using the tomographic method, as described in the previous section, Rayleigh wave group velocity maps at 4.5s, 12s, 20s and 28s have been produced. Surface waves

of different periods are sensitive to seismic shear wave speeds at different depths, with the longer period waves exhibiting sensitivity to greater depths. In order to guide the interpretation, the partial derivatives of Rayleigh wave group velocity with respect to shear wave velocity are calculated. The partial derivatives are computed analytically (Urban et al., 1993) for the AK135 model but with the crust replaced by a model based on DSS data gathered in North-China (Gao et al., 1993, Figure 3-7).

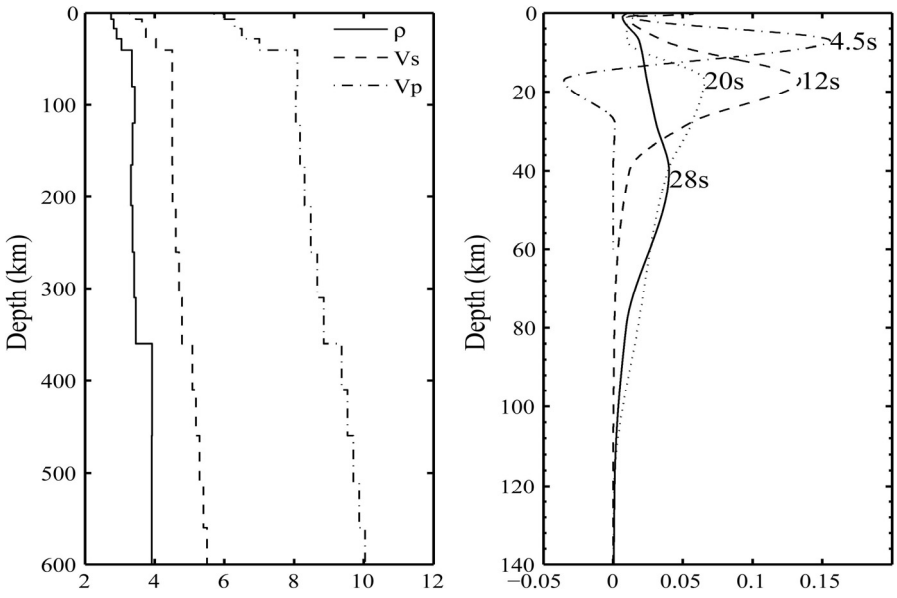

Figure 3-7. Analytical partial derivatives (Urban et al., 1993) of the group velocity of fundamental mode Rayleigh wave (right), computed with respect to shear wave velocity (left), at 4.5s, 12s, 20s and 28s. For each layer the partial derivative is normalized with respect to the layer thickness. The velocity profile comes from Gao et al. (1993).

At 4.5 s (Figure 3-8a), the shortest period of our tomography results, the partial derivative shows a peak at a depth of about 7 km. The group velocity map at 4.5s is therefore sensitive to variations of shear wave velocity at depths around 7 km and mainly reveals the characteristics of the uppermost crust, and can be correlated with the sedimentary cover thickness. The boundary between NCB and the surrounding mountain ranges is clearly outlined. A broad low velocity zone is observed at NCB, which is due to the large thickness of sediments. Zheng et al. (2005) derived the shear wave velocity model in NCB by inverting the receiver functions obtained at 44 temporary seismic stations. Their results indicate that the sedimentary cover of NCB is about 2-12 km thick. Taihangshan and Yanshan uplifts are imaged as high velocity zones. The Quaternary intermountain basins, such as Yanqing-Huailai, Yangyuan-Yuxian, Datong and Zhangjiakou show up as low-velocity anomalies. A small low velocity anomaly is observed between Fuping and Yuxian, which is

consistent with the location of the Lingqiu basin. In general, the group velocity map correlates very well with known geological structures. The resolution in the southeastern part (NCB) is relatively low because the local noise in this part is very strong and at the same time wave attenuation in the sediment basin is very strong, thus it is very difficult to obtain cross correlations with high SNR.

At 12 s period (Figure 3-8b), the resolution is improved by the increase of ray-paths and the group velocity map shows lateral variations as large as 1.2 km/s. Geologic units with small areas can be identified clearly and Jizhong depression, Cangxian Uplift and Huanghua depression are mapped as well. Affected by the thickness of sedimentary deposits, the Jizhong depression and Huanghua depression are mapped with relatively low velocities, while Cangxian uplift is mapped with high velocities. Taihangshan and Yanshan uplifts are mapped as high velocity anomalies. Yanqing-Huailai, Yangyuan-Yuxian and Datong basins still show up as low velocity anomalies. Using 30 DSS profiles, Jia & Zhang (2005a) studied the crust velocity structure of each sub-block in North-China. Their results reveal that the thicknesses of the sediment deposits in the Huanghua and Jizhong depressions are about 7-9 km and 6-10 km, respectively. Therefore the low velocity anomalies in the tomography maps at short period are an excellent indicator of the location and nature of the sedimentary basins in North-China, e.g. the extremely thick sedimentary deposit is the direct cause of the low velocity anomalies of Rayleigh wave in the Jizhong and Huanghua depressions.

Below the 20 s period, the tomography maps dominantly reflect low velocity anomalies caused by sedimentary basins. Almost all the basins are mapped as low velocity anomalies. However, at 20 s period the area of low velocity anomaly in the Jizhong depression is smaller, while the high velocity anomaly in the Cangxian uplift is larger; the velocity contrast between the sediment basin, such as Yangyuan-Yuxian and Yanqing-Huailai Basins, and its surrounding areas decreases (Figure 3-8c).

At 28 s period (Figure 3-8d), waves are primarily sensitive to depths between 30 and 50 km, namely, the lower crust velocity, the crust thickness and the uppermost mantle velocity. In this map the influence of the sediment basins decreases. The group velocity map at this period differs greatly from those obtained at 4.5 s, 12 s, 20 s. High velocity anomalies are observed in the eastern part of the study region, while low

velocity anomalies are observed in the northwest part. Thick crust tends to appear as low velocity anomalies and thin crust as fast anomalies on the map. Reflection and refraction profiles in North-China (Jia & Zhang, 2005a) show that the crust is relatively thin in NCB, while it is thick in the northwest part of our study region: the crust thickness is about 28-29 km in Bohai Bay, about 35-36 km in Beijing and more than 40 km to the west of Taihangshan fault.

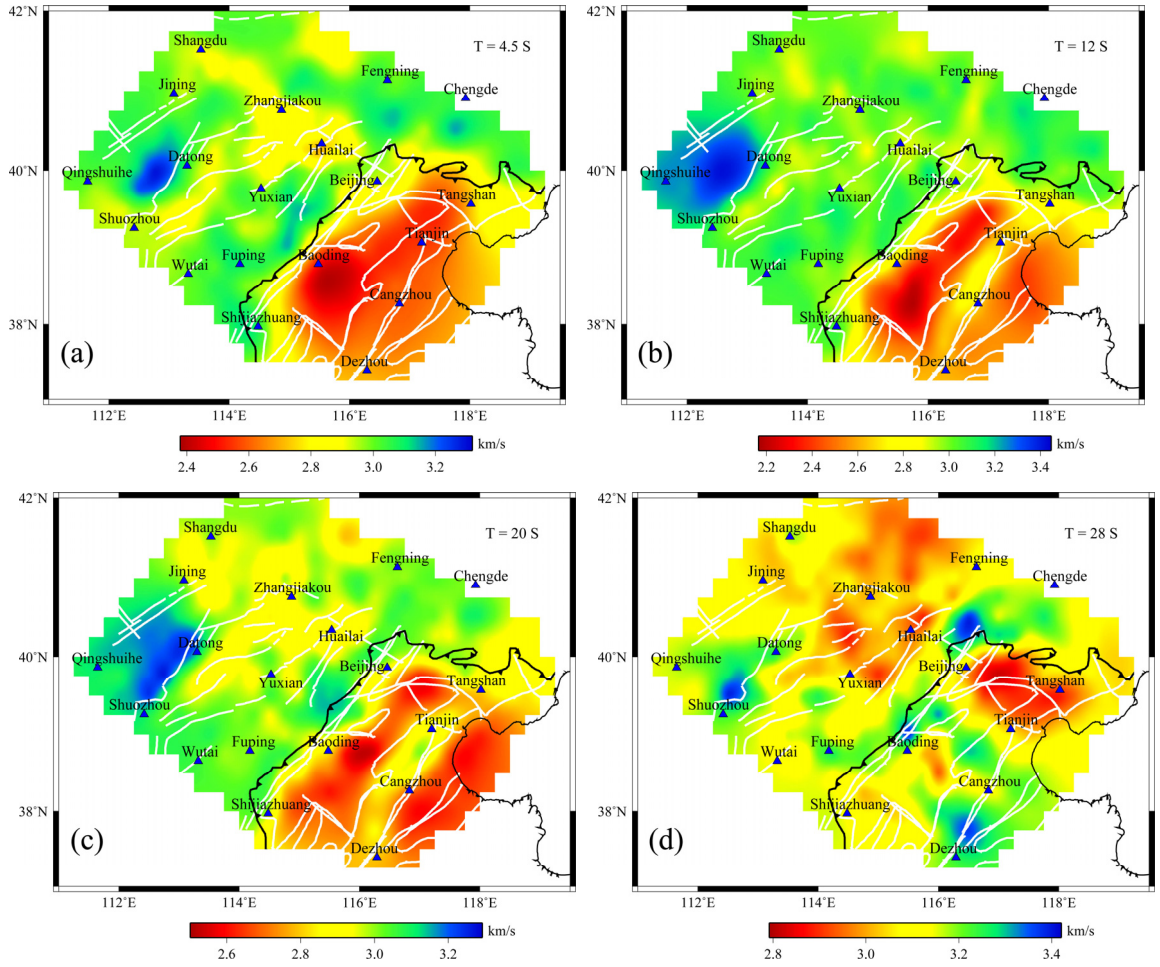

Figure 3-8. Rayleigh wave group velocity map at different periods. The blue triangles represent major cities in North-China. Some major boundaries and geological features are also shown at each panel as in Figure 1-2. The color scale changes between panels.

Group velocities at 28 s period show a well defined low velocity zone in the Beijing-Tianjin-Tangshan region (Figure 3-8d). In fact, Zhu & Zeng (1990) find a low velocity region in the Beijing-Tianjin-Tangshan region at 50 km of depth, which extends to 100 km depth beneath Tangshan and Tianjin, and, using regional seismic arrival data and Simultaneous Iterative Reconstruction Technique, Ding & Zeng (1994) reveal that a clear low velocity zone lies between Beijing and Tangshan in the 20-35 km

depth range. Recent body wave tomography shows a low velocity zone in the lower crust beneath the Beijing-Tianjin-Tangshan region (Huang & Zhao, 2004) as well. In our tomography results, the low velocity zone in the Beijing-Tianjin-Tangshan region can be seen from 23 s to 30 s. Tomography maps at these periods mainly reveal the velocity structures in the lower crust and uppermost mantle. We infer that the low velocity zone is related with the upwelling of hot mantle material. Seismic refraction and reflection profiles across Tangshan indicate that there is a 3-5 km offset of Moho discontinuity beneath Tangshan (Zeng et al., 1988). The hot material of the uppermost mantle may migrate to the crust along the offset of Moho discontinuity. The intrusion of mantle material heats up the lower crust and can cause the reduction of seismic velocity. A high conductivity layer has been found between 20 km to 30 km depth under this region using magnetotelluric soundings (Liu et al., 1989). Since the low velocity and high conductivity layer is usually related with fluids and partially melting materials, our results do not rule out the existence of fluids as suggested by Huang & Zhao (2004).

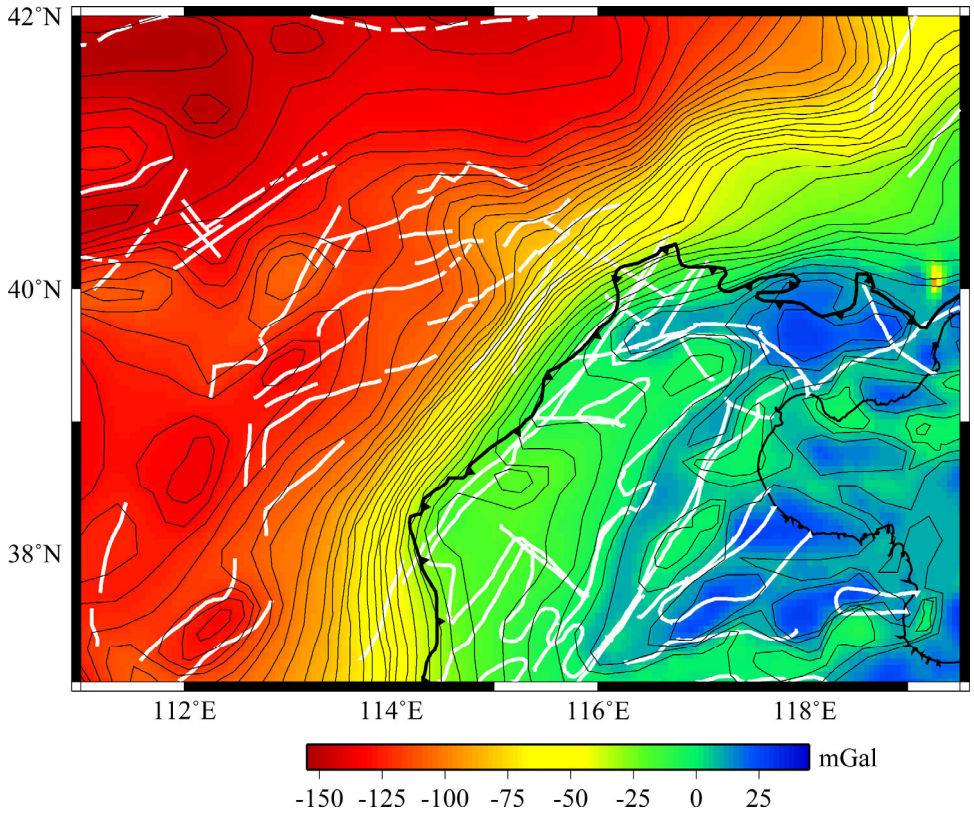

Figure 3-9. Bouguer gravity anomaly map in *mGal*, modified from Yin et al. (1989). Some major boundaries and geological features are also shown as in Figure 1-1.

From the tomography maps two further important features can be seen: (a) a high velocity zone near Datong, Shouzhou and Qingshuihe and (b) strong velocity gradient near the boundary between North-China basin and Yanshan-Taihangshan uplift. The

zone with high velocity Rayleigh wave near Datong, Shouzhou and Qingshuihe is located at the northeastern margin of the Ordos block that shares the typical features of cratonic lithosphere and hasn't been affected by the NCC re-activation. The block is characterized by low seismicity, low heat flow, positive vertical velocity gradient and lack of active fault and magmatic activity (Qiu et al, 2005). The trend of the strong velocity gradients seen near the boundary of the North-China basin and the Yanshan-Taihangshan uplift is nearly identical to that visible in the Bouguer gravity anomaly map (Figure 3-9, Yin et al. 1989), where, along the NE-SW-trending Taihangshan uplift, a continuous gradient zone is outstanding. The Taihangshan fault is within this gradient belt and P-wave tomography has shown that the fault cuts through the Moho interface and penetrates into the upper mantle (Huang & Zhao, 2004, Zhang et al, 2007). The belt represents a major lithospheric boundary and separates the NCC into western and eastern sectors, which can be shown to have fundamentally different architectures. Gravity anomaly values decrease from east to west and this indicates that the main density interface (Moho discontinuity) is deeper in the west. Thus both densities and velocity structures differ greatly on both sides of the Taihangshan fault.

Chapter 4 3D S-wave velocity structures beneath NC

4.1 Introduction

Surface wave dispersion data can be used to obtain the vertical shear-wave profile by inversion. Inversion is a challenging problem due to its highly non-linear nature and to the large numbers of local minima and maxima of the objective function. The inversion procedure follows the determination of the dispersion curve and allows reconstructing the vertical shear-wave velocity distribution from the observed dispersion curve.

In inversions of dispersion curves, a structural model is determined by fitting the observed dispersion curves with a theoretical curve. Generally, a dispersion curve is a nonlinear function of shear wave velocities, compressional wave velocities, densities, and thicknesses for each layer. To invert a dispersion curve into these parameters, usually a linearized approximation is used by neglecting higher-order terms in the Taylor series expansion. Then, an optimal solution is obtained by an iterative perturbation process based on linear inverse theory. However, the linear inversions results strongly depend on an assumed initial model. When an appropriate initial model can be generated using a priori information, linearized inversions can find an optimal solution that is the global minimum of a misfit function. However, if a priori information is either scant or unavailable, the inversion may find a local optimal solution.

Many nonlinear inversion methods are used to resolve the inversion problems. Search techniques such as Monte Carlo and hedgehog allow a large model space to be explored and produce multiple solutions (Keilis-Borok and Yanovskaya, 1967; Valyus, 1972; Panza, 1981; Shapiro et al., 2002). However these techniques become inefficient or impractical in very large model spaces (Lomax and Snieder, 1994, 1995). To tackle these problems, we use a nonlinear optimization method that uses a genetic algorithm (GA).

GA has been extensively applied in solving geophysical inversion problems. Stoffa and Sen (1991) used a GA in an inversion of 1D reflection seismograms. Wilson and Vasudevan (1991) estimated static corrections in reflection data processing by using a GA. Sambridge and Drijkoningen (1992) applied a GA to a waveform inversion

of reflection seismograms. In an earthquake study, Sambridge and Gallagher (1993) examined a GA-based inversion method of travel-time data for determining hypocenter locations. GA has also been used extensively in dispersion curve inversion (Lomax et al, 1994, 1995; Shi et al, 1995; Yamanaka et al, 1996; Wu et al, 2001; He et al, 2001, 2007; Pezeshk et al, 2005; Dal Moro et al, 2007; Suresh et al, 2008). Using an analogy to population genetics (i.e., where the operations are selection, crossover, and mutation), these algorithms can simultaneously search both globally and locally for an optimal solution by using several models. Since what is required in using a GA is only to compute the objective functions that are to be minimized, these algorithms are robust.

4.2 Fundamentals of GA

One of the main objectives of this study is to use a genetic algorithm (GA) to estimate shear-wave velocity profiles using dispersion curves. GA is an optimization and search technique that simulates the natural evolution process. GA is a global search method based on a stochastic approach, which rely on strategy of survival of the best fit (Holland, 1975). The results obtained in an inversion process using GA methodology are considered more dependable (Goldberg, 1989; Pezeshk and Camp, 2002) because:

* The GA approach is independent of initial information, so there is no need to determine a set of initial design parameters.

* GA is not gradient-based methodology; it uses objective function information and a probabilistic transition scheme with no use of gradient information.

* GA does not utilize the variables themselves; instead, it uses a coding set of variables.

* GA does not improve a single solution, it works on a population of possible solutions.

GA is based on the mathematical modeling of the mechanism of a genetic evolution strategy. GA does not rely on the specific relationship between the objective function and the boundary conditions. Basically, GA can be characterized as follows:

1. They work on a population of problem variables, which are usually created randomly. Variables are grouped in variable sets; each is called a string and composed of a series of characters that defines a possible solution for the problem. Characters in

each string are typically binary numbers, which are evaluated after decoding to real or integer numbers to represent the values of the discrete problem variables for a particular solution.

2. The performance of the problem variables, as described by the objective function and the constraints, is represented by the fitness of each string. A mathematical expression, called a fitness function, calculates a value for a solution of the objective function. The fitter solution gets the higher value and the ones that violate the objective function and constraints are penalized. Therefore, like what happens in nature, the fittest and best solutions will survive and get the chance to be a parent of the next generation.

3. In a crossover procedure, two selected parents reproduce the next generation. The procedure first divides the selected parent strings into segments, and then some of the segments of a parent string are exchanged with the corresponding segment of another parent string. One-point (Goldberg, 1989), multiple-point, and uniform crossover (Camp et al., 1998; Pezeshk et al., 2000) are among the several crossover patterns.

4. The mutation operation, which acts as an insurance policy (Goldberg, 1989), guarantees diversity in the generated populations. This is usually done by flipping (0 to 1 or vice versa) a randomly selected bit in the selected binary string to create a mutated string. Mutation prevents a fixed model of solutions from being transferred to the next generation. It allows for the possibility of generating children with nonexisting features from both parent strings.

4.3 GA inversion scheme

The most important parameters affecting Rayleigh wave propagation are shear-wave velocity and layer thickness. Two schemes are often used in inverting dispersion curves. The first way is to fix the layer thickness and only invert S wave velocity. When using this method, the layers are divided as thin as possible in order to adopt model velocity variations and jumps at interfaces. The second way is to invert layer thickness and S wave velocity simultaneously. In general, the first way will increase the uncertainty of inversion results, and rapid oscillations of the solutions are often observed. The second approach can reduce the total number of layers. However,

in practice, we don't know the depth of the interface and how many layers should be considered. In addition, the simultaneous inversion of velocity and thickness increases the computing time.

In order to overcome these problems, we develop an indirect smooth constraint in GA inversion (Wu et al., 2001). It's very difficult to apply smooth constraint in GA inversion directly. If the smoothed models are used in iteration, the diversity of models will be greatly suppressed and all models in population tend to be similar with each other after a few iterations. The optimal solution can't be guaranteed. We find that if we do not change the new models generated by selection, crossover and mutation, but modify the model for forward calculation, then the smooth constraint can be easily applied to model parameters in GA inversion.

The process of the method can be summarized as follows: firstly, the new model Vs_0 generated by selection, crossover and mutation is smoothed by equation (1) to produce model Vs, then the smoothed model Vs is used to calculate synthetic dispersion curves. The misfit of model Vs_0 is set to be identical with that of Vs and is used in the next iteration.

$$\begin{cases} Vs(h) = \dfrac{1}{E}\displaystyle\int_{h-h_0}^{h+h_0} Vs_0(y)e^{-\sigma(y-h)^2}dy \\ \\ E = \displaystyle\int_{h-h_0}^{h+h_0} e^{-\sigma(y-h)^2}dy \end{cases} \tag{1}$$

where Vs_0 is velocity model in GA iteration, Vs is the smoothed model; $h0$ is the number of layers used for smoothing. In our case, 3 layers are used for smoothing. However, this value can be adjusted by user. σ is the smooth coefficient. The value of σ depends on the need of model resolution. In general, the smaller σ is, the smoother the model will be. In inversion, σ can be chosen as a function of depth. For example, σ can be selected larger near the surface layer and Moho than in other depth in order to fit the possible high velocity gradient. Vs is only used for the forward calculation, but not in the search of model space. The method is similar to the smooth constraint used in linear inversion.

After many tests, we find if the layer thickness is thin (less than 3 km), the smooth parameter can be set to 0.2-0.4; if the layer thickness is thick (more than 5 km), the smooth parameter can be set to 0.5-0.7. The smooth parameters also vary with depth. At shallow depth, the smooth parameter can be set to ~0.6. At Moho and other discontinuities, the smooth value can be set to ~1.3.

The key element for any kind of optimization tool is the model evaluation, which is performed by means of an objective function *obj* that allows a quantitative estimation of the model. We considered the root-mean square value of the difference between the observed and calculated group velocities:

$$obj = \left[\frac{1}{n} \sum_{i=1}^{n} (v_{obs_i} - v_{cal_i})^2 \right]^{1/2} \qquad (2)$$

where n represents the number of observed frequency-velocity couples, v_{obs_i} is the observed phase velocity at the ith period and v_{cal_i} is the calculated velocity for the considered model (individual of the current population). This kind of formulation is also referred to as the $\ell 2$-norm.

4.3.1 Parameterization and priori constraints

Model parameterization strongly affects the inversion results. If the inversion is too weakly constrained, there will be a broad subset of models that will fit the data and large uncertainties will result at each depth. Much tighter constraints on the model space reduce the uncertainty in the estimated parameters, but the model will be increasingly subject to systematic errors.

A priori constraints on the model parameters are important not only to speed the inversion by limiting the volume of model space searched, but also define what we judge to be physically reasonable or plausible candidate models. For this reason, we collected the seismic reflection and refraction data, receiver function inversion data and receiver function *h-k* stack results (China Earthquake Administration, 1986; Wang 2008; Wang et al, 2009; Zheng et al, 2005, 2006, 2007; Luo et al, 2008; Xu et al, 2005, see Figure 4-1,).

The depth of Moho is obtained according to DSS data and receiver function *h-k*

stack results. In inversion, we don't fix the depth of Moho interface, but design a 5-layer model with 1 km thickness near the Moho interface. Shear wave velocities near surface (0-4 km) obtained by the receiver function inversion are used to set the search spaces in the uppermost crust. The compressional wave values are calculated using the relation between Vs and *Vp* (*Vp*=1.732**Vs*). When receiver function *h-k* data are available and the variance is less than 0.05, the ratio of *Vp* to *Vs* is set according to RF *h-k* data. The density is estimated using the Nafe-Drake relation (e.g. Fowler, 1995, Ludwig et al., 1970). The a priori constraints are applied to ensure that the selected models are physically plausible. A model is considered acceptable if the objective function is less than 0.04.

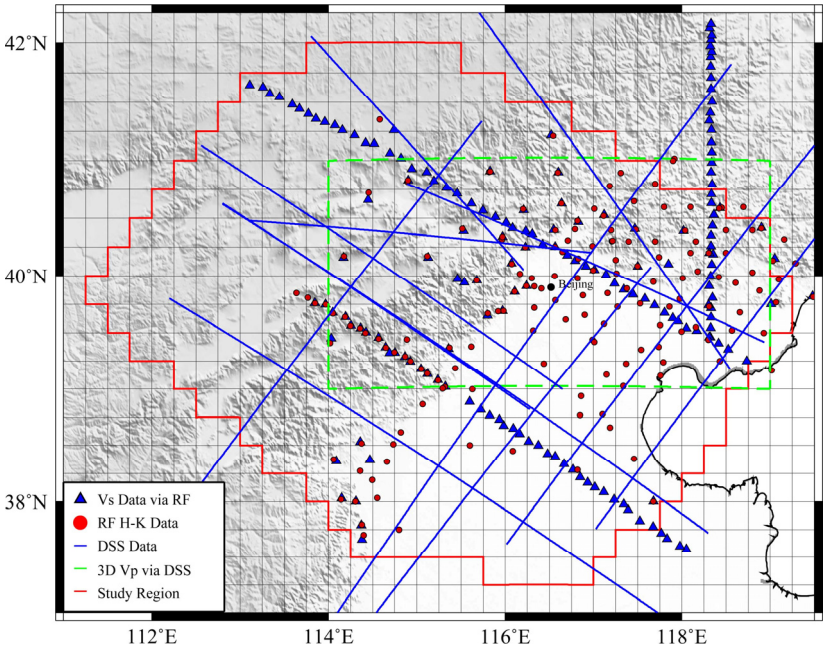

Figure 4-1. Assembled geophysical data. Blue triangles show points with shear velocity structure obtained via receiver function inversion. Solid red dots show points with Moho depth and Vp/Vs ratio obtained via receiver function *h-k* stack. Blue lines represent the location of DSS profiles. Green dotted rectangle shows area with 3D P wave velocity structures. The red line near the edge is our study area.

The maximum period used for inversion is 30 s. The partial derivatives of the group velocity of Rayleigh wave (Figure 3-7) shows that the dispersion curve data at this period is insensitive to shear wave velocity structures below 150 km. So we construct a starting model with 150 km thickness. The shear wave velocity structures below 150 km are from AK135 model.

4.3.2 Inversion examples

We tested the genetic inversion method explained above using synthetic Rayleigh wave group velocities. The synthetic dispersion curves are calculated using fast Schwab-Knopoff method (Schwab 1970; Schwab and Knopoff 1972). The structural model we used is shown in Figure 4-2a (red line). This is a four-layer model. Group velocities for the fundamental Rayleigh wave were calculated in a period range from 4 to 70 sec. Two tests were conducted to examine the performance of GA. We set the population size Q at 40, crossover probability at 0.8, and mutation probability at 0.015 in the two tests. We terminated the iterations after 150 iterations.

Firstly, we construct a model with four layers and the thickness of each layer is similar with the real model. We searched for an optimal solution of S wave velocity structure. The structural model obtained from the inversion by the modified GA method is shown in Figure 4-2a. The true S-wave profile was reconstructed well by the inversion. The comparison between the synthetic and inverted group velocities can be seen in Figure 4-2b, showing that the synthetic data were perfectly reproduced by the inversion. The results demonstrate that the true model can be well recovered by inversion, and thus show the robustness of GA inversion.

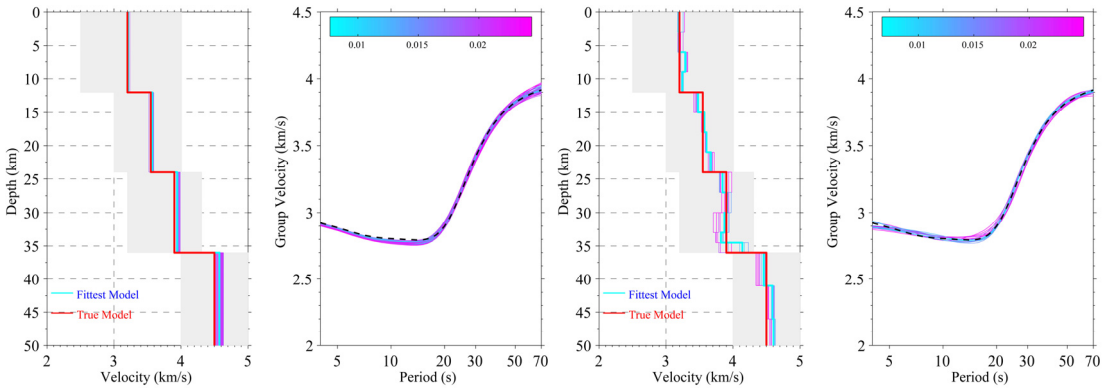

Figure 4-2. Shear velocity structure obtained by GA inversion. The gray shaded area in (a) and (c) are search space of S wave velocity in each layer. The color codes in (b) and (d) represent misfit values. The red line in (a) and (b) shows the true model and the cyan one indicates the fittest model.

In a real case, the thicknesses of each layer are unknown, so we construct a model with many thin layers. The thickness of each layer is 2 km in the crust and 5 km in the mantle. The inversion results show that not only the absolute S wave velocity, but also the thicknesses of each layer can be well reconstructed (Figure 4-2c, d). The minimum misfit value obtained at each generation is shown in Figure 4-3. The misfit value

decreased rapidly in the first 40 generations and then gradually in the next 110 generations. This gradual decrease suggests convergence near the minimum solution.

The results from the two tests show a very good agreement between the calculated output group velocities and the input experimental group velocities.

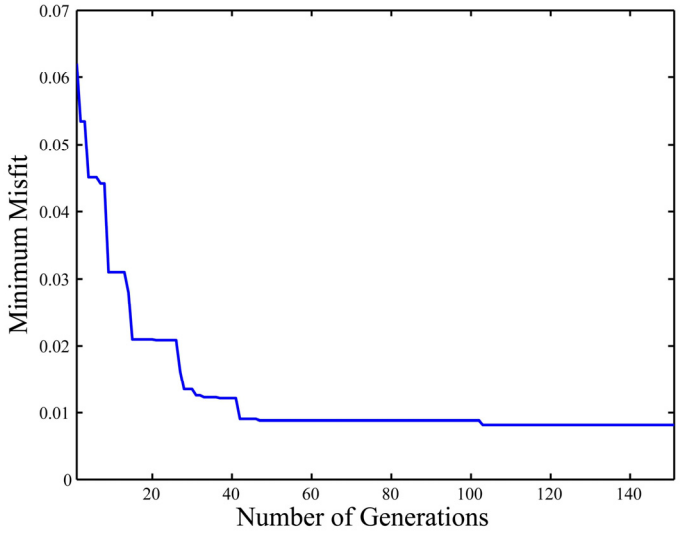

Figure 4-3. Minimum misfit value as a function of generation.

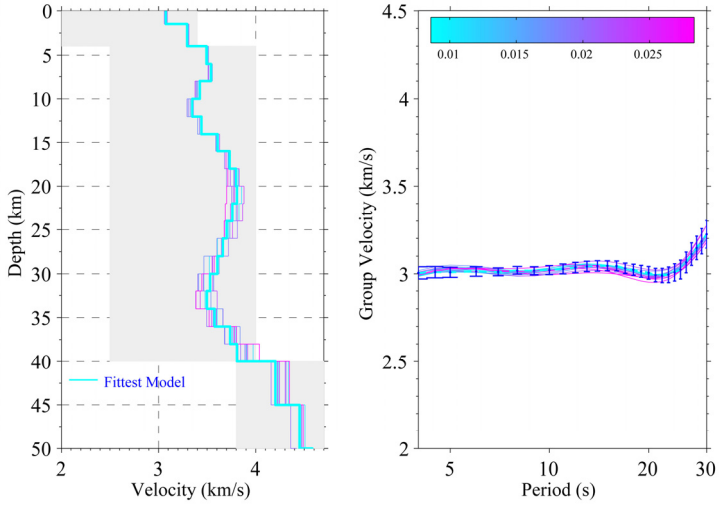

(a) (b)

Figure 4-4. Inversion results of a cell. (a) shows S wave velocity structures，(b) shows observed and synthetic dispersion curves. The cyan line in (a) and (b) indicates the best-fit model and dispersion curve, respectively. The gray shaded area in (a) is the search space of S wave velocity in each layer. The color codes in (b) represent misfit values. The error bars in (b) are standard errors of tomography.

Using the GA inversion procedure, shear wave velocity structures of a cell is obtained (Figure 4-4). The velocity structures are consistent with DSS interpretation profile and receiver function inversion results.

4.4 Results and interpretation

We construct a 'favoured model' developed through GA inversion at each gridpoint. Combining these 1-D isotropic models, we obtain a 3-D shear wave velocity model for the North-China, with depth range from the surface to about 50 km.

4.4.1 Reliability of inversion results

Zhang et al. (1997) determined the velocity structure along Wenan-Yuxian-Chahaer by performing 1-D and 2-D ray tracing traveltime fitting and calculation of synthetic seismograms from DSS data. We select a profile that is the same as Zhang et al. (1997) and compare the results. It can be seen the main features are similar (Figure 4-5), such as the thickness of sedimentary cover, the variation of Moho interface, the low velocity zone between Jining and Yanggao in the upper crust, the low velocity zones in the upper and lower crust in the east of Tianzhen. These similarities validate the reliability of our inversion results.

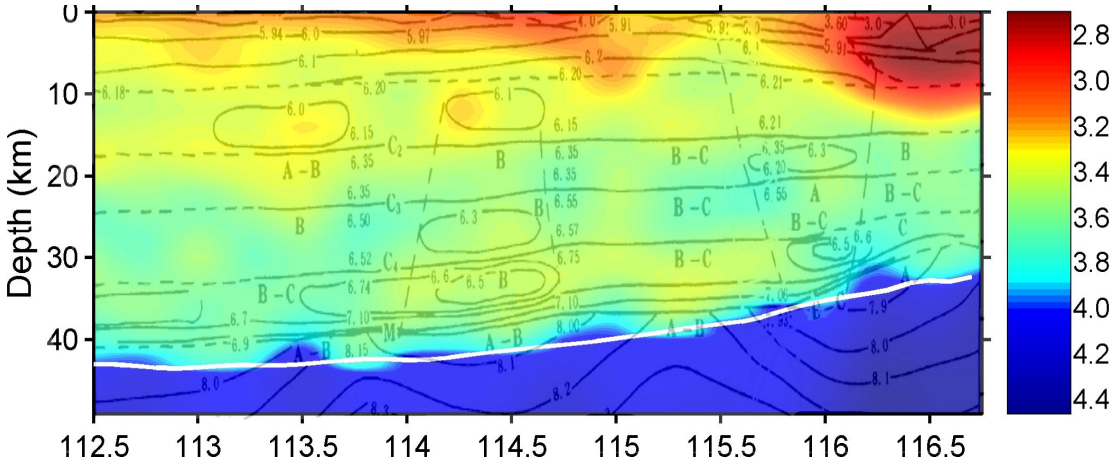

Figure 4-5. A comparison of velocity structures obtained by two methods. The color map shows the surface dispersion inversion results, while the contours shows the interpretation of DSS profile.

4.4.2 The thickness of sedimentary cover

Song et al. (1997) obtained the crystal basement velocities in NC using tomographic back projection method with Pg waves from 28 DSS profiles. Their results indicate the P-wave velocities in the crystal basement vary from 5.9 to 6.35 km/s. The laboratory experiment shows that the ratio of Vp to Vs is very large in sediments, and often larger than 2 (Chen & Li, 2003). In this study, we use Vs=3.2 km/s as a criterion

to determine the thickness of sedimentary cover. The distribution of sedimentary cover thickness is shown in Figure 4-6a.

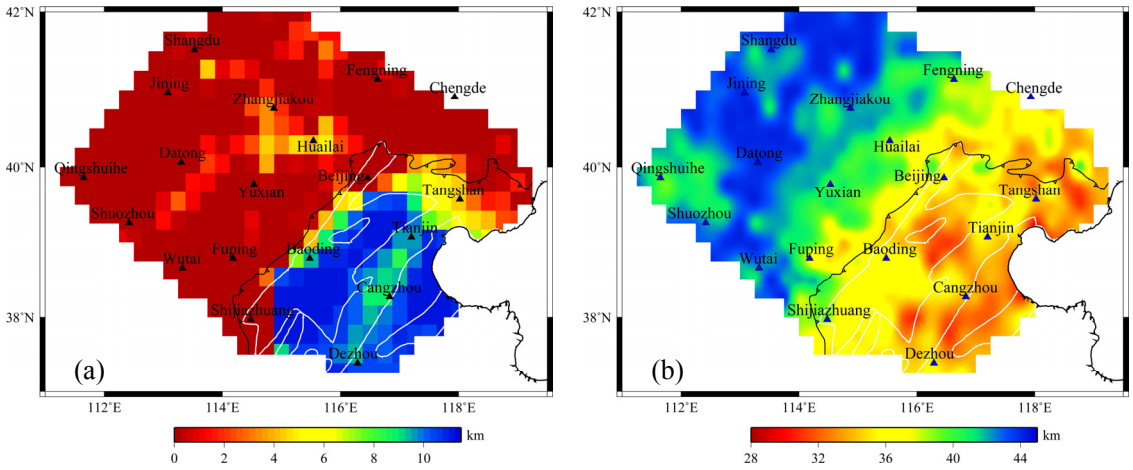

Figure 4-6. Sedimentary cover thickness map and crustal thickness map.

The thickness of sedimentary cover in the northwestern part is shallow, in Taihangshan uplift and Yanshan uplift is less than 2 km, about 3 km in Datong basin, and about 4 km in Yanqing-Huailai basin. The thickness is more than 6 km in NCB, about 8 km in Cangxian uplift, and about 11 km in Jizhong depression and Huanghua depression. The thickness of sedimentary cover varies from 2 km in the mountain ranges to 7 km in NCB. This is consistent with the topography in the region. Previous studies show that the thickness of sedimentary cover in Jizhong depression and Huanghua depression is about 7-9 km (Editorial Group of "The 1976 Tangshan Earthquake", State Seismological Bureau). The DSS results also suggest that the sedimentary is thin in the mountain ranges, about 1-2 km, while it is thick in NCB, about 6-10 km in Jizhong depression and about 2-4km in Cangxian uplift (Jia et al., 2005a). This is consistent with our results. However, previous studies can only give the thickness of sedimentary cover along the DSS profiles, but our results give the thickness of sedimentary cover of the whole region. We must keep in mind, since the layer thickness is about 0.5-1 km in the model and we apply the smooth constraint, so the error of thickness is about 1 km.

Figure 4-6b shows the thickness of crust. The lateral variation of crustal thickness is very large, the maximum difference in thickness reaches 16 km. In general, the crust is thin in the eastern part, while thick in the western part. The crustal thickness increases from 28 km in the Bohai gulf to 44 km in Shanxi highland and Zhangjiakou. The crustal

thickness in Huanghua depression, Cangxian uplift and Tangshan is relative thin, about 32 km, about 32-36 km in Jizhong depression.

Many researchers have studied the crustal thickness of North China using DSS profiles and receiver function *h-k* stack method. Reflection and refraction profiles in North-China (Jia & Zhang, 2005a) show that the crust is relatively thin in NCB, while it is thick in the northwest part of our study region: the crust thickness is about 28-29 km in Bohai Bay, about 35-36 km in Beijing and more than 40 km to the west of Taihangshan fault. Our results are also consistent with the receiver function *h-k* stack results (Figure 4-7, Xu et al., 2005; Wang et al., 2009). Due to the limitations of the method, the DSS profiles and receiver function *h-k* stack method can only give the crustal thickness along the profile or beneath the station. Our method gives the crustal thickness at each knot and the resolution is higher than the traditional methods.

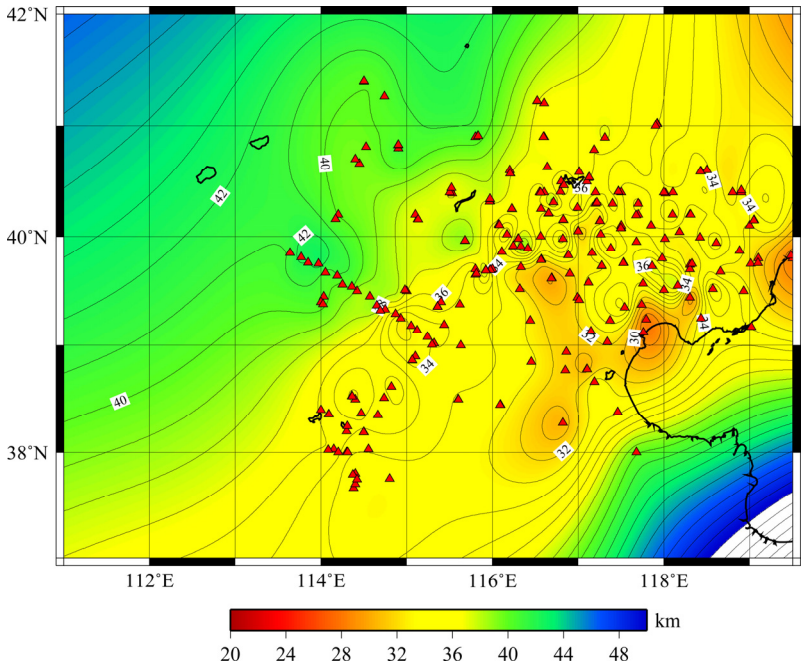

Figure 4-7. The lateral variation of Moho depth retrieved by the receiver function *h-k* stack.

4.4.3 S-wave velocity structures at different depths

Horizontal slices of shear wave speed at a selection of depths are shown in Figure 4-8, including 1, 8, 10, 12, 27 and 36 km.

The most striking features at 1 km depth are several large sedimentary basins. The NCB, Yanqing-Huailai Basin and Datong Basin clearly appear as low velocity anomalies. A broad low velocity zone is observed at NCB, which is due to the large

thickness of sediments. Zheng et al. (2005) derived the shear wave velocity model in NCB by inverting the receiver functions obtained at 44 temporary seismic stations. Their results indicate that the sedimentary cover of NCB is about 2-12 km thick. Taihangshan and Yanshan uplifts are imaged as high velocity zones. In general, the shear wave velocity structure at 1 km correlates very well with known surface geological structures.

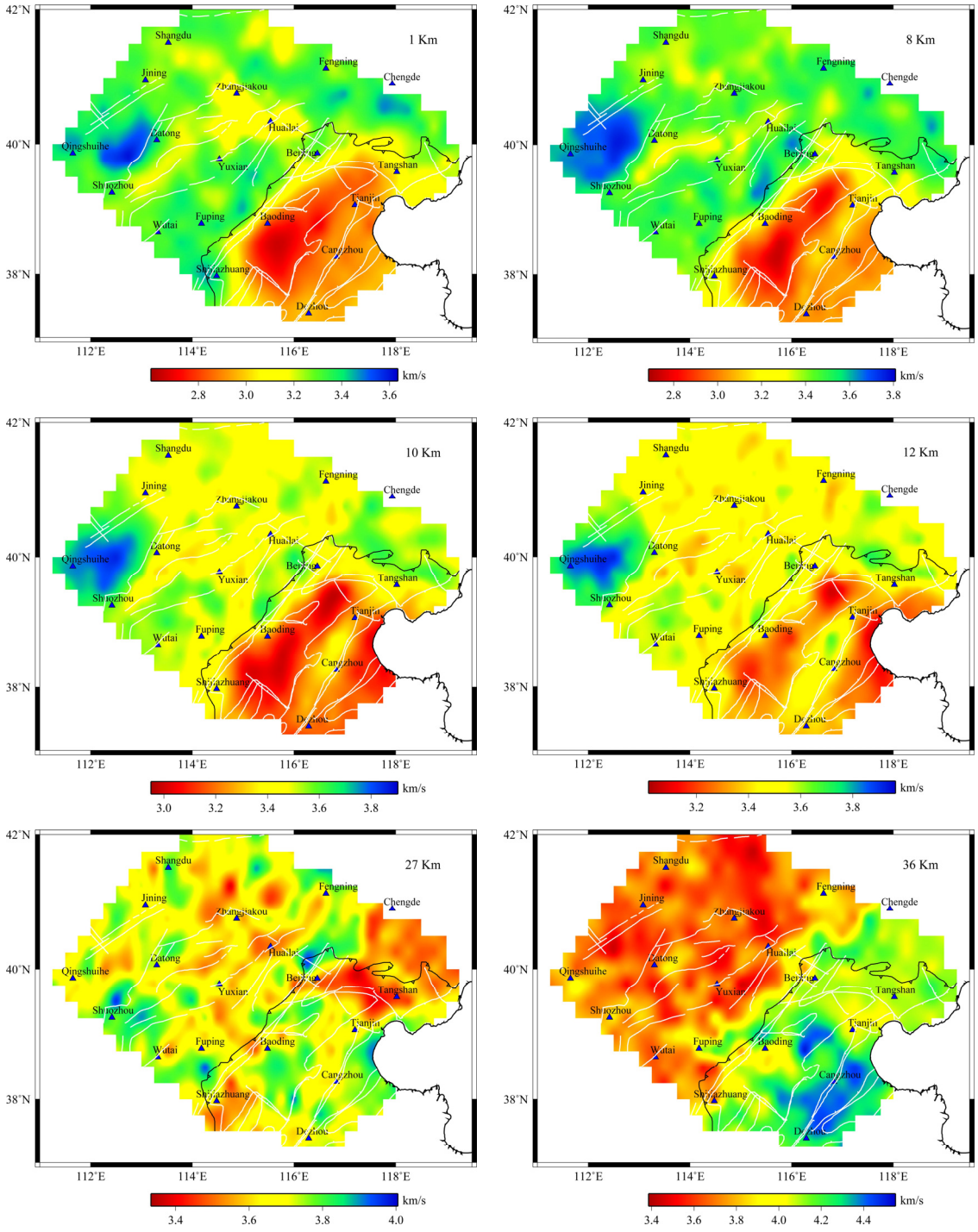

Figure 4-8. Horizontal slices of S-wave velocities at different depths.

At 10 km and 12 km depths, Jizhong depression, Cangxian Uplift and Huanghua depression are mapped very well. At 36 km depth, high velocity anomalies are observed in the eastern part of the study region, while low velocity anomalies are observed in the northwest part. Thick crust tends to appear as low velocity anomalies and thin crust as fast anomalies on the map.

A high velocity zone near Datong, Shouzhou and Qingshuihe is observed at 1-23 km depth. The high velocity zone is located at the northeastern margin of the Ordos block that shares the typical features of cratonic lithosphere and hasn't been affected by the NCC re-activation. The block is characterized by low seismicity, low heat flow, positive vertical velocity gradient and lack of active fault and magmatic activity (Qiu et al, 2005). The inversion results reveal the stable characteristics of this region.

Strong velocity gradient near the boundary between North-China basin and Yanshan-Taihangshan uplift can be seen at 1-12 km depth. Below 13 km, the high and low velocity anomalies near Taihangshan front fault become blurry, and only can be visible in some parts. We thus argue that the Taihangshan front fault does not penetrate through the Moho discontinuity along the whole fault, probably penetrate through the Moho discontinuity in some region. P-wave tomography has shown that the fault cuts through the Moho interface and penetrates into the upper mantle (Huang & Zhao, 2004, Zhang et al, 2007). The discrepancy may be caused by different methods and different characteristics of P and S waves.

A well defined low velocity zone in the Beijing-Tianjin-Tangshan region is imaged at 22-30 km. This is consistent with many tomography studies in this region. Zhu & Zeng (1990) find a low velocity region in the Beijing-Tianjin-Tangshan region at 50 km of depth, which extends to 100 km depth beneath Tangshan and Tianjin. Using regional seismic arrival data and Simultaneous Iterative Reconstruction Technique, Ding & Zeng (1994) reveal that a clear low velocity zone lies between Beijing and Tangshan in the 20-35 km depth range. Recent body wave tomography shows a low velocity zone in the lower crust beneath the Beijing-Tianjin-Tangshan region (Huang & Zhao, 2004) as well. In our tomography results, the low velocity zone in the Beijing-Tianjin-Tangshan region can be seen from 22 km to 30 km. We infer that the low velocity zone is related with the upwelling of hot mantle material. Seismic refraction and reflection profiles across Tangshan indicate that there is a 3-5 km offset

of Moho discontinuity beneath Tangshan (Zeng et al., 1988). The hot material of the uppermost mantle may migrate to the crust along the offset of Moho discontinuity. The intrusion of mantle material heats up the lower crust and can cause the reduction of seismic velocity. A high conductivity layer has been found between 20 km to 30 km depth under this region using magnetotelluric soundings (Liu et al., 1989). Since the low velocity and high conductivity layer is usually related with fluids and partially melting materials, our results do not rule out the existence of fluids as suggested by Huang & Zhao (2004).

4.4.4 Connection between velocity structure and occurrence of strong earthquakes

The North China area is one of the most seismic active areas in China. Historical strong earthquakes occurred frequently in this area. More than 200 earthquakes with magnitude greater than 5.0 have occurred in this region since 780 BC, among them 37 events are larger than M= 6.0 and 10 events are larger than M= 7.0 (The Earthquake Disaster Prevention Department of China Earthquake Administration, 1995, 1999; China Earthquake Networks Center, 2008). Three strong earthquakes occurred in North China since modern seismometers. The three earthquakes are Tangshan earthquake, Luanxian earthquake and Ninghe earthquake.

The 1976 Tangshan earthquake sequence consists of three large earthquakes: (1) the mainshock (M= 7.8) occurred on July 28, 1976 right beneath the Tangshan city; (2) the largest aftershock (M= 7.1) (also known as Luanxian earthquake) occurred 15 h after the mainshock and was located about 25 km northeast of the main shock hypocenter under Luanxian; and (3) the second largest aftershock (M= 6.9) (also known as Ninghe earthquake) occurred on November 15, 1976 west of Tangshan under Ninghe city. The focal depths of the three events were determined by the seismic network to be 11.0, 10.0 and 17.0 km. The focal depths obtained by waveform modeling are 13.0, 8.2 and 17.5 km (Nabelek and Chen, 1987). In this study, we use the average values as the focal depths. We select a profile crossing the epicenters of the three earthquakes and study their relationships (Figure 4-9).

We find that the focal depth of Ninghe earthquake is located in the transition zones of high and low velocity bodies. The focal depths of Tangshan and Luanxian earthquake are located in high velocity bodies. There is a low velocity zone beneath the focuses of Tangshan and Luanxian earthquake. Moho interface is locally uplifted in

Ninghe and Luanxian. The S-wave velocity is lower in the uppermost mantle of these three earthquake regions.

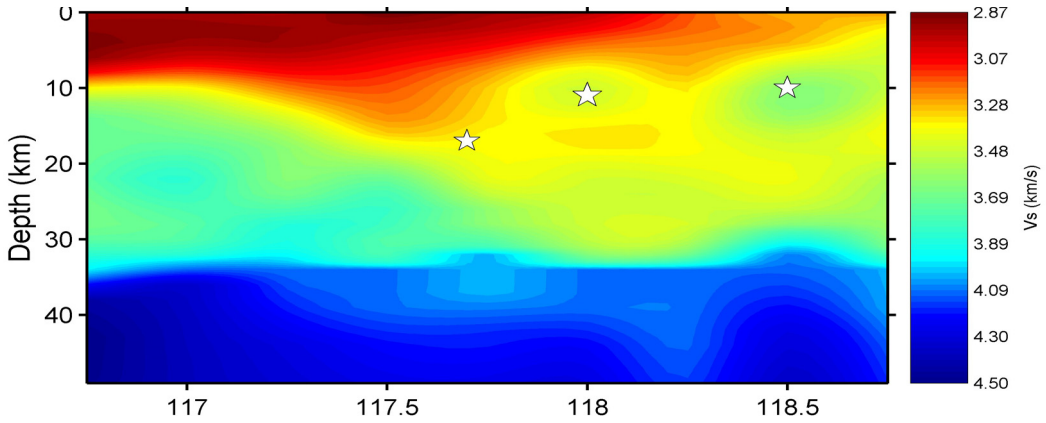

Figure 4-9. A velocity structure profile crossing Ninghe-Tangshan-Luanxian large earthquake source region. From left to right, the stars in the profile show the focal depths of Ninghe, Tangshan and Luanxian earthquakes.

Liu et al. (1989) determined the geoelectric structure in the Tangshan area using magnetotelluric soundings and revealed a high-conductivity anomaly below 20 km depth under the epicenter of the Tangshan earthquake. Similar low velocity and high-conductivity anomalies are also found in the source areas of the 1995 Kobe earthquake in Japan and the 2001 Bhuj earthquake in India (Zhao et al., 1996; Mishra and Zhao, 2003). Huang et al. (2004) argue that the high-conductivity and low-velocity anomaly in the lower crust under Tangshan shows the existence of fluids in the earthquake source region.

We infer that these three earthquakes were mainly caused by vertical deformation of upper mantle and material exchange between crust and upper mantle. Seismic refraction and reflection profiles across Tangshan indicate that there is a 3-5 km offset of Moho discontinuity beneath Tangshan (Zeng et al., 1988). The magma intrudes crust along faults near the boundary of crust and upper mantle, which leads to the low velocity anomaly in the uppermost mantle. The magma intrusion heats up the lower crustal material and drops the viscosity. Some minerals are dehydrated. The water move up and store in the middle crust. The presence of liquids affects the structure and composition of fault zone, further changes the stress state, weakens the seismotectonic region and triggers the earthquakes.

4.5 Conclusions

From our successful inversions of synthetic and observed Rayleigh wave group velocities, we confirmed that GA can be applied to the inversion of surface wave dispersion data. GA is especially applicable when we cannot prepare appropriate initial models needed in the linear inversion methods. Since GA requires only calculating a forward model, they were easily incorporated in the inversion of dispersion data as well as other geophysical inverse problems.

Chapter 5 Noise characteristics in NC

5.1 Introduction

It has been recently demonstrated that the time cross correlation function of random seismic wavefields such as seismic coda (Campillo and Paul, 2003) or seismic noise (Shapiro and Campillo, 2004) computed between a pair of distant stations contains the actual Green function between the two stations (Campillo, 2006). This provides us with the possibility to retrieve the propagation properties of deterministic seismic waves along long paths by analyzing microseisms only. The emergence of the Green function is effective only after a sufficient averaging. In the case of diffuse coda waves, the averaging is performed over a set of earthquakes (Campillo and Paul, 2003; Paul et al., 2005). With the seismic noise (in the following, we use the term noise for the microseism which actually have no relation with instrumental noise), it is assumed that the averaging is provided by randomization of the noise sources when considering long time series (Shapiro and Campillo, 2004; Sabra et al., 2005b). Another important process contributing to the randomization is the scattering of seismic waves on heterogeneities within the Earth, that is significantly strong at periods less than 40 s. Reconstruction of Rayleigh waves from the seismic noise is sufficiently efficient and accurate to lead to high-resolution imaging at the regional scale (Shapiro et al., 2005; Sabra et al., 2005a). Further optimization of seismic imaging based on noise correlation requires better understanding of the origin of the seismic noise and of the spatial and temporal distribution of its sources (Pederson et al., 2007; Schulte-Pelkum et al., 2004). In particular, it is important to establish the conditions under which the noise can be considered as well randomized. To be more precise, a perfect randomization is not necessary but at least a distribution of sources covering a sufficiently large surface is required when integrating over time.

In the case of a spatially homogeneous distribution of noise sources, the cross correlation is expected to be nearly symmetric in amplitude and in arrival time with its positive and negative parts corresponding to the Green function of the medium and its anticausal counterpart, respectively (e.g., Lobkis and Weaver, 2001; Van Tiggelen, 2003; Snieder, 2004; Sánchez-Sesma and Campillo, 2006). In practice, as we will see below, the causal and anticausal parts of the cross correlation may strongly differ in

amplitude. This amplitude factor depends directly on the energy flux of the waves traveling from one station to the other (Van Tiggelen, 2003; Paul et al., 2005). In others words, in the case of a perfectly isotropic distribution of sources, the energy flux between two stations is the same in both directions and the resulting cross correlation between these stations is symmetric (Figure 5-1a). On the other hand, if the density of sources is larger on one side than on the other, the amounts of energy propagating in both directions are different. In this case, the resulting cross correlation is not symmetric anymore in amplitude (although the arrival time remains the same) (Figure 5-1b, c).

Snieder (2004) showed that only the sources near the line connecting two stations will contribute to the signals observed in the cross correlation function. Sources at opposite sides of the line will contribute to the signal at positive and negative lags in the cross correlation function respectively. An important consequence is that the asymmetry of the cross correlation computed between several pairs of stations of a network can be used to measure the main direction of the energy flux across the array. Making such measurements at different arrays will allow us to determine the location of main sources of the seismic noise.

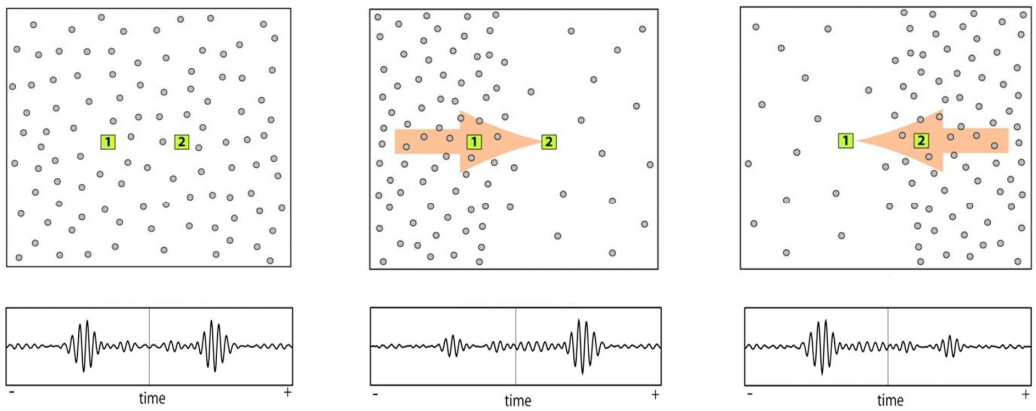

Figure 5-1. Schematic illustration of the effect of inhomogeneous noise sources distribution on the degree of symmetry of cross correlation. (a) Symmetric cross correlation between 1 and 2 obtained when the sources of noise are evenly distributed. (b), (c) Asymmetric cross correlation (but symmetric travel times) associated with a nonisotropic distribution of sources. Modified from Stehly et al. (2006).

5.2 The origin of seismic noise

Ambient seismic noise is mostly made of surface waves (e.g., Friedrich et al., 1998; Ekström, 2001). Therefore its sources are likely close to the Earth's surface. Observed noise amplitudes cannot be explained by the background seismicity (Tanimoto and Um, 1999) and main noise sources are believed to be loads caused by pressure perturbations in the atmosphere and the ocean. Moreover, the mechanisms of generation of seismic noise are not the same in different period bands. At relatively short periods (<20 s), the two strongest peaks of the seismic noise, i.e., the primary and the secondary microseisms, are believed to be related to the interaction of the sea waves with the coast (Gutenberg, 1951). The primary microseism has periods similar to the main swell (10–20 s), while the secondary microseism that is the strongest peak in the noise spectrum originates from the nonlinear interaction between direct and reflected swell waves that results in half period (5–10 s) pressure variations (Longuet-Higgins, 1950). This interaction results in variations of pressure at the sea bottom that do not exhibit the rapid exponential decay with depth expected for primary gravity waves.

Long-period seismic noise, referred to as earth ‘‘hum,’’ is observed in the continuous background free oscillations in low-frequency seismic spectra (Nawa et al., 1998). This term is usually reserved for motions with periods above 100 s. Early studies attributed the long-period noise to atmospheric motions (Tanimoto and Um, 1999; Ekström, 2001), but more recent studies (Tanimoto, 2005; Rhie and Romanowicz, 2004, 2006) suggest that the origin of the long-period noise is more likely related to so-called ocean infragravity waves, a long-period ocean gravity wave. Rhie and Romanowicz (2004) proposed that the generation of long-period seismic noise involves a three stage atmosphere-ocean-seafloor coupling process.

5.3 Seasonal variability and origin of seismic noise

In this chapter, we use the CCFs (Cross Correlation Function) to determine the characteristics of ambient seismic noise in NC. We kept only paths longer than 120 km (two wavelengths at 20 s) and SNR$\geqslant$6.0. This resulted in 7678 paths or 15356 azimuths when using both the causal and the acausal parts. Figure 5-2 shows three typical CCFs obtained from 14-month data. The CCF between VCHL and VFEN is symmetrical, the other two are asymmetrical.

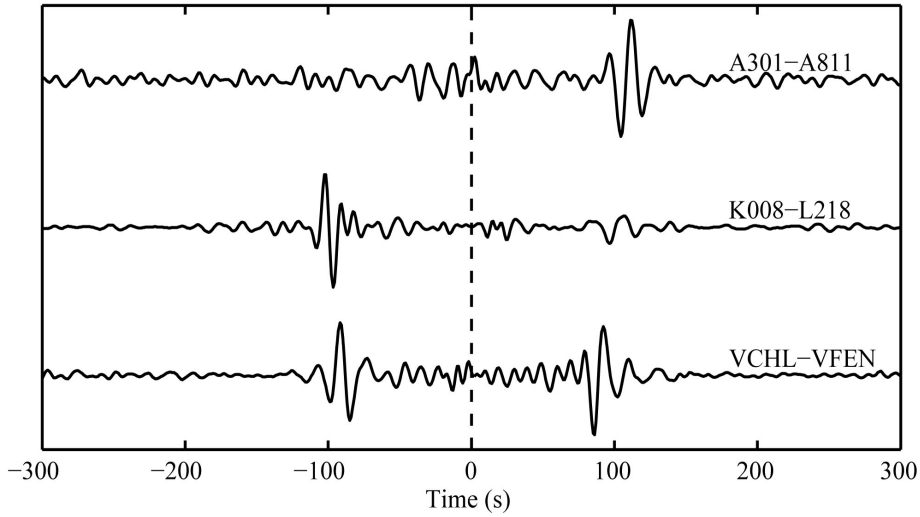

Figure 5-2. Three typical CCFs. The positive lags represent waves propagate from A301, K008, VCHL to A811, L218 and VFEN, respectively. The negative lags represent waves propagate in the opposite direction.

In this study, we apply three methods to analyze the characteristics of ambient seismic noise.

Method 1

First, we use two 3-month stacked CCFs to investigate the seasonal variability of the ambient noise source. The stacked CCFs are centered on February and August; namely, months 1, 2, 3 and 7, 8, 9. Following are data selection criteria:

Azimuth of the CCFs: 0 - 60 º (other azimuths also have similar traits),

SNR$\geqslant$6,

Interstation distances: 40-400 km,

We then stack the CCFs by 3 km bins in distance and normalize the amplitude using the maximum of each CCF. To illustrate the frequency-dependent characteristics of ambient noise sources, we filtered the CCFs with three subbands: 4-10 s (the secondary microseism), 10-20 s (the primary microseism) and 20-50 s (the low frequency noise). The results are shown in Figure 5-3.

Method 2

Secondly, we use the amplitudes of the CCFs to determine the direction of normalized background energy flow (NBEF) and compare its azimuthal distribution with global ocean wave height. The data selection criteria are same as the last step, but

using the CCFs from all azimuths. Amplitudes of the causal and acausal parts were determined by taking the maximum of their envelopes in a time window corresponding to the Rayleigh wave group velocity. We correct our measurement from the geometrical attenuation of the Rayleigh wave with distance, by multiplying the amplitude by the square root of the interstation distance. In this way we measured normalized amplitudes of seismic noise for two azimuths from each cross correlation. Combining measurements from all stations pairs we obtain the distribution of the normalized amplitude with respect to azimuth. Maxima of this distribution indicate main directions of NBEF across the array. Seasonal variation of the normalized amplitude and the direction of the NBEF during the year 2007 are illustrated in Figure 5-4. Amplitudes were normalized between 0 and 1 for the entire set of azimuths.

One must remark that these azimuthal distributions were computed after running-absolute-mean normalization. This means that high amplitude events, likely associated with the strongest storms are down weighted by our processing. Figure 5-4 is not directly characteristic of the actual absolute noise energy but of the time-averaged normalized energy. Note that it is the relevant measure for analyzing the noise in the context of Green function reconstruction using the procedure initiated by Shapiro and Campillo (2004).

Method 3

The third method is beamform analysis. To confirm, quantify, and interpret the seasonal amplitude variations of CCFs, we perform a beamforming analysis of the same data. The data processing method is similar with Lu et al. (2009) and Gerstoft et al., (2008). In this step, only interstation distances larger than 120 km are used.

For a given frequency ω, phase slowness s, and azimuth θ, the plane wave response for the array of geophones is

$$p(\omega, s, \theta, r) = \exp[i\omega s(r \cdot e)]$$

where $e = (\sin\theta, \cos\theta)^T$ are the directional cosines and r is the coordinates of the geophones with respect to their mean.

The beamforming output is then given by

$$b(\omega, s, \theta) = \sum_r p*(\omega, s, \theta; r) C(\omega) p(\omega, s, \theta; r)$$

Where $C(\omega)$ is the cross-spectral density matrix. $C(i, j; \omega)$ is obtained by the FFT transform of CCF between station *i*th and station *j*th. $C(i, j; \omega)$ contains the phase information between station *i*th and station *j*th at frequency ω. The angle resolution is 2 degrees, while the velocity resolution is 0.005 s/km.

Figure 5-5 and Figure 5-6 show the beamforming outputs of CCFs in summer (from April to September) and winter (from January to March and from October to December), respectively. The seasonal variations are observed from the beamforming output.

Following are the primary characteristics of seismic ambient noise in NC.

Near zero phase: A coherent energetic phase appears at near-zero times in noise cross correlations at 4-10 s period band (Figure 5-3a, b). This phase is stronger during northern winter than summer. The apparent velocity of this signal is larger than 12 km/s. Due to its fast propagating speed, we conjecture that this phase may be composed of P waves. Landes et al. (2009) use seismic arrays located in Yellowstone, in Turkey and in Kyrgyzstan and apply beamforming analysis and its projection on the Earth, they find that, in the 0.1-0.3 Hz frequency band, the energetic "near zero" time arrivals in seismic noise cross correlations are mainly formed by teleseismic P, PP, and PKP waves. Significant amount of the microseism energy is generated far from the coast in deep oceans.

4 – 10 s: The CCFs at this period band show apparent asymmetry and marked seasonal variation (Figure 5-3a, b). The ambient noise is stronger in winter. For this period band, the SNR of Green function is relatively low due to the short period surface wave attenuation and absorption of large propagating distances.

Using 1 year of recording at several stations of networks located in North America, Western Europe, and Tanzania and similar method, Stehly et al. (2006) found the noise between 5 and 10 s is very stable in time with signal mostly coming from the coastline. Using stations located in Europe, southern Africa, Asia, and three regions within North America, Yang and Ritzwoller (2008) analyzed the signal-to-noise ratios (SNR) of CCFs. They found that the ambient noise in 5-10 s band comes dominantly from the directions of relatively nearby coastlines with stronger noise occurring in the Northern Hemisphere in northern winter and in the Southern Hemisphere in southern winter.

In our case, we observe a marked seasonal variation of noise. This is similar to Yang and Ritzwoller (2008), but different to Stehly et al. (2006). This indicates that the noise sources and its characteristics are different in different regions. The location of the ambient noise is difficult to determine due to the low SNR.

10 – 20 s: The SNR of CCFs is much higher than 4–10 s. The seasonal variation of CCFs is also very clear. The CCFs are more symmetrical in winter than in summer (Figure 5-3c, d). Pie charts illustrate the azimuthal dependence of the normalized amplitude of the CCFs (or ambient noise energy flux), both for winter (left) and summer (right), see Figure 5-4a and b. The background image shows the distribution of the normalized global ocean wave height, modified after Stehly et al. (2006). The pie charts show that the ambient noise energy in the winter (Figure 5-4a) is more uniformly distributed than in the summer (Figure 5-4b). In the winter, noise energy is dominant in the north-east direction and also from the south (Indian Ocean) and the north-west (Northern Atlantic). In the summer, the main direction of the ambient noise energy is from the south-west, pointing to an origin in the Indian Ocean. The effect of attenuation is weaker for longer periods and sources at the global scale are contributing. These results clearly show that the 10–20 s noise is not generated locally but is excited by sources acting at the global scale and having a clear seasonal variability.

The hypothesis that the average background noise energy originates in the zones of storm activity is confirmed by strong similarities between the maps of the apparent sources of the 10–20 s seismic noise and the global wave height maps obtained from the radar altimeter data collected by the satellite TOPEX-Poseidon (Figure 5-4). Both maps show clear seasonal variations with maxima located in deep oceans in the Southern and the Northern hemispheres during the summer and the winter, respectively. These results are consistent with the observations of Stehly et al. (2006).

20 – 50 s: The SNR of CCFs is also higher than 4–10 s, but lower than 10–20 s. The patterns of energy arriving at this period are quite distinct from waves in the microseism band. These waves display little seasonal variability and the azimuthal patterns of energy arriving at this period band are very similar to one another. This observation is similar to Yang and Ritzwoller (2008). Rhie and Romanowicz (2006) also find that the microseism has a seasonal change in amplitude, whereas the amplitude in the hum band (with periods above 100 s) does not show clear seasonal

variations. Recent studies (Tanimoto, 2005; Rhie and Romanowicz, 2004, 2006) suggest that the origin of the long-period noise is more likely related to so-called ocean infragravity waves, a long-period ocean gravity wave.

In our view, the shallow water source location may be more plausible than the deep water sources distributed over a much larger area. If the noise is caused by deep water sources, the source regions would have to cover much of the ocean basins, which we argue is unlikely. However, deep water sources cannot be formally ruled out by the methods we apply here.

Beamforming results: Beamformer output provides valuable information about azimuthal distribution of noise. For periods between 10–32 s, there is a nearly continuous ring maximum with surface wave slownesses (Figure 5-5 and Figure 5-6), suggesting surface waves dominate the signal in this period range. Since the SNR of the CCFs for periods shorter than 10 s and larger than 30 s is relatively low, so we stress the noise characteristics for 10 – 30 s period band.

A seasonal variation of ambient seismic noise is clearly observed. Our results also show that even though the strongest noise emerges only from a few directions, strong ambient noise emerges from many directions. At 10 s and 16 s periods in winter, the wave field is dominated by energy coming from the east (30°–240°) in summer, and from the northeast, southwest and northwest in winter (Figure 5-5 and Figure 5-6). The beamforming outputs are in excellent agreement with results of the azimuthal distributions of CCFs' amplitudes (Figure 5-4). For periods larger than 20 s period, the noise sources are less seasonal variant. This is also consistent with the azimuthal distributions of CCFs' amplitudes.

For beamforming array aperture larger than λ is required to resolve the longest periods of interest and station spacing $< \lambda / 2$ to prevent spatial aliasing at shortest periods for a regularly spaced array, but for irregular arrays it can be relaxed somewhat (Harmon et al., 2008). For the NCSA array which consists mainly of two regularly-spaced line arrays pointing southeast, beamforming aliasing manifests itself as a straight-line beamformer output (perpendicular to the line array directions) rather than a point for sources coming from the southwest, as shown in the 9 s band in Figure 5-8. For shorter periods, the beamformer aliasing becomes more severe making it difficult to obtain reliable azimuthal distribution. Overall, the aliasing at the periods of

interest, 10–35 s, is minor while it dominates at periods less than 8 s.

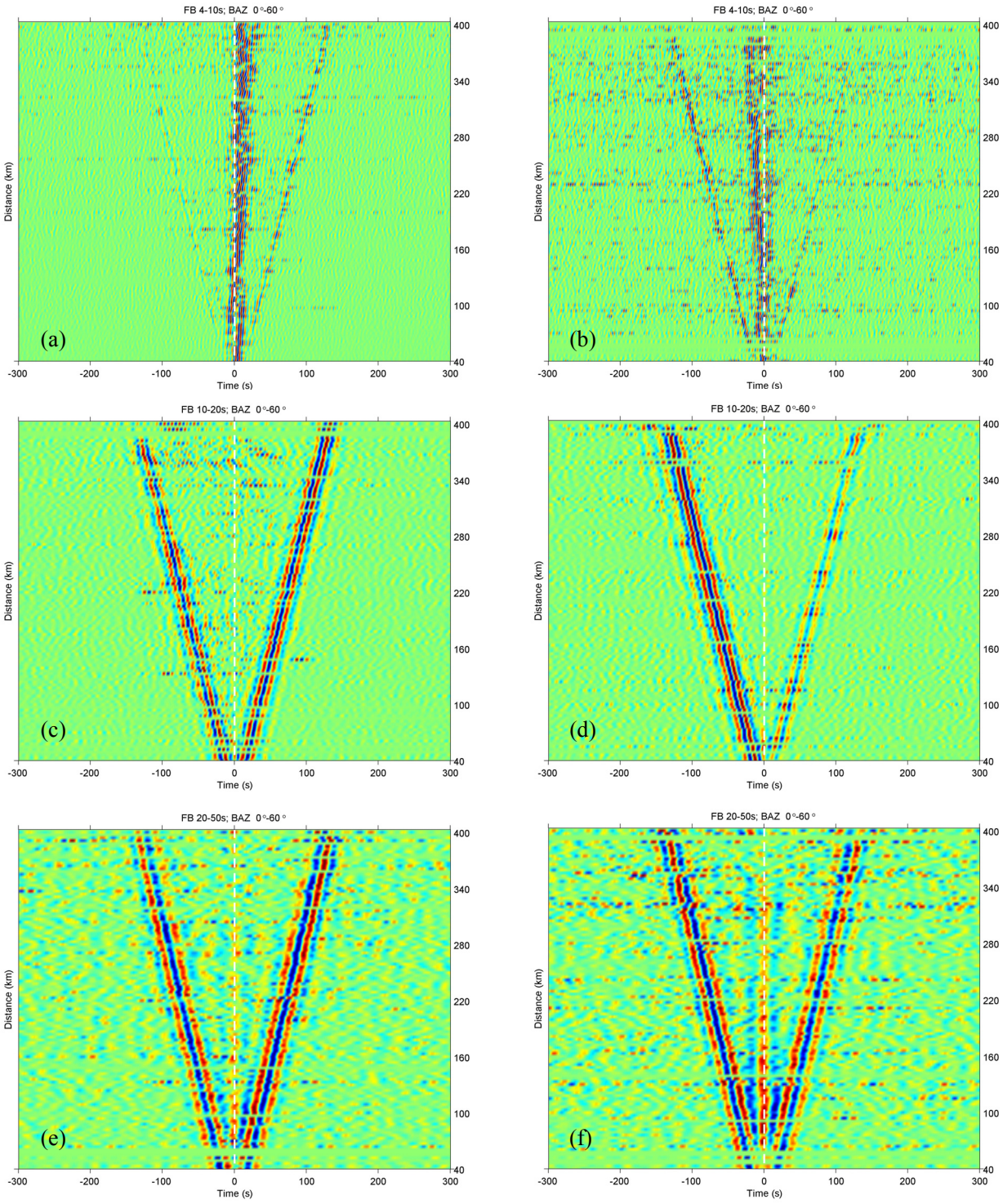

Figure 5-3. CCFs of different period bands and different seasons. (a) and (b) are bandpass filtered (4-10 s) CCFs for winter and summer. (c) and (d) are bandpass filtered (10-20 s) CCFs for winter and summer. (e) and (f) are bandpass filtered (20-50 s) CCFs for winter and summer. The azimuth of these CCFs are 0-60º. The interstation distances are 40-400 km.

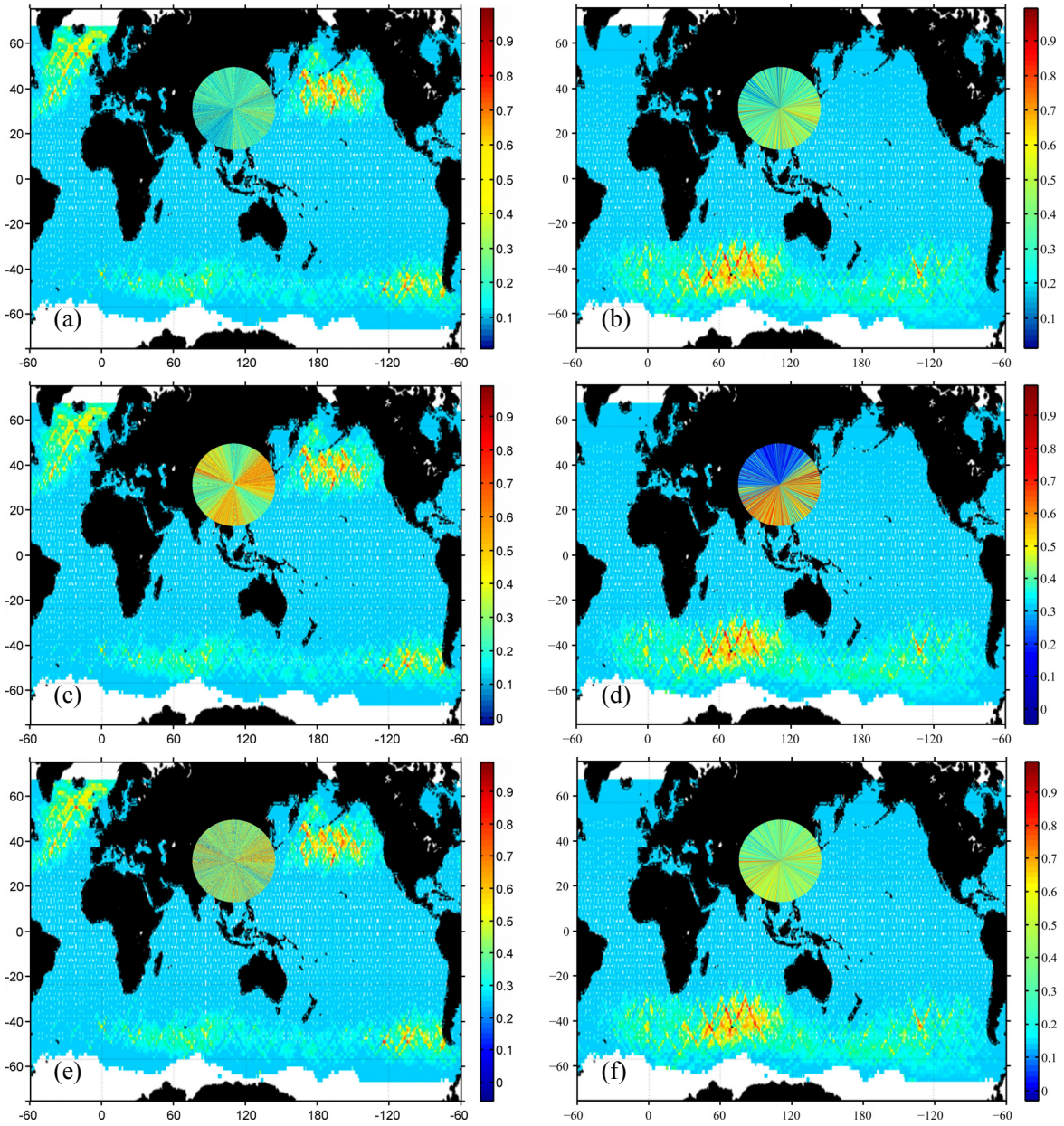

Figure 5-4. Normalized amplitude of the cross correlations versus azimuth for various period bands averaged during winter (left) and summer (right). (a) and (b) is 4-10 s, (c) and (d) is 10-20 s, (e) and (f) is 20-50 s. The background images are normalized global wave height maps measured by TOPEX/Poseidon during winter and summer.

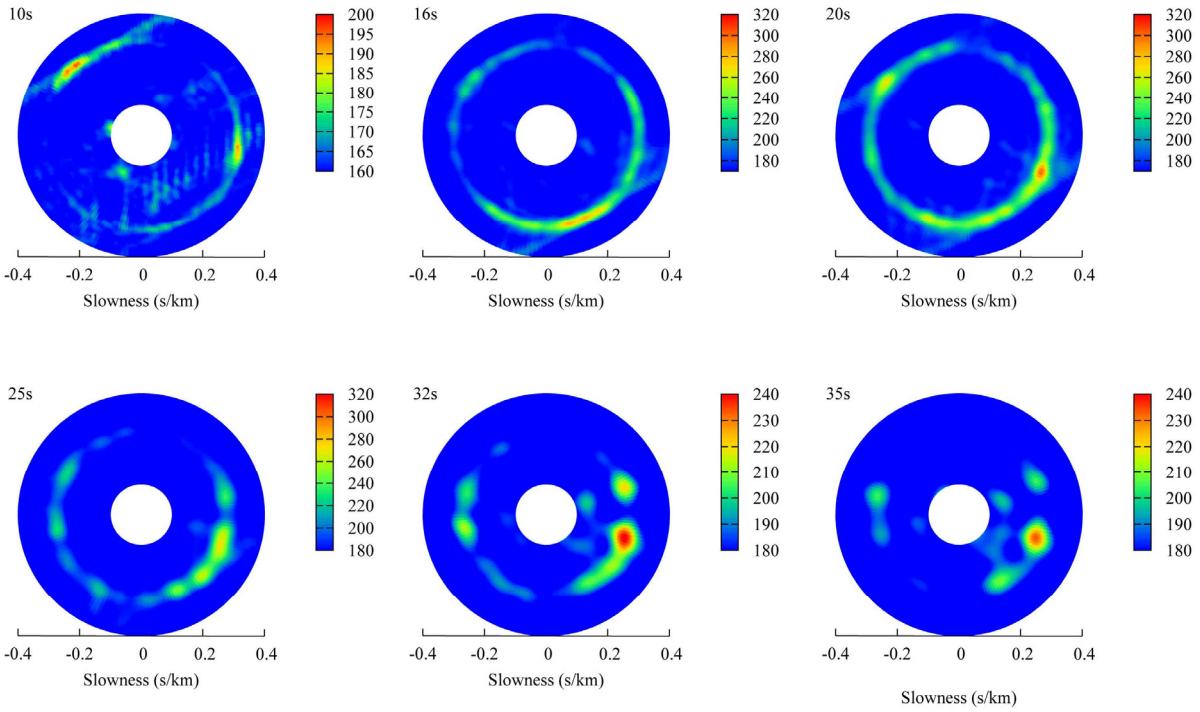

Figure 5-5. Azimuth distribution of the slowness spectra at different period in winter. After Lu et al. (2009).

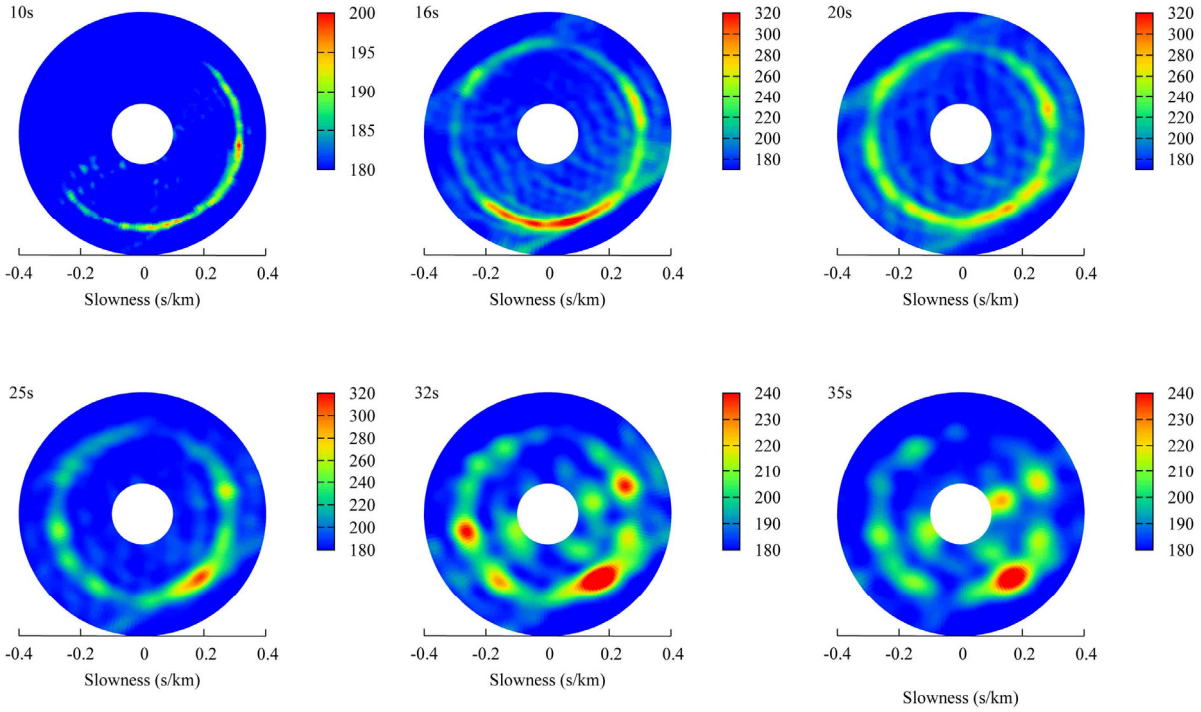

Figure 5-6. Azimuth distribution of the slowness spectra at different period in summer. After Lu et al. (2009).

5.4 The effect of inhomogeneous noise distribution

Recent theoretical work has revealed that, under the assumption that the sources of the ambient noise are evenly distributed, the Green's function between two points can be estimated from the cross-correlatation of recordings made at the two locations (Weaver and Lobkis 2001, 2004; Derode et al. 2003; Snieder 2004; Larose et al. 2005). The observed distribution of ambient noise is far from homogeneous, however, with exceptionally strong signals sometimes emanating only from a narrow range of azimuths (Paul et al., 2005; Stehly et al., 2006; Yang and Ritzwoller, 2008). Therefore questions have been raised about the effect that this will have on the emergence of accurate empirical Green's functions from cross correlations of ambient noise and whether the observations can be used meaningfully to obtain dispersion measurements and perform tomography. How to improve and optimize ANT?

This question has been addressed observationally in previous studies (e.g., Shapiro et al., 2005; Yang et al., 2007; Lin et al., 2008; Moschetti et al., 2007; Bensen et al., 2007, 2008) using several lines of evidence. These studies showed that the observed interstation empirical Green's functions are similar to earthquake signals when earthquakes occur near to one of the stations, that dispersion curves are seasonally repeatable even though ambient noise characteristics may change substantially, and that the dispersion curves are consistent with one another even when azimuths are quite different. In addition, they showed that the resulting group and phase velocity maps reproduce geological structures faithfully. These and other reasons help to establish the veracity of ambient noise tomography. It should be borne in mind, however, that considerable efforts are exerted in processing ambient noise data to identify bad measurements (commonly more than half of all observations), some of which result from low signal levels or incomplete constructive/destruction interference in the generation of the observed Green's functions.

Sabra et al. (2005b) argues that scattering from heterogeneities and geometric effects (such as reflections from the edge of a basin) randomizes the noise field and thus partially redistributes the ocean microseism wave field making it more uniform. The synthetic experiments show that if ambient noise exists over a broad azimuthal range even at relatively low levels, accurate empirical Green's functions will emerge from long time series of the ambient noise even when the distribution is far from azimuthally

homogenous (Yang and Ritzwoller, 2008). The numerical experiment shows that stronger scattering can improve the reconstruction of the Green function even for an inhomogeneous distribution of sources (Paul et al., 2005). This effect was already confirmed by laboratory experiments (Derode et al., 2003). The experiments of Lin et al. (2008) show that the measured phase velocities of the CCFs match the input phase velocity at all periods with errors less than 0.5%. The uncertainty of group velocity dispersion measurement is higher, but still less than 2%. Harmon et al. (2008) measured the phase velocity dispersion curves from NCFs and teleseismic surface waves, and found the discrepancy is within 1%. These experiments and observations confirm that ambient noise can be used to perform tomography and ANT is valid.

For the orientation of most station pairs, sufficiently strong ambient noise is present to be the basis for the retrieval of reliable empirical Green's functions. Nevertheless, there are some azimuths in most regions where ambient noise is so weak that interstation cross correlations will not provide a good empirical Green's function. From a practical perspective, therefore, these cross correlations have to be identified and removed as candidate empirical Green's functions. Typically, these cross correlations have a low signal-to-noise ratio, and SNR is useful in the data processing part of ambient noise tomography to identify the acceptable empirical Green's functions (e.g., Bensen et al., 2007).

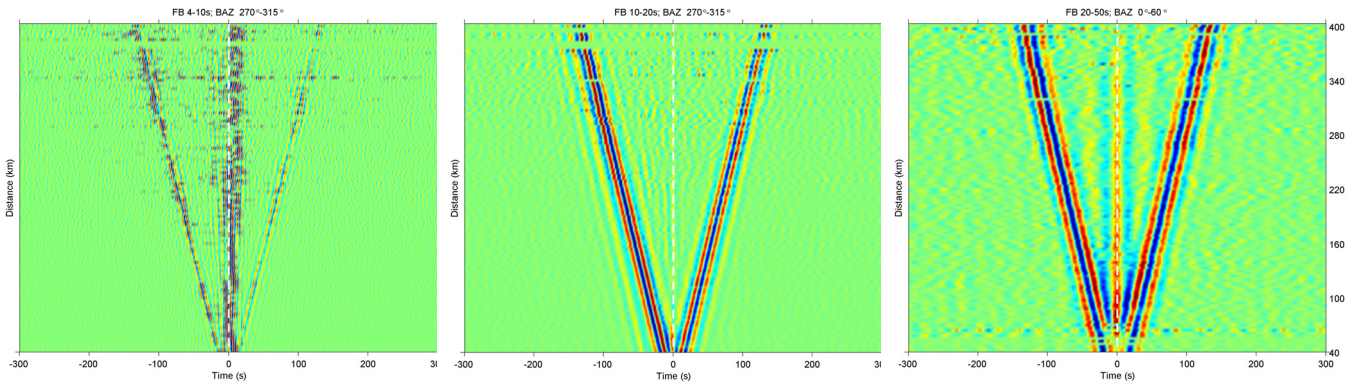

(a) (b) (c)

Figure 5-7. CCFs of different period bands for 14-month. (a), (b) and (c) are bandpass filtered between 4-10 s, 10-20 s and 20-50 s, respectively. It can be seen the SNR of the CCFs obtained using 14 month data is higher than only using summer or winter data.

Figure 5-7 show the extracted CCFs using 14 months data. It can be seen the SNR and symmetry of the signal are enhanced greatly by using long period data. The beamform outputs (Figure 5-8) using 14 month data also show that the noise

distribution is more uniform than only using summer or winter data. These results indicate that the longer the observation time, the more homogeneous of seismic noise, and higher SNR. So, in order to get more reliable tomography results, we propose to use data longer than 1 year.

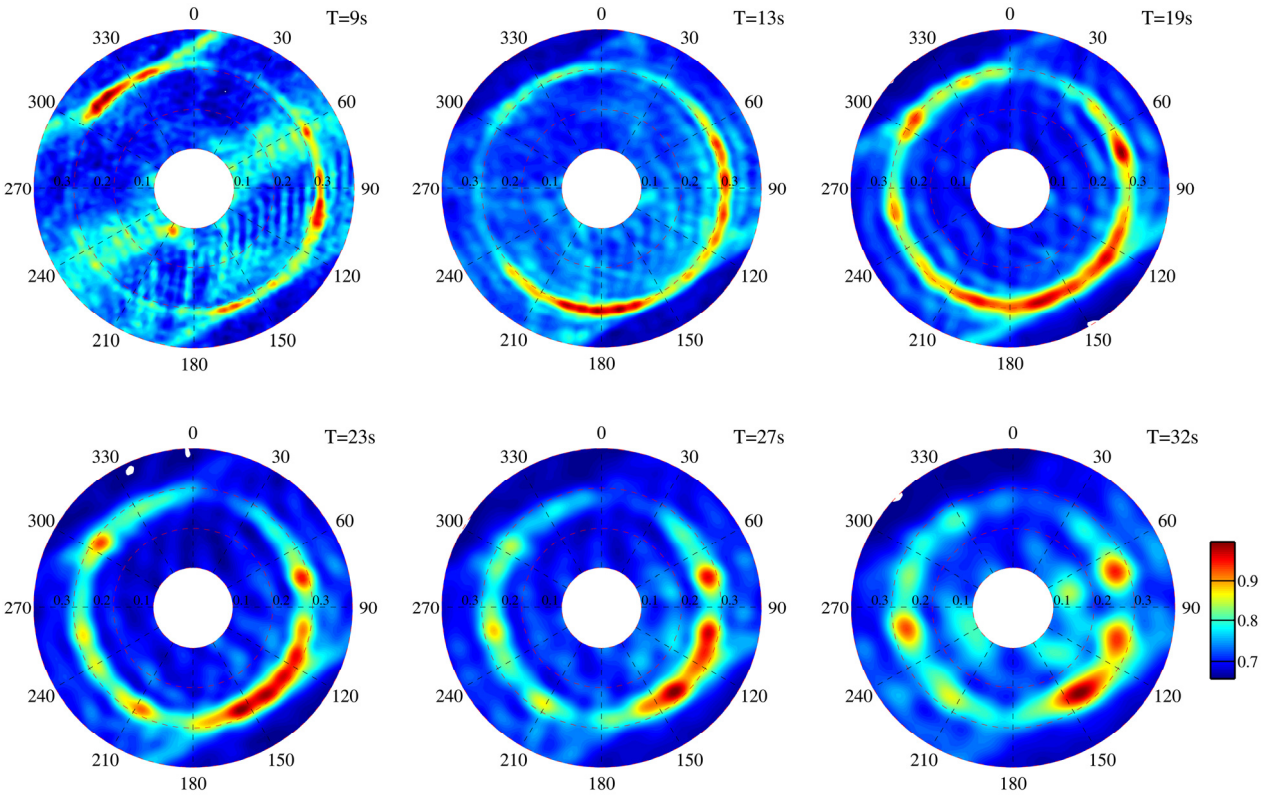

Figure 5-8. The slowness spectra of Rayleigh wave at different periods obtained by beamforming using all station records during 2007.

5.5 Conclusions

Our results clearly demonstrate that the characteristics of ambient seismic noise are different in different period bands. A marked seasonal variation of noise is also observed for periods less than 20 s. The seasonal variability of primary microseism exhibits good correlation with the maps of average ocean wave height map obtained by TOPEX-Poseidon.

This seasonal variation means that the quality of the Green function reconstruction by cross correlation can be different with noise recorded during the summer and during the winter. Using simultaneously data recorded during the winter and the summer would be a way to increase the number of high-quality measurements and to improve the resolution of seismic imaging based on noise cross correlation.

Chapter 6 Conclusions and Future Work

6.1 Conclusions

We studied the theory and methodology of ambient noise tomography and we applied this method to NC successfully. Continuous vertical-component seismograms, spanning the period from January 1, 2007 to February 28, 2008 recorded by 190 broadband stations and 10 very broadband stations, are used in this study. We apply the cross correlation technique to the ambient noise data for each station pairs recorded by NCSA. Rayleigh wave group velocity dispersion curves are measured at periods between 4s and 40s by multiple filter technique. We obtain 5630 high quality dispersion curves. Surface wave tomography is conducted to generate group velocity maps with a grid spacing of 0.25º×0.25º. These maps display higher resolution and span to shorter periods than previous surface wave tomography maps. Then genetic algorithm was used to invert local dispersion curves. The 3-D shear wave velocity structure from 0 to 50 km depth was readily constructed. To the authors' knowledge, the resolution presented here is, so far, the highest one in China mainland.

The important findings are:

1, We can obtain more reliable dispersion measurement by introducing maximum cutoff period. The maximum period extracted from ambient seismic noise is related to the aperture of the seismic array. The larger the aperture, the wider the spectrum band is. The SNR of Green Function is proportional to the square root of observation time and can be enhanced by using symmetric component. The inhomogeneous distribution of seismic noise gives rise to the asymmetry of Green Function. Using more than 1 year's data, we can get more symmetric and higher SNR Green Function.

2, We analyzed the characteristic of ambient seismic noise and found the characteristics are different for different period band. Between 4-10s period band, there is a coherent phase with large amplitude near zero lag time. In 10-20s period band, the sources of ambient seismic noise has a very clear seasonal variability. The azimuthal distributions of noise share a great similarity with the map of average ocean wave height map obtained by TOPEX-Poseidon. In 20-50s period band, Rayleigh wave Green Functions are near symmetrical and have less seasonal variation in both signal strength and directivity, which indicate the distribution of noise is almost homogeneous.

In 4-20s period band, the amplitudes of positive and negative components of Green Functions are obviously asymmetrical, but the arrival times are near identical, which indicate the distribution of noise has much influence on the amplitude of Green Function, but less influence on arrival time. The beamform analysis shows that using simultaneously data recorded during the winter and the summer would be a way to increase the number of high-quality measurements and to improve the resolution of seismic imaging based on noise cross correlation.

3, Tomographic maps, with a grid spacing of 0.25º×0.25º, are computed between 4s and 40s period band. The maps at short periods reveal an evident lateral heterogeneity in the curst of North-China, quite well in agreement with known geological and tectonic features. The North China Basin is imaged as a broad low velocity area, while the Taihangshan and Yanshan uplifts and Ordos block are imaged as high velocity zones, and the Quaternary intermountain basins show up as small low-velocity anomalies.

4, We constructed the 3-D shear wave crustal velocity model in North China by inverting the pure path Rayleigh wave dispersion curves at 432 nodes using genetic algorithm. The inversion results reveals the shear wave velocity structure in North China crust, the thickness of sedimentary cover and the lateral variation of Moho interface very well. Our results show that the thickness of sedimentary cover is less than 2 km in Taihangshan and Yanshan uplifts, about 5 km in Yanqing-Huailai basin and about 3 km in Datong basin. The thickness of sedimentary cover in North China basin is more than 6 km and has lateral variation in different tectonic units. The thickness of sedimentary cover is about 8 km in Cangxian uplift and about 11 km in Jizhong and Huanghua depressions. The depth of Moho interface is thicker in westert part than those in the eastern part. The crustal thickness increases from 28 km in Bohai Bay to 44 km in Zhangjiakou.

5, S-wave velocity maps at different depths show that Taihangshan fault is a boundary of high and low velocity anomaly in 0-12 km depth. Below 13 km, the boundary of high and low velocity anomaly is visible only at some parts of Taihangshan fault. We infer that Taihangshan fault only extends to Moho interface in some regions. From 0 to 8 km, Yanshan uplift is mapped as broad high velocity anomaly, while its southern margin is mapped as high and low velocity anomalies alternatively, which

may be caused by the NNE-NE trend faults. There is a distinct low velocity belt with NW trend at 10 km depth near Zhangjiakou-Bohai seismic zone. This low velocity belt and the southern margin of Yanshan high velocity anomaly draw the outline of Zhangjiakou-Bohai seismic zone and its northern boarder line. There is a well-defined low velocity zone in middle to lower crust (15-25 km) in the Beijing-Tianjin-Tangshan region, which may be caused by intrusion of hot mantle materials.

6, We analyzed the S-wave velocity structure near Tangshan，Luanxian and Ninghe earthquake region. We find the focal depth of Ninghe earthquake is located in the transition zones of high and low velocity bodies. The focal depths of Tangshan and Luanxian earthquake are located in high velocity bodies. There is a low velocity zone beneath the focuses of Tangshan and Luanxian earthquake. Moho interface is locally uplifted in Ninghe and Luanxian. The S-wave velocity is lower in the uppermost mantle of these three earthquake regions. We infer that these three earthquakes are mainly caused by vertical deformation of upper mantle and material exchange between crust and upper mantle. The magma intrudes crust along faults near the boundary of crust and upper mantle, which leads to the low velocity anomaly in the uppermost mantle. The magma intrusion heats up the lower crustal material and drops the viscosity. Some minerals are dehydrated. The water move up and store in the middle crust. The existence of liquid affects the structure and composition of fault zone, further changes the stress state, weakens the seismotectonic region and triggers the earthquakes.

6.2 Future work

The presented group velocity tomography from the ambient noise cross correlations was conducted only with the vertical components. In practice, using the three components at the stations, the nine components of Green's tensor can be recovered between the two stations. A synthetic study, which was conducted about recovery of multiple component Green's tensor for coda waves, was performed by Paul et al. (2005). In our study, the cross correlations of radial-radial (R-R) and transverse-transverse (T-T) components were also conducted. Figure 6-1 shows the extracted Love wave signal and Love wave tomography map. The differences in the shear-wave velocity models obtained from Love waves and Rayleigh waves can be used to study anisotropy and heterogeneity of the crust.

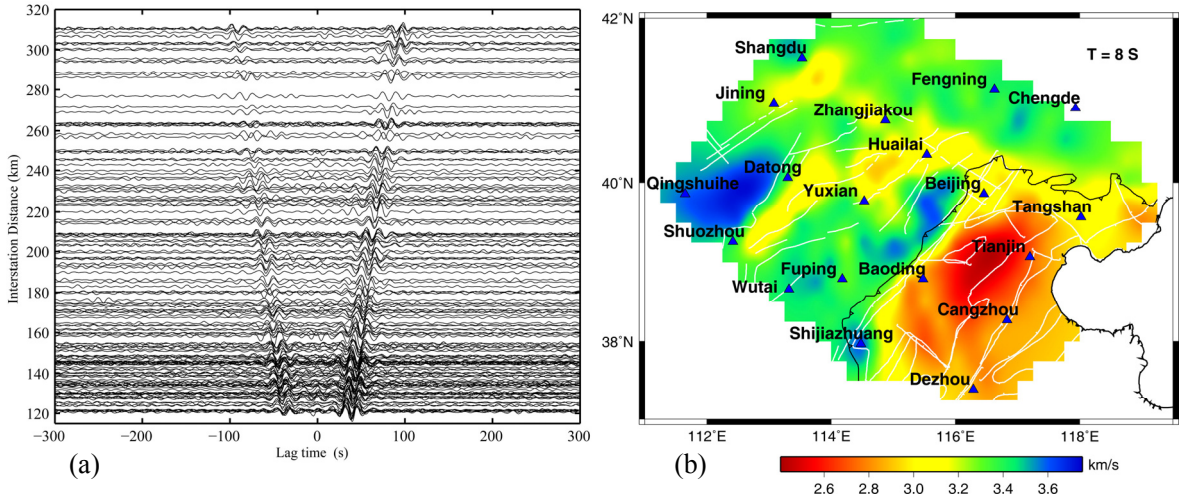

Figure 6-1. (a) Bandpass filtered (10-50s) transverse-transverse cross correlations as a function of distance and lag time. The cross correlation is time reversed if the amplitude of the negative component is smaller than the amplitude of the positive one. (b) Love wave tomographic map for 8 s period.

For traditional surface wave tomography, it is difficult to obtain short period dispersion measurements due to the absorption, attenuation and scattering of seismic waves. Ambient noise tomography overcomes this drawback and it can get reliable short period dispersion curves (e. g. T<30 s). We can constrain the crust-mantle velocity structure tightly by combining ambient seismic noise and earthquake excited surface waves. Furthermore, surface wave dispersions are sensitive to the average shear-velocity structure, receiver functions are sensitive to velocity contrasts between layers. Thus, a joint inversion of dispersion curves and receiver functions will results in a better-determined shear-wave structure than inversion from either method alone. This is a focus of my future study.

References

Aki, K., 1957. Space and time spectra of stationary stochastic waves with special reference to microtremors, Bull. Earthquake Res. Inst. Univ. Tokyo, 35, 415-456.

Backus, G. E. & Gilbert, F., 1968. The resolving power of gross Earth data, Geophys. J., 16, 169-205.

Bai, J. & Dai, F. Y., 1996. The early Precambrian crustal evolution of China. Journal of Southeast Asian Earth Sciences, 13, 205-214.

Bai, J. & Dai, F. Y., 1998. Archaean crust of China. In: Ma, X. Y. & Bai, J. (eds) Precambrian Crustal Evolution of China. Geological Publishing House, Beijing, 15-86.

Bensen, G. D., M. H. Ritzwoller, M. P. Barmin, A. L. Levshin, F. Lin, M. P. Moschetti, N. M. Shapiro, and Y. Yang., 2007. Processing seismic ambient noise data to obtain reliable broad-band surface wave dispersion measurements, Geophys. J. Int., 169, 1239-1260, doi:10.1111/j.1365- 246X.2007.03374.x.

Bensen, G. D., M. H. Ritzwoller, and N. M. Shapiro. 2008. Broadband ambient noise surface wave tomography across the United States, J. Geophys. Res., 113, B05306, doi:10.1029/2007JB005248.

Camp, C. V., S. Pezeshk, and G. Cao., 1998. Optimized design of two dimensional structures using a genetic algorithm, Journal of Structural Engineering. 124, 5, 551-559.

Campillo, M., and A. Paul., 2003. Long-range correlations in the diffuse seismic coda, Science, 299, 547-549.

Campillo, M., 2006. Phase and correlation in random seismic fields and the reconstruction of the Green function, Pure Appl. Geophys., 163, 475-502.

Chang, C., 1991. Geological characteristics and distribution patterns of hydrocarbon deposits in the Bohai Bay Basin, east China. Mar. Pet. Geol. 8, 98-106.

Chen, L., T. Zheng, and W. Xu, 2006. A Thinned Lithospheric Image of the Tanlu Fault Zone, Eastern China: Constructed from Wave Equation Based Receiver Function Migration, J. Geophys. Res., 111, B09312, doi:10.1029/2005JB003974.

Chen, L., T. Zheng, and W. Xu, 2006. Receiver function migration image of the deep structure in the Bohai Bay Basin, eastern China, Geophys. Res. Lett., 33, L20307, doi:10.1029/2006GL 027593.

Chen, L., Wang, T., Zhao, L. and Zheng, T., 2008. Distinct Lateral Variation of Lithospheric thickness in the Northeastern North China Craton, Earth Planet. Sci. Lett., 267, 56-68.

Chen Y. and Li L., 2003. Several Development Trends of Seismological Science.

Recent Developments in World Seismology. 289, 1, 1-6.

Cheng Y. Q., 1994. Outlines of Regional Geology of China (in Chinese), Beijing: Geological Publishing House, 90-164.

China Earthquake Administration, 1986. Geophysical exploration results of crust and upper mantle in China. Beijing: Seismological Press.

China Earthquake Networks Center, Seismic Data Management and Service System, 2008. http://www.csndmc.ac.cn/newweb/index.jsp.

Cho, K. H., Herrmann, R. B., Ammon, C. J., and Lee, K., 2007. Imaging the upper crust of the Korean Peninsula by surface-wave tomography, Bull. Seismol. Soc. Am., 97, 198-207.

Claerbout J F. 1968. Synthesis of a layered medium from its acoustic transmission response. Geophysics, 33, 264-269.

Curtis, A., Trampert, J., Snieder, R., 1998. Eurasian fundamental mode surface wave phase velocities and their relationship with tectonic structures. J. Geophys. Res. 103, 26919-26947.

Dal Moro, Giancarlo, Pipan, Michele, Gabrielli, Paolo. 2007. Rayleigh wave dispersion curve inversion via genetic algorithms and Marginal Posterior Probability Density estimation. Journal of Applied Geophysics, Volume 61, Issue 1, p. 39-55.

Davis G. A., C. Wang and Y. Zheng et al., 1998. The enigmatic Yinshan fold-and-thrust belt of northern China: new views on its intraplate contractional styles, Geology, 26, 43-46.

Deng J. F., Wu Z. X., Zhao G. C., et al., 1999. Precambrian granitic rocks, continental crustal evolution and craton formation of the North China Platform, Acta Petrologica Sinica (in Chinese), 15(2), 190-198.

Deng J. F., Zhao H. L., Mo X. X. et al., 1996. Continental Root-Plume Tectonics of China—Key to the Continental Dynamics (in Chinese with English abstract), Beijing: Geological Publishing House, 1-96.

Deng, Q.D., et al. 2004. Distribution of active faults in China (1:4000000). Beijing: Science Press.

Derode, A., E. Larose, M. Campillo, and M. Fink., 2003a. How to estimate the Green's function of a heterogeneous medium between two passive sensors? Application to acoustic waves, Appl. Phys. Lett., 83, 3054-3056.

Derode, A., E. Larose, M. Tanter, J. de Rosny, A. Tourim, M. Campillo, and M. Fink., 2003b. Recovering the Green's function from field-field correlations in an open scattering medium, J. Acoust. Soc. Am., 113, 2973-2976.

Ding, Z. F. & Zeng, R. S., 1994. The 3D velocity structure inversion in Beijing-Tianjin-Tangshan area by using local earthquake data. North China

Earthquake Sciences, 12(2), 14-20.

Ding Z. F., Zhou X. F., Wu Y. et al., 2009. Tomographic imaging of P wave velocity structure beneath the region around Beijing. Earthq Sci. 22, 403-408.

Ditmar, P. G., Yanovskaya, T. B., 1987. Generalization of Backus–Gilbert method for estimation of lateral variations of surface wave velocities. Phys. Solid Earth, Izvestia Acad. Sci. U.S.S.R. 23(6), 470-477.

Duvall, T., S. Jefferies, J. Harvey, et al., 1993. Time distance helioseismology, Nature, 362, 430-432.

Dziewonski A, Bloch S and Landisman M., 1969. A technique for t he analysis of transient seismic signals. Bull. Seism. Soc. Am., 59, 427-444.

Editorial Group of "The 1976 Tangshan Earthquake", State Seismological Bureau. 1982. The 1976 Tangshan Earthquake. Beijing: Seismological Press, 71-79.

Ekström, G., 2001. Time domain analysis of Earth's long-period background seismic radiation, J. Geophys. Res., 106, 26, 483-26, 494.

Fan, W. M., Chen, X. and Menzies Martin, A., 1993. Geographical variations of major elements for peridotitic xenoliths in relation to crust/lithosphere age and thickness in eastern China. Geotectonica et Metallogenia, 17(3), 221-228.

Feng, C. C., and T. L. Teng, 1983. Three-Dimensional Crust and Upper Mantle Structure of the Eurasian Continent, J. Geophys. Res., 88(B3), 2261-2272.

Friedrich, A., F. Krüger, and K. Klinge, 1998. Ocean generated microseismic noise located with the Gra¨fenberg array, J. Seismol., 2, 47-64.

Forsyth, D.W. and A. Li, 2005. Array-analysis of two-dimensional variations in surface wave phase velocity and azimuthal anisotropy in the presence of multi-pathing interference, in Seismic Earth: Array Analysis of Broadband Seismograms (A. Levander and G. Nolet, ed.), AGU Geophysical Monograph Series, 157, 81-97.

Fowler, C. M. R., 1995. The Solid Earth. An Introduction to Global Geophysics. Cambridge Univ. Press.

Gao, W. X. & Ma, J., 1993. Seismo-geological background and earthquake hazard in Beijing area. Beijing: Seismological Press, pp, 54.

Gerstoft, P., P. M. Shearer, N. Harmon, and J. Zhang, 2008. Global P, PP, and PKP wave microseisms observed from distant storms, Geophys. Res. Lett., 35, L23307, doi:10.1029/2008GL036111.

Gilles P. M., Duvall T. L., Scherrer P. H. and Bogart R. S., 1997. A subsurface flow of material from the Sun equator's to its poles. Nature, 390, 52-54.

Gutenberg, B., 1951. Observation and theory of microseisms, in Compendium of Meteorology, edited by T. F. Malone, pp. 1303-1311, Am. Meteorol. Soc., Providence, R. I.

Godin O. A., 2007. Emergence of the acoustic Green's function from thermal noise. The Journal of the Acoustical Society of America, 121, EL96–EL102.

Goldberg, D. E., 1989. Genetic Algorithms in Search, Optimization, and Machine Learning, Addison-Wesley, Reading, Massachusetts.

Gouédard, P., L. Stehly, F. Brenguier, et al., 2008. Cross correlation of random fields:mathematical approach and applications, Geophysical Prospecting, 56, 375-393, doi:10.1111/j.1365-2478.2007.00684.

Griffin, W. L., Zhang, A., O'Reilly, S. Y. and Ryan, C. G., 1998. Phanerozoic evolution of the lithosphere beneath the Sino-Korean Craton. In: M.F.J. Flower, S.-L. Chung, C.-H. Lo and T.-Y. Lee (Editors), Mantle dynamics and plate interactions in East Asia. Geodynamics Series, pp. 107-126.

Guo J. H., Zhai M. G., Xu R. H., 2001. Timing of the granulite facies metamorphism in the Sanggan area, North China craton: zircon U-Pb geochronology, Science in China, Ser. D, 44(11), 1010-1018.

Harmon N, Gerstoft P, Rychert C A, et al., 2008 Phase velocities from seismic noise using beamforming and cross correlation in Costa Rica and Nicaragua. Geophys. Res. Lett., 35, L19303, doi:10.1029/2008GL035387.

He Z. Q., Ding Z. F., Ye T. L., et al., 2001, Surface wave tomography of the crust and upper mantle of Chinese mainland, Acta seismological sinica, 23, 6, 596-603.

He Z. Q., Ding Z. F., Jia H., et al., 2007, To determine the velocity structure of shallow crust with surface wave information in microtremors, Chinese Journal of Geophysics, 50, 2: 492-498.

He Z. Q., Ye T. L., and Ding Z. F., 2009. Surface wave tomography for the phase velocity in the northeastern part of North China, Chinese Journal of Geophysics, 52(5), 1233-1242.

Hirth, G., Evans, R. L., and Chave, A. D., 2000. Comparison of continental and oceanic mantle electrical conductivity: Is the Archean lithosphere dry?: Geochemistry, Geophysics, Geosystems, v. 1, doi:10.1029/2000GC000048.

Holland, J. H. 1975. Adaptation in Natural and Artificial Systems, University of Michigan press, Ann Arbor.

Hong D. W., Wang T., Tong Y., et al., 2003. Mesozoic granitoids from North China block and Qinling-Dabie-Sulu orogenic belt and their deep dynamic process, Earth Science Frontiers (in Chinese with English abstract), 10(3): 231-256.

Huang, J. & Zhao, D., 2004. Crustal heterogeneity and seismotectonics of the region around Beijing, China, Tectonophysics, 385, 159-180.

Huang, Z., W. Su, Y. Peng, Y. Zheng, and H. Li, 2003. Rayleigh wave tomography of China and adjacent regions, J. Geophys. Res., 108(B2), 2073, doi:10.1029/2001JB00 1696.

Jia S. X., Zhang X. K., 2005. Crustal structure and comparison of different tectonic blocks in North China. Chinese J. Geophys. (in Chinese), 48(3), 611-620.

Jordan, T.H., 1975, The continental tectosphere: Reviews of Geophysics and Space Physics, v. 13, p. 1-12.

Keilis-Borok,V. I., and T. B.Yanovskaya, 1967. Inverse problems of seismology (structural review). Geophys. J. R. Astr. Soc., 13, 223-234.

Kröner, A., Wilde, S., Wang, K. & Zhao, G. C., 2002. Age and evolution of a late Archaean to early Proterozoic upper to lower crustal section in the Wutaishan/Hengshan/Fuping terrain of northern China, a Field Guide. GSA Penrose Conference, Beijing.

Kusky, T. M., Li, J. H. & Tucker, R. T., 2001. The Archaean Dongwanzi ophiolite complex, North China Craton: 2.505 billion year old oceanic crust and mantle. Science, 292, 1142-1145.

Kusky, T. M. & Li, J. H., 2003. Paleoproterozoic tectonic evolution of the North China Craton. Journal of Asian Earth Sciences, 22, 383-397.

Kusky, T. M., Li, Z. H., Glass, A. & Huang, H. A., 2004. Archaean ophiolites and ophiolite fragments of the North China craton. In: KUSKY, T. M. (ed.) Precambrian Ophiolites and Related Rocks. Developments in Precambrian Geology, 13, 223-274.

Kusky T. M., B. F. Windley & M. G. Zhai, 2007. Tectonic evolution of the North China Block: from orogen to craton to orogen, Geological Society, London, Special Publications; v. 280; p. 1-34; DOI:10.1144/SP280.1

Landes M., Hubans F., Shapiro N. M., et al., 2009. Origin of deep ocean microseims by using teleseismic body waves. Journal of geophysical Research, doi:10.1029/ 2009JB006918, in press.

Larose E., Derode A., Campillo M. and Fink M. 2004. Imaging from one-bit correlation of wide-band diffuse wavefield. Journal of Applied Physics, 95, 8393-8399.

Larose, E., A. Derode, D. Corennec, L. Margerin, and M. Campillo, 2005a. Passive retrieval of Rayleigh waves in disordered elastic media, Phys. Rev. E, 72, 046607, doi:10.113/PhysRevE.72.046607.

Larose E., Khan A., Nakamura Y. and Campillo M. 2005b. Lunar subsurface investigated from correlation of seismic noise. Geophysical Research Letters, 32, L16201.

Larose E., Margerin L., Derode A., Tiggelen B.V., Campillo M., Shapiro N.M., Paul A., Stehly L. and Tanter M. 2006. Correlation of random wavefields: an interdisciplinary review. Geophysics, 71, 4, SI11-SI21.

Levshin, A., L. Ratnikova, and J. Berger, 1992. Peculiarities of surface wave

propagation across central Eurasia. Bull. Seism. Soc. Am., 82(6), 2464-2493.

Li, J. H., Qian, X. L. & Gu, Y. C. 1998. Outline of Paleoproterozoic tectonic division and plate tectonic evolution of North China Craton. Earth Science, 23, 230-235.

Li, J. H., Qian, X. L., Huang, X. N. & Liu, S. W. 2000a. The tectonic framework of the basement of North China Craton and its implication for the early Precambrian cratonization. Acta Petrologica Sinica, 16, 1-10.

Li, J. H., Kröner, A., Qian, X. L. & O'brien, P. 2000b. The tectonic evolution of early Precambrian high-pressure granulite belt, North China Craton (NCC). Acta Geological Sinica, 274, 246-256.

Liang, C., and C. A. Langston, 2008. Ambient seismic noise tomography and structure of eastern North America, J. Geophys. Res., 113, B03309, doi:10.1029/2007JB00 5350.

Lin, F., M. H. Ritzwoller, J. Townend, M. Savage, and S. Bannister, 2007. Ambient noise Rayleigh wave tomography of New Zealand, Geophys. J. Int., 170, 649-666, doi:10.1111/j.1365-246X.2007.03414.x.

Lin, F., M. P. Moschetti, and M. H. Ritzwoller, 2008. Surface wave tomography of the western United States from ambient seismic noise: Rayleigh and Love wave phase velocity maps, Geophys. J. Int., 173, 2, 281-298.

Liu F. T., Qu K. X.,Wu H.,et al. 1986. Seismic tomography of North China region. Chinese J .Geophys. (in Chinese), 29(5), 442-449.

Liu, G., Sun, J. & Liu, J., 1989. The electrical structure of the crust and upper mantle in North China. In: Ma, X. (Ed.), Lithospheric Dynamics Atlas of China. Beijing: China Cartographic Press, pp. 59-62.

Liu J. M., Zhang H. F., Sun J. G. et al., 2004. Geochemical research on C-O and Sr-Nd isotopes of mantle-derived rocks from Shandong Province, China, Science in China, Ser. D, 47(2), 171-180.

Liu J. Q. 1987. Geochronology of the Cenozoic volcanic rocks in Northeast China. Acta Petrol. Sinica (in Chinese). (4), 21-31.

Lobkis, O., and R. Weaver. 2001. On the emergence of the Green's function in the correlations of a diffuse field, J. Acoust. Soc. Am., 110, 3011-3017.

Lomax, A., R. Snieder. 1994. Finding sets of acceptable solutions with a genetic algorithm with application to surface wave group dispersion in Europe, Geophys. Res. Lett., 21, 2617-2620.

Lomax, A., and R. Snieder, 1995. The contrast in upper mantle shear-wave velocity between the East European Platform and Tectonic Europe obtained with genetic algorithm inversion of Rayleigh wave group dispersion, Geophys. J. Int., 123,

169-182.

Longuet-Higgins, M. 1950. A theory of the origin of microseisms, Philos. Trans. R. Soc. London, 243, 137-171.

Lu L. Y., He Z. Q., Ding Z. F., et al. 2009. Investigation of ambient noise source in North China array. Chinese J. Geophysics. (in Chinese), 51(10):2566-2572, DOI:10.3969/j.issn.0001-5733.2009.10.015.

Ludwig, W. J., Nafe, J. E., and Drake, C. L., 1970. Seismic refraction. In: The Sea, Wiley-Intersci., New York. Vol.4, Part 1:53-84.

Luo Y., Chong J. J., Ni S. D., et al. 2008. Moho depth and sedimentary thickness in Captital region, 51(4), 1135-1145.

Mao J. W., Wang Y. T., Zhang Z. H., et al., 2003. Geodynamic settings of Mesozoic large-scale mineralization in North China and adjacent areas-implication from the highly precise and accurate ages of metal deposits, Science in China, Ser. D, 46 (8), 838-851.

Menzies, M. A., Fan, W. M. and Zhang, M., 1993. Palaeozoic and Cenozoic lithoprobes and the loss of >120 km of Archaean lithosphere, Sino-Korean craton, China. In: H.M. Prichard, T. Alabaster, N.B.W. Harris and C.R. Neary (Editors), Magmatic Processes and Plate Tectonics. Geological Society of London Special Publication, pp. 71-81.

Mishra, O., Zhao, D., 2003. Crack density, saturation rate and porosity at the 2001 Bhuj, India, earthquake hypocenter: a fluid-driven earthquake? Earth Planet. Sci. Lett. 212, 305-393.

Montagner, J. P., 1986. Regional three-dimensional structures using long-period surface waves, Ann. Geophys., 4, B3, 283-294.

Montagner, J. P. & Nataf, H. C., 1986. A simple method for inverting the azimuthal anisotropy of surface waves, J. Geophys. Res., 91, 511-520.

Montagner, J. P. & Tanimoto, T., 1991. Global upper mantle tomography of seismic velocities and anisotropies, J. Geophys. Res., 96, 20337–20351.

Moschetti, M. P., M. H. Ritzwoller, and N. M. Shapiro, 2007. Surface wave tomography of the western United States from ambient seismic noise: Rayleigh wave group velocity maps, Geochem. Geophys. Geosyst., 8, Q08010, doi:10.1029/2007GC001655.

Nabelek J., Chen W. 1987. The Tangshan earthquake sequence and its implications for the evolution of the North China Basin. J. Geophys. Res., 92: 12615-12628.

Nawa, K., N. Suda, T. S. Y. Fukao, Y. Aoyama, and K. Shibuya, 1998. Incessant excitation of the Earth's free oscillations, Earth Planets Space, 50, 3-8.

Nolet, G., 1990. Partitioned wave-form inversion and 2D structure under the NARS

array, J. Geophys. Res., 95, 8513-8526.

Panza, G. F., 1981. The resolving power of seismic surface wave with respect to crust and upper mantle structural models. In: R. Cassinis, Editor, The Solution of the Inverse Problem in Geophysical Interpretation, Plenum press, pp. 39-77.

Panza, G. F., Raykova, R. B., Carminati, E., et al, 2007. Upper mantle flow in the western Mediterranean. Earth and Planetary Science Letters, 257, 200-214.

Paul, A., M. Campillo, L. Margerin, E. Larose, and A. Derode. 2005. Empirical synthesis of time-asymmetrical Green functions from the correlation of coda waves, J. Geophys. Res., 110, B08302, doi:10.1029/2004JB003521.

Pedersen, H., F. Krüger, and the SVEKALAPKO Seismic Tomography Working Group, 2007. Influence of the seismic noise characteristics on noise correlations in the baltic shield, Geophys. J. Int., 168(1), 197-210.

Pezeshk, S., C. V. Camp, and D. Chen. 2000. Design of Nonlinear Framed Structures Using Genetic Optimization, Journal of Structural Engineering, 126, 3, 382-388.

Pezeshk, S., and C. V. Camp. 2002. State of the Art on the Use of Genetic Algorithms in Design of Steel Structures, in Recent Advances in Optimal Structural Design, S. Burns (Editor), American Society of Civil Engineers.

Pezeshk S and Zarrabi M, 2005. A New Inversion Procedure for Spectral Analysis of Surface Waves Using a Genetic Algorithm, Bulletin of the Seismological Society of America; 95, 5, 1801-1808. DOI: 10.1785/0120040144.

Polat, A., Herzberg, C., Munker, C. et al., 2006. Geochemical and petrological evidence for a suprasubduction zone origin of NeoArchaean (c. 2.5 Ga) peridotites, central orogenic belt, North China craton. Geological Society of America Bulletin, 118, 771-784.

Pollack, H. N., 1986, Cratonization and thermal evolution of the mantle: Earth and Planetary Science Letters, v. 80, p. 175–182, doi:10.1016/0012–821X(86)90031–2.

Pontevivo, A. & Panza, G. F., 2002. Group velocity tomography and regionalization in Italy and bordering areas. PEPI, 134, 1-15.

Pontevivo, A. & Panza, G. F., 2006. The Lithosphere-Asthenosphere System in the Calabrian Arc and Surrounding Seas - Southern Italy. PAGEOPH, 163, 1617-1659.

Qiu R. Z., Deng J. F., Zhou S., et al., 2005. Lithosphere types in North China: Evidence from geology and geophysics. Science in China Ser. D Earth Sciences. 48, 11, 1809-1827.

Rhie, J., and B. Romanowicz, 2004. Excitation of Earth's continuous free oscillations by atmosphere-ocean-seafloor couplinng, Nature, 431, 552-554.

Rhie, J., and B. Romanowicz, 2006. A study of the relation between ocean storms and the Earth's hum, Geochem. Geophys. Geosyst., 7, Q10004, doi:10.1029/2006GC0012

74.

Ritzwoller, M.H. and A.L. Levshin, 1998. Eurasian surface wave tomography: Group velocities, J. Geophys. Res., 103, 4839-4878.

Roux P. and Kuperman W. A. 2004. Extracting coherent wavefronts from acoustic ambient noise in the ocean. The Journal of the Acoustical Society of America, 116, 4, 1995-2003.

Roux P., Sabra K.G., Gerstoft P. and KupermanW. A. 2005a. P-waves from cross correlation of seismic noise. Geophysical Research Letters, 32, L19303.

Roux P., Sabra K.G., Kuperman W.A. and Roux A. 2005b. Ambient noise cross correlation in free space: theoretical approach. The Journal of the Acoustical Society of America 117, 1, 79-84.

Sabra, K. G., P. Gerstoft, P. Roux, W. A. Kuperman, and M. C. Fehler, 2005a. Surface wave tomography from microseisms in Southern California, Geophys. Res. Lett., 32, L14311, doi:10.1029/2005GL023155.

Sabra, K. G., P. Gerstoft, P. Roux, W. A. Kuperman, and M. C. Fehler, 2005b. Extracting time-domain Green's function estimates from ambient seismic noise, Geophys. Res. Lett., 32, L03310, doi:10.1029/2004GL021862.

Sambridge, M. S. and G. G. Drijkoningen, 1992. Genetic algorithms in seismic waveform inversion, Geophys. J. Int., 109, 323-342.

Sambridge, M. & Gallagher, K., 1993. Earthquake hypocentre location using genetic algorithms. Bull. Seismological Society America, 83, 1467-1491.

Sánchez-Sesma, F., and M. Campillo, 2006a. Retrieval of the green function from cross correlation: The canonical elastic problem, Bull. Seismol. Soc. Am., 96(3), 1182–1191, doi:10.1785/0120050181.

Sánchez-Sesma F. J., Pérez-Ruiz J., Campillo M., and Luzón F. 2006b. Elastodynamic 2-D Green function retrieval from cross correlation: canonical inclusion problem. Geophysical Research Letters, 33, L13305.

Sánchez-Sesma F. J., Pérez-Ruiz J., Luzón F., Campillo M. and Rodriguez-Castellano A. 2007. Diffuse fields in dynamic elasticity. Wave Motion, 45, 5, 641-654.

Schulte-Pelkum, V., P. S. Earle, and F. L. Vernon, 2004. Strong directivity of ocean-generated seismic noise, Geochem. Geophys. Geosyst., 5, Q03004, doi:10.1029/2003GC000520.

Schwab F and Knopoff L. 1970. Surface wave dispersion computations. Bull Seism Soc Am, 60, 321-344.

Schwab F and Knopoff L. 1972. Fast Surface Wave and Free Mode Computations. in Methods in Computational Physics. Editor: Bolt, B A, Academic Press, New York NY, 11, 87-180.

Sebai A, Stutzmann E, Montagner J P, Sicilia D, Beucler E, 2006. Anisotropic structure of the African upper mantle from Rayleigh and Love wave tomography, Phys. Earth Planet. Inter., 155, 48-62.

Shapiro, N.M. and M.H. Ritzwoller, 2002. Monte-Carlo inversion for a global shear velocity model of the crust and upper mantle, Geophys. J. Int., 151, 88-105

Shapiro, N. M., and M. Campillo, 2004. Emergence of broadband Rayleigh waves from correlations of the ambient seismic noise, Geophys. Res. Lett., 31, L07614, doi:10.1029/2004GL 019491.

Shapiro, N., M. Campillo, L. Stehly, and M. Ritzwoller, 2005. High-resolution surface wave tomography from ambient seismic noise, Science, 307, 1615-1618.

Sheng Q. H., 1998. Geological characteristics and geological setting of banded itabirite on the Early Precambrian in North China Platform, in Contributions on the Early Precambrian Geology in North China Craton (eds. Sheng Qihan, Cheng Yuqi) (in Chinese), Beijing: Geological Publishing House, 1-31.

Shi Y L and Jin W. 1995. Genetic algorithms inversion of lithospheric structure from surface wave dispersion. Chinese J. Geophys. (in Chinese),38(2):189-198.

Simons, F. J., Zielhuis, A., and Van der Hilst, R. D., 1999. The deep structure of the Australian continent inferred from surface wave tomography, Lithos, 48/1-4, 17-43.

Simons, F. J., van der Hilst, R. D., Montagner, J. P., and Zielhuis, A., 2002. Multimode Rayleigh wave inversion for heterogeneity and azimuthal anisotropy of the Australian upper mantle, Geophys. J. Int., 151, 738-754

Snieder, R. 2004. Extracting the green's function from the correlation of coda waves: A derivation based on stationary phase, Phys. Rev. E, 69.

Song Z. L., Yang Z. X., Shi J. H., et al., 1997, Reconstruction of the basement velocities and time-terms using Pg waves in North China region. North China Earthquake Sciences. 15, 2, 9-16.

Stehly, L., M. Campillo, and N. M. Shapiro. 2006. A study of the seismic noise from its long range correlation properties, J. Geophys. Res., 111, B10306, doi:10.1029/ 2005JB004237.

Stoffa, P. L., and Sen, M. K., 1991. Nonlinear multiparameter optimization using genetic algorithms: Inversion of plane-wave seismograms, Geophysics,56 , 1794-1810.

Sun R. M., Liu F. T., 1995. Crust structure and strong earthquake in Beijing,Tianjing,Tangshan area-I : P wave velocity structure. Chinese J .Geophys. (in Chinese), 38 (5), 599-607.

Suresh G., Jain S., and Bhattacharya S. N., 2008. Lithosphere of Indus Block in the Northwest Indian Subcontinent through Genetic Algorithm Inversion of Surface-Wave Dispersion, Bulletin of the Seismological Society of America, 98, 4, 1750-1755. DOI:

10.1785/0120070254.

Tanimoto, T., J. Um, K. Nishida, and N. Kobayashi, 1998. Earth's continuous oscillations observed seismically quiet days, Geophys. Res. Lett., 25, 1553-1556.

Tanimoto, T., and J. Um, 1999. Cause of continuous oscillations of the earth, J. Geophys. Res., 104(B12), 723-739.

Tanimoto, T. 2005. The oceanic excitation hypothesis for the continuous oscillations of the Earth, Geophys. J. Int, 160, 276-288.

The Earthquake Disaster Prevention Department of China Earthquake Administration, 1995. Catalogue of Chinese Historical Strong Earthquakes. Beijing: Seismological Press.

The Earthquake Disaster Prevention Department of China Earthquake Administration, 1999. Catalogue of Chinese Present Earthquakes. Beijing: China Science and Technology Press.

Tian, Y., D. Zhao, R. Sun, and J. Teng. 2009. Seismic imaging of the crust and upper mantle beneath the North China Craton, Phys. Earth Planet. Inter., 172, 169–182, doi:10.1016/j.pepi.2008.09.002.

Urban Ludvík, Cichowicz Artur and Vaccari Franco, 1993. Computation of analytical partial derivatives of phase and group velocities for Rayleigh waves with respect to structural parameters, Studia Geophysica et Geodaetica, 37, 14-36.

Valyus, 1972, Determining seismic profiles from a set of observations. In: V.I. Keilis-Borok, Editor, Computational Seismology, Consultation Bureau, New York.

Van Tiggelen, B. 2003. Green function retrieval and time reversal in a disordered world, Phys. Rev. Lett, 91(24), 243904.

Wan Y. S., Zhang Q. D., Song T. R., 2003. SHRIMP ages of detrital zircons from the Changcheng System in the Ming Tombs area, Beijing: Constraints on the protolith nature and maximum depositional age of the Mesoproterozoic cover of the North China Craton, Chinese Science Bulletin, 48(22), 2500-2506.

Wang W. L., Wu J. P., Fang L. H., 2009, Crust and upper mantle S-wave velocity structure beneath TangHai-ShangDu seismic array profile. Chinese J. Geophys. (in Chinese), 52(1), 81-89.

Wang W. L., 2008. S-wave velocity structure beneath seismic array profiles in North-China obtained from joint inversion of receiver functions and surface wave dispersion. Master Thesis. Institute of Geophysics, China Earthquake Administration.

Wang J., Liu Q. Y., Chen J. H., et al., 2009, The crustal thickness and Poisson's ratio beneath the Capital Circle Region. Chinese J. Geophys.(in Chinese). 52, 1, 57-66.

Wang J. L., Li B. Z., Zhou D. X. et al., 1994. Geology of Intermediate-Acidic Intrusions and Their Relations to Metallogeny, Hebei Province (in Chinese), Beijing:

Geological Publishing House, 1-213.

Wang, Y. P., Deng, Q. D. & Zhu, S. L., 1989. Lithospheric dynamics of north China. In: Ma, X. (Ed.), Lithospheric Dynamics Atlas of China. Beijing: China Cartographic Publishing House, pp, 62.

Wapenaar K. 2004. Retrieving the elastodynamic Green's Function of an arbitrary inhomogeneous medium by cross correlation. Physical Review Letter, 93, 254301.

Weaver, R. L., and O. I. Lobkis, 2001. On the emergence of the Green's function in the correlations of a diffuse field, J. Acoust. Soc. Am., 110, 3011–3017.

Weaver R. L. and Lobkis O. I. 2003. Elastic wave thermal fluctuations, ultrasonic waveforms by correlation of thermal phonons. The Journal of the Acoustical Society of America 113, 2611–2621.

Weaver, R. L., and O. I. Lobkis, 2004. Diffuse fields in open systems and the emergence of the Green's function, J. Acoust. Soc. Am., 116, 2731-2734.

Weaver R. L. 2005. Information from seismic noise. Science, 307, 5715, 1568-1569.

Wilde, S. A., Xinhua Zhou, Nemchin, A. A. et al., 2003. Mesozoic crust-mantle interaction beneath the North China craton: A consequence of the dispersal of Gondwanaland and accretion of Asia, Geology, 31(9), 817-820.

Wilson, W. G. and K. Vasudevan, 1991. Application of the Genetic Algorithm to Residual Statics Estimation, Geophys. Res. Lett., 18, 2181-2184.

Wu F. Y., Shun D. Y., Zhang G. L., et al., 2000. Deep geodynamics of Yanshanian movement, Geological Journal of China Universities (in Chinese with English abstract), 6(3), 379-388.

Wu J. P., Ming Y. H., Zeng R. S., 2001. Smooth constraint inversion technique in genetic algorithms and its application to surface wave study in the Tibetan Plateau, Acta Seis,plogical Sinica, 14, 1, 49-57.

Xu W. W. and Zheng T. Y., 2005. Distribution of Poisson's ratios in the northwestern basin-mountain boundary of the Bohai Bay Basin. Chinese J. Geophys.(in Chinese), 48 (5), 1077-1084.

Xu, Y. G., 2001. Thermo-tectonic destruction of the Archean lithospheric keel beneath eastern China: Evidence, timing, and mechanism, Phys. Chem. Earth, 26A, 747-757.

Yamanaka H., Ishida H, 1996, Application of genetic algorithms to an inversion of surface-wave dispersion data, Bulletin of the Seismological Society of America; 86(2), 436-444.

Yang J. H., Wu F. Y., Simon A. Wilde, Elena Belousova and William L. Griffin, 2008. Mesozoic decratonization of the North China block, Geology, 36(6), 467-470; DOI: 10.1130/G24518 A.1.

Yang, Y., M. H. Ritzwoller, A. L. Levshin, and N. M. Shapiro, 2007. Ambient noise

Rayleigh wave tomography across Europe, Geophys. J. Int., 168, 259–274.

Yang, Y. and M. H. Ritzwoller, 2008. The characteristics of ambient seismic noise as a source for surface wave tomography, Geochem., Geophys., Geosys., 9(2), Q02008, 18 pages, doi:10.1029/ 2007GC001814.

Yanovskaya, T. B.,Ditmar, P. G. 1990. Smoothness criteria in surface wave tomography. Geophys. J. Int., 102, 63-72.

Yanovskaya, T. B., 1997. Resolution estimation in the problems of seismic ray tomography, Izv. Phys. Solid Earth, 33 (9), 762-765.

Yanovskaya, T. B., Kazima, E. & Antonova, L., 1998. Structure of the crust in the Black Sea and adjoining region. J. Seismol. 2, 303-316.

Yao, H., G., Xu, L., Zhu, and X., Xiao, 2005. Mantle structure from inter-station Rayleigh wave dispersion and its tectonic implication in western China and neighboring regions, Phys. Earth Planet. Inter., 148, 39-54.

Yao, H., R. D. vander Hilst, and M. V. de Hoop, 2006. Surface-wave array tomography in SE Tibet from ambient seismic noise and two-station analysis – I. Phase velocity maps. Geophys. J. Int., 166, 732-744.

Yin, X. H., Shi, Z. H. & Liu, Z. P., 1989. Bouguer gravity anomalies averaged in grid 1º×1º, In: Ma, X. (Ed.), Lithospheric Dynamics Atlas of China. Beijing: China Cartographic Publishing House, 1989. pp: 8.

Zeng R. S., Lu H. X. & Ding Z. F., 1988. Seismic refraction and reflection profiles across Tangshan epicentral region and their implication to seismogenic processes. Chinese J. Geophys. (Acta Geophysica Sinica) (in Chinese), 31(4), 383-398.

Zhai, M. G., 2005. 2.1–1.7 Ga geological event group and its geotectonic significance. Acta Petrologica Sinica, 20, 1343–1354.

Zhai, M. G., Guo, J. H. & Yan, Y. H. 1992. Discovery and preliminary study of Archaean high-pressure granulites in the North China Craton. Science in China, 12, 28–50.

Zhai, M. G., Guo, J. H., Li, Y. G. & Yan, Y. H. 1995. Discovery of Archaean retrograded eclogites in the North China Craton and their tectonic implications. Bulletin of Science in China, 40, 706–721.

Zhai, M. G., Yang, J. H., Fan, H. R., Miao, L. C. & Li, Y. G. 2002. A large-scale cluster of gold deposits and metallogenesis in the eastern North China craton. International Geology Reviews, 44, 458–476.

Zhang, K. 1989. Tectonics and Resources of Ordos Fault-Block. Geological Publishing House, Beijing.

Zhang C. K., Zhang X. K., Gai Y. J.,et al.,1997. A study of crust and upper mantle structure on Wen'an-Yuxian-Qaharyouyizhongqi profile. North China Earthquake

Sciences (in Chinese), 15(3), 18-28.

Zhang, L., Liu, J. S., Hao, T.Y., Liu, J. H. & Xu, Y., 2007. Seismic tomography of crust and upper mantle in Bohai Bay baisin and surrounding area, Science in China Ser. D Earth Sciences, 37(11), 1444-1455.

Zhang Z. Q., 1998. On the continental growth periods of North China craton based on Sm-Nd isotopic characteristics of early Precambrian metamorphic rocks, in Contributions on the Early Precambrian Geology in North China Craton (eds. Sheng Qihan, Cheng Yuqi) (in Chinese), Beijing: Geological Publishing House, 133-136.

Zhao, D., Kanamori, H., Negishi, H., 1996. Tomography of the source zone of the 1995 Kobe earthquake: evidence for fluids at the hypocenter? Science 274, 1891-1894.

Zhao, G. C.,Wilde, S. A., Cawood, P. A. & Lu, L. Z. 1998. Thermal evolution of basement rocks from the eastern part of the North China Craton and its bearing on tectonic setting. International Geology Reviews, 40, 706-721.

Zhao, G. C., Wilde, S. A., Cawood, P. A. & SUN, M. 2001a. Archaean blocks and their boundaries in the North China Craton: lithological, geochemical, structural and P–T path constraints and tectonic evolution. Precambrian Research, 107, 45-73.

Zhao, G. C., Wilde, S. A., Cawood, P. A. & Lu, L. Z. 2001b. High-pressure granulites (retrograded eclogites) from the Hengshan Complex, North China Craton: petrology and tectonic implications. Journal of Petrology, 42, 1141-1170.

Zhao, G., Sun, M., Wilde, S. & Li, S. Z. 2005. Late Archaean to Paleoproterozoic evolution of the North China Craton: key issues revisited. Precambrian Research, 136, 177-202.

Zhao, L., T. Zheng, and G. Lü.2008. Insight into craton evolution: Constraints from shear wave splitting in the North China Craton, Phys. Earth Planet. Inter., 168, 153-162, doi:10.1016/j.pepi.2008.06.003.

Zheng, S., X. Sun, X. Song, Y. Yang, & M. H. Ritzwoller, 2008, Surface wave tomography of China from ambient seismic noise correlation, Geochem. Geophys. Geosyst., 9, Q05020, doi:10.1029/2008GC001981.

Zheng Tianyu, Ling Chen, Liang Zhao,Weiwei Xu, Rixiang Zhu. 2006. Crust-mantle structure difference across the gravity gradient zone in North China Craton:Seismic image of the thinned continental crust, Physics of the Earth and Planetary Interiors, 159, 43-58.

Zheng Tianyu, Ling Chen, Liang Zhao, Rixiang Zhu. 2007. Crustal structure across the Yanshan belt at the northern margin of the North China Craton, Physics of the Earth and Planetary Interiors, 161, 36-49.

Zheng Tianyu, Liang Zhao, Ling Chen. 2005. A detailed receiver function image of the sedimentary structure in the Bohai Bay Basin, Physics of the Earth and Planetary

Interiors,152, 129-143.

Zhou X. H., Yang J. H. & Zhang L. C., 2003. Metallogenesis of superlarge gold deposits in Jiaodong region and deep processes of subcontinental lithosphere beneath North China Craton in Mesozoic, Science in China, Ser. D, 46(Supp.), 14-25.

Zhou X. H. & Sun M., 2003. Major transformation of subcontinental lithosphere mantle beneath the Sino-Korean Craton in Late Mesozoic: A possible global link, Goldschmidt Conference Abstracts, Geochimica et Cosmochimica Acta, 67(18s), 584.

Zhu, L. P. & Zeng, R. S., 1990. Three-Dimensional P-wave velocity structure under the Beijing network area. Chinese J. Geophys. (Acta Geophysica Sinica) (in Chinese), 33(3), 267-277.